Cosmological Parameter Estimation Using Sunyaev-Zel'dovich Selected Galaxy Cluster Abundances

Jon Dudley

Ph.D.

Department of Physics

McGill University

Montreal, Quebec

2012-08-15

A thesis submitted to McGill University in partial fulfilment of the requirements of the degree of Doctor of Philosophy

ACKNOWLEDGEMENTS

First and foremost I wish to acknowledge the the efforts and contributions of my supervisor Gil Holder, whose guidance and instruction formed the cornerstone of my graduate experience. I also wish to acknowledge the members of the SPT collaboration without the efforts of whom the results presented in this work would not be possible.

I would also like to acknowledge the wide assortment of educators that I have encountered on my academic path. Their dedication and passion for physics and teaching were both integral and inspirational.

Clearly deserving of mention are those who have shared the ERP-225 office experience, including all honourary or temporary members. The discussions, theorizing, problem-solving and general revelry witnessed within that office will never be forgotten.

Finally I wish to acknowledge the support of family and friends who provided constant reminders of realities outside the realm of academia and whose continued assistance and support was, and is greatly appreciated. After all, there are always more stars in the sky.

ABSTRACT

The observational record of the growth of structure in the universe over cosmic time offers a unique and invaluable cosmological measure. The abundance and evolutionary history of structure in the universe are dependent upon the parameters which define the cosmological framework. In this work, we formulate a method for deriving cosmological constraints from the observed abundance of galaxy clusters. These objects are the most massive gravitationally collapsed structures in the universe and act as tracers of the underlying density field. We develop a technique for comparing theoretical cluster abundances with observed galaxy cluster catalogs. In this process, we explore and constrain the parameter space for departures from the canonical cosmological model.

The motivation and framework for this investigation are presented in the opening chapters. An introduction to modern cosmological theory and methods for calculating theoretical galaxy cluster abundances are presented. A description of the physical observables associated with galaxy clusters follows, including a summary of detection methods. A cluster likelihood, defined through comparisons between observed cluster abundances with those predicted from theory, is developed.

The focus of this work rests in the analysis of the cluster likelihood. The fiducial ΛCDM model is explored and parameter constraints are presented. The cluster dataset is shown to provide useful constraints on numerous parameters and the inclusion of supplementary data is investigated. The cluster-scale normalization parameter σ_8 is well-constrained by this analysis, where we find $\sigma_8 = 0.745 \pm 0.082$ when considering only the cluster data and $\sigma_8 = 0.796 \pm 0.026$ for a combination of cluster and complementary datasets. The normalization of the scaling relation between the cluster observable and its mass and redshift is also constrained by this joint analysis such that, when compared with predictions from numerical simulations, we find $A_{SZ,meas.}/A_{SZ,fid.} = 0.82 \pm 0.17$.

Also explored are two extensions to the standard cosmological model, a non-cosmological-constant form of dark energy and non-Gaussian primordial fluctuations. In both cases the cluster likelihood is demonstrated to provide informative constraints, demonstrating consistency with a cosmological constant form of dark energy and Gaussian primordial fluctuations. Through a combination of cluster and complementary datasets we constrain the dark energy equation of state parameter to be $w = -1.07 \pm 0.12$. The degree of non-Gaussianity inferred from a catalog of massive galaxy clusters is also constrained, finding $f_{NL} = -36^{+456}_{-491}$ at 68% confidence for a particular non-Gaussian model.

ABRÉGÉ

Les données observationnelles de la croissance des structures dans l'univers représentent une mesure cosmologique unique et inestimable. La quantité et l'historique d'évolution des structures dans l'univers dépendent des paramètres qui définissent le contexte cosmologique. Dans le présent travail, nous formulons une méthode pour déduire des contraintes cosmologiques à partir d'observations du nombre d'amas de galaxies. Ces objets demeurent les structures les plus massives à être issues de l'effondrement gravitationnel dans l'univers et agissent comme traceurs du champ de densité sous-jacent. Nous développons une technique servant à comparer le nombre d'amas de galaxies théorique aux données des catalogues d'amas de galaxies observés. Ce faisant, nous explorons et contraignions l'espace de paramètres à la recherche de déviations par rapport au modèle cosmologique standard.

L'intérêt et le cadre de travail de cette recherche sont détaillés dans les premiers chapitres. Une introduction à la théorie de la cosmologie moderne et aux méthodes de calcul du nombre théorique d'amas de galaxies sera présentée. Ensuite, nous faisons la description des observables physiques associés aux amas de galaxies, incluant un résumé des méthodes de détection. Nous développons par après une fonction de vraisemblance des amas de galaxies définie par une comparaison entre les amas observés et les amas prédits par la théorie.

Le fil conducteur de ce travail réside dans l'analyse de la fonction de vraisemblance des amas de galaxies. Le modèle standard de la cosmologie, dit ΛCDM, est exploré et les contraintes sur ses paramètres sont présentées. L'utilisation d'ensembles

de donnes sur les amas de galaxies permet d'améliorer les contraintes sur plusieurs de ces paramètres. L'impact sur ces contraintes de l'ajout de données supplémentaires est également considéré. Cette analyse permet de contraindre significativement le paramètre de normalisation des fluctuations à l'échelle des amas de galaxies σ_8. Nous obtenons $\sigma_8 = 0.745 \pm 0.082$ en ne considérant que les données d'amas de galaxies et $\sigma_8 = 0.796 \pm 0.026$ en ajoutant des ensembles de données complémentaires. La normalisation du rapport d'échelle entre l'observable d'un amas de galaxies et sa masse est aussi contrainte par cette analyse conjointe. En comparant les résultats de notre analyse à ceux de simulations numériques, nous trouvons $A_{SZ,meas.}/A_{SZ,fid.} = 0.82 \pm 0.17$.

Nous explorons de plus deux extensions au modèle cosmologique standard, une forme d'énergie sombre ne correspondant pas à une constante cosmologique ainsi que des fluctuations primordiales non-Gaussiennes. Dans les deux cas, la fonction de vraisemblance des amas de galaxies a permis de produire des contraintes informatives. Nous contraignons le paramètre de l'équation d'état de l'énergie sombre comme étant $w = -1.07 \pm 0.12$. En appliquant la fonction de vraisemblance à un catalogue d'amas de galaxies massifs, nous trouvons que le degré de non-Gaussianité correspond à $f_{NL} = -36^{+456}_{-491}$, à un niveau de confiance de 68%, pour un modèle de non-Gaussianité donné.

TABLE OF CONTENTS

LIST OF TABLES

LIST OF FIGURES

CHAPTER 1
Introduction

1.1 Overview

Observations of the present day universe reveal a rich assortment of cosmological structures across an enormous range in size and mass. The existence and distribution of stars, galaxies, and clusters of galaxies in the universe indicates a complex evolutionary history, tracing back to the initial seeds of structure which formed in the first moments following the Big Bang. By studying the growth of structure over cosmic time we can gain valuable insights regarding the nature and composition of the universe.

In this work we will motivate and explore the cosmological constraints offered by the abundance and distribution of galaxy clusters in the late-time universe. The focus of this analysis will lie in the construction of a cluster likelihood formalism, which will permit comparisons between observed cluster abundances and theoretical predictions. Cosmological parameter estimation through the observation of galaxy clusters amounts to a counting experiment. Since their number density, as a function of cluster mass and cosmic distance, is a cosmologically-dependent quantity, a comparison between the observed galaxy cluster abundance with predictions from theory measures cosmological parameters. In order to make such a comparison, we must first investigate the means by which galaxy clusters may be observed while also constructing a method by which a theoretical prediction for galaxy cluster abundances may be made.

We will investigate parameters of not only the fiducial cosmological paradigm, which includes both cold dark matter and a cosmological constant, but also extensions and modifications to this model. We will demonstrate the sensitivity with which the growth of structure, as manifested by the abundance and distribution of massive galaxy clusters in the late-time universe, acts as a probe of cosmological parameters. We will develop a methodology for calculating theoretical distributions of galaxy clusters as a function of cluster mass, redshift, and cosmology.

Through the construction and implementation of a galaxy cluster likelihood formalism we will measure cosmological parameters. This likelihood formalism will establish the use of galaxy cluster catalogs as precise tools for constraining the cosmological parameter space.

This work will be organized as follows: Chapters 1 and 2 will provide an introduction to modern cosmological theory, along with metrics and measures relevant to the cluster analysis. Chapters 3 and 4 will introduce the galaxy cluster catalogs employed in this analysis, including the derivation of the formalism by which the theoretical cluster distributions will be calculated. Finally, in Chapters 5, 6, and 7 the main results of the analysis performed in this work will be presented and discussed, culminating with concluding remarks in Chapter 8.

1.2 The Expanding Universe

Theorized by both Alexander Friedmann [1] and George Lemaitre [2] in 1922 and 1927 respectively, and later famously supported by seminal observations of galaxy velocities performed by Edwin Hubble in 1929 [3], the modern cosmological paradigm is that of a spatially flat, expanding universe. Thorough analyses of this model can be found in many modern cosmological texts (e.g. Dodelson [4], J. E. Peebles [5], and Peacock [6]), a summary of which will be provided here.

The spatial expansion leads to a useful measure of cosmic distance known as the cosmological redshift, parameterized as $z = \frac{(\lambda_{\rm obs} - \lambda_{\rm rest})}{\lambda_{\rm rest}}$, where λ is the wavelength of the emitted light. It is also convenient to describe the expansion of such a universe in terms of a *scale factor* $a(t)$, related to the cosmological redshift z by $a = (1+z)^{-1}$ and normalized to the present time such that $a(t_{\rm today}) = 1$.

Another useful quantity is known as the *metric* which describes the geometry of a spacetime by defining a differential length within it. For the analysis presented in this section we will set the speed of light explicitly to $c = 1$ for convenience, unless otherwise noted. Through the scale factor we may describe an expanding, isotropic, and homogeneous universe in terms of the Friedmann-Lemaître-Robertson-Walker (FLRW) metric:

$$ds^2 = -dt^2 + a(t)^2 \left(\frac{dr^2}{1 - \kappa r^2} + r^2 d\Omega^2 \right), \tag{1.1}$$

where κ describes the curvature of the universe with $\kappa = -1$ signifying an open universe and $\kappa = +1$ corresponding to a closed universe. In the case where $\kappa = 0$, the FLRW metric provides a prescription for the metric expansion or contraction of a flat spacetime. We may also introduce a measure of distance, defined in terms of this expanding background, such that it remains constant between objects moving only with the expansion. This *comoving distance* relates a physical coordinate $\mathbf{x}$ to a comoving coordinate $\mathbf{r}$ through the scale factor, such that $\mathbf{x}(t) = a(t)\mathbf{r}(t)$.

The time-evolution of the scale factor can be calculated through the Einstein field equations

$$G_{\mu\nu} \equiv R_{\mu\nu} - \frac{1}{2} g_{\mu\nu} \mathcal{R} = 8\pi G T_{\mu\nu}, \tag{1.2}$$

where $G_{\mu\nu}$ is the Einstein tensor, $R_{\mu\nu}$ and $\mathcal{R}$ are measures of the metric, referred to as the Ricci tensor and Ricci scalar respectively. The energy-momentum tensor, $T_{\mu\nu}$, describes the energy and momentum of a fluid in terms of its energy density ρ, pressure p, and four-velocity U^{μ} where, for a perfect fluid,

$$T^{\mu\nu} = (\rho + p)\, U^{\mu} U^{\nu} + p g^{\mu\nu}. \tag{1.3}$$

The isotropy and homogeneity of the FLRW metric implies that the energy-momentum tensor $T_{\mu\nu}$ is isotropic as well, such that

$$T^{\mu\nu} = \begin{pmatrix} \rho & 0 & 0 & 0 \\ 0 & p & 0 & 0 \\ 0 & 0 & p & 0 \\ 0 & 0 & 0 & p \end{pmatrix}. \tag{1.4}$$

The FLRW metric can be inserted into the field equations, yielding the Friedmann equations which describe the time dependence of the scale factor:

$$\left(\frac{\dot{a}}{a}\right)^2 = \frac{8\pi G}{3}\rho - \frac{\kappa}{a^2} \tag{1.5}$$

$$\frac{\ddot{a}}{a} = -\frac{4\pi G}{3}\left(\rho + 3p\right), \tag{1.6}$$

where, assuming isotropy, we have directly substituted the relations $T^{00} = \rho$ and $T^{ii} = p$ and overdots correspond to derivatives with respect to time.

Here it is useful to define the Hubble parameter in terms of the scale factor and its derivative

$$H(t) \equiv \frac{\dot{a}}{a}, \tag{1.7}$$

such that we are able to rewrite the Friedmann equations in an alternate form:

$$H^2 = \frac{8\pi G}{3}\rho - \frac{\kappa}{a^2} \tag{1.8}$$

$$\dot{H} = -4\pi G\left(\rho + p\right) + \frac{\kappa}{a^2}. \tag{1.9}$$

Through these equations we are able to derive the continuity equation governing the time evolution of the component energy densities:

$$\dot{\rho} + 3H(\rho + p) = 0. \tag{1.10}$$

Some useful quantities include the Hubble time

$$t_H \equiv \frac{1}{H_0} = 3.086 \times 10^{17} h^{-1} \text{ s} = 9.778 \times 10^9 h^{-1} \text{ yrs}, \tag{1.11}$$

where h is set by the value of the Hubble constant, and the Hubble distance which, when expressed in physical units, is the product of the Hubble time and the speed of light c,

$$D_H \equiv \frac{c}{H_0} = 2997.9 h^{-1} \text{ Mpc}. \tag{1.12}$$

Referring back to the first Friedmann equation (1.8) we see that there exists a connection between the expansion rate, density and geometry of the universe. Given an observed expansion rate, there exists a value for the density which results in a spatially flat universe ($\kappa = 0$). This *critical density* is defined as follows:

$$\rho_{crit} = 3H_0^2/8\pi G. \tag{1.13}$$

From this critical density we may define a density parameter which expresses the ratio of a component's energy density to the critical density. Taking, for example, the matter energy density, this may be expressed as

$$\Omega_m \equiv \frac{\rho_m}{\rho_{crit}} = \frac{8\pi G \rho_m}{3H^2} \tag{1.14}$$

with a similar definition applying for the other quantities, such as the radiation energy density. The total energy density can be approximated as having three primary contributions: pressureless matter, radiation and dark energy. These three components will also evolve uniquely with the expansion of the universe, each according to its equation of state parameter w, where

$$w = \frac{p}{\rho}. \tag{1.15}$$

With this definition, Equation 1.10 may be rewritten in terms of w and integrated to find

$$\rho = \rho_0 \exp\left[-\int 3(1+w)\frac{da}{a}\right] \tag{1.16}$$

which, for time-independent equations of state, can be solved to yield

$$\rho \propto a^{-3(1+w)}. \tag{1.17}$$

For models with an evolving dark energy component, the equation of state parameter w can be time-dependent such that $w_{\mathrm{DE}}(a) \neq \mathrm{const}$ [7]. In such cases the evaluation of the integral in Equation 1.16 may require numerical evaluation.

For matter $p_m = 0$ and thus $w_m = 0$. From Equation 1.17 we see that this implies that the matter component evolves as $\rho_m \propto a^{-3}$, which indicates that the energy density in matter evolves simply with the increase in volume due to the spatial expansion. For radiation, the pressure is related to the energy density through $p = 1/3\rho$ and thus $w_r = 1/3$. This implies an evolution for the radiation energy density which is steeper than its matter counterpart: $\rho_r \propto a^{-4}$. This can be considered to be an effect of the increasing volume as well as the redshifting of the radiation due to the spatial expansion. In the absence of dark energy, the evolution of these two components describes an expanding universe which is radiation-dominated at early times and matter-dominated at late times. For the dark energy component, we will assume a constant equation of state $w_{\rm DE}$ such that the dark energy density evolves as $\rho_{\rm DE} \propto a^{-3(1+w)}$. For the remainder of this work w will refer exclusively to the dark energy equation of state, unless otherwise noted.

There also exists a particular form of dark energy referred to as the *cosmological constant*, Λ, and parameterized as ρ_Λ. For a cosmological constant $w \equiv -1$, such that this dark energy density is constant in time. Such a form of dark energy is often described in terms of a *vacuum energy*, describing the energy density of empty space [8, 9]. Presented in terms of the earlier Einstein equations, the effect of this vacuum energy can be modeled as

$$G_{\mu\nu} \equiv R_{\mu\nu} - \frac{1}{2} g_{\mu\nu} \mathcal{R} = 8\pi G \left(T_{\mu\nu} - \rho_\Lambda g_{\mu\nu} \right). \tag{1.18}$$

This vacuum energy may be described through field theory approaches, however, predictions for its amplitude have shown extremely poor agreement with observations [8, 9, 10].

We may now rewrite Equation 1.5 in terms of the Hubble parameter and energy densities, finding

$$H(z) = H_0 \left[\Omega_R (1+z)^4 + \Omega_m (1+z)^3 + \Omega_{\rm DE} (1+z)^{3(1+w)} \right]^{1/2}, \tag{1.19}$$

where $H_0 = 100h$ km/s/Mpc and we have explicitly assumed both a flat universe ($\Omega_k = 0$) and a time-independent dark energy equation of state. In practice it will be convenient to also define an expansion factor

$$E(z) = \frac{H(z)}{H_0} = \left[\Omega_R(1+z)^4 + \Omega_m(1+z)^3 + \Omega_{\rm DE}(1+z)^{3(1+w)}\right]^{1/2}. \tag{1.20}$$

Having briefly discussed the geometry of the universe and its expansion we will now define some measures of distance and time. The first quantity to be defined is a measure of the time elapsed since the big bang and is known as the conformal time

$$\eta(t) \equiv \int_0^t \frac{dt'}{a(t')}. \tag{1.21}$$

This monotonically increasing function helps define causality in that regions separated by more than a distance η (when $c = 1$) could never have been in causal contact, thus defining a horizon.

As mentioned earlier, we can introduce a measure of distance, defined in terms of the expanding background such that it remains constant between objects moving only with the expansion. This comoving distance can be expressed as

$$D_C(z) = D_H \int_0^z \frac{dz'}{E(z')}, \tag{1.22}$$

which, for a given value of D_C, is related to a physical distance $D_{\rm phys}(t)$ through the scale factor, such that $D_{\rm phys}(t) = a(t)D_C$.

An astronomically useful quantity for measuring distance lies in the comparison of an object's physical size (l) and the angle it subtends on the sky (θ) and is referred to as the angular diameter distance

$$D_A = \frac{l}{\theta}. \tag{1.23}$$

Assuming no spatial curvature, we find

$$D_A(z) = \frac{D_C}{1+z} = \frac{D_H}{1+z}\int_0^z \frac{dz'}{E(z')}. \tag{1.24}$$

At low redshift we see that the angular diameter distance D_A behaves as the comoving distance D_C. Interestingly, the angular diameter distance reaches a maximum at finite redshift, beyond which it decreases; this effect is demonstrated in Figure 1–1. This peculiar behaviour impacts upon the observation of astrophysical objects at high redshift and will be further explored in Chapter 3.

The final quantity to be defined in this section is the comoving volume element. This describes the volume per steradian per unit redshift in which the comoving number density of non-evolving objects remains constant:

$$dV_C(z) = D_H \frac{(1+z)^2 D_A^2}{E(z)} d\Omega dz, \tag{1.25}$$

where $d\Omega$ refers to the solid angle. These formulae will prove integral in future sections, particularly when discussing the observed and predicted abundance of cosmological structures in terms of survey area and extent.

1.3 Cosmological Models

In this section we will introduce the modern cosmological paradigm, the parameters which describe it, and their physical significances. Included in this discussion will be an examination of an important extension to this standard cosmological model. The standard cosmological model is the "ΛCDM" model and is described through a set of six parameters, as presented in Table 1–1. Also shown are recent constraints from the WMAP 7-year dataset, as described in Komatsu et al. [11].

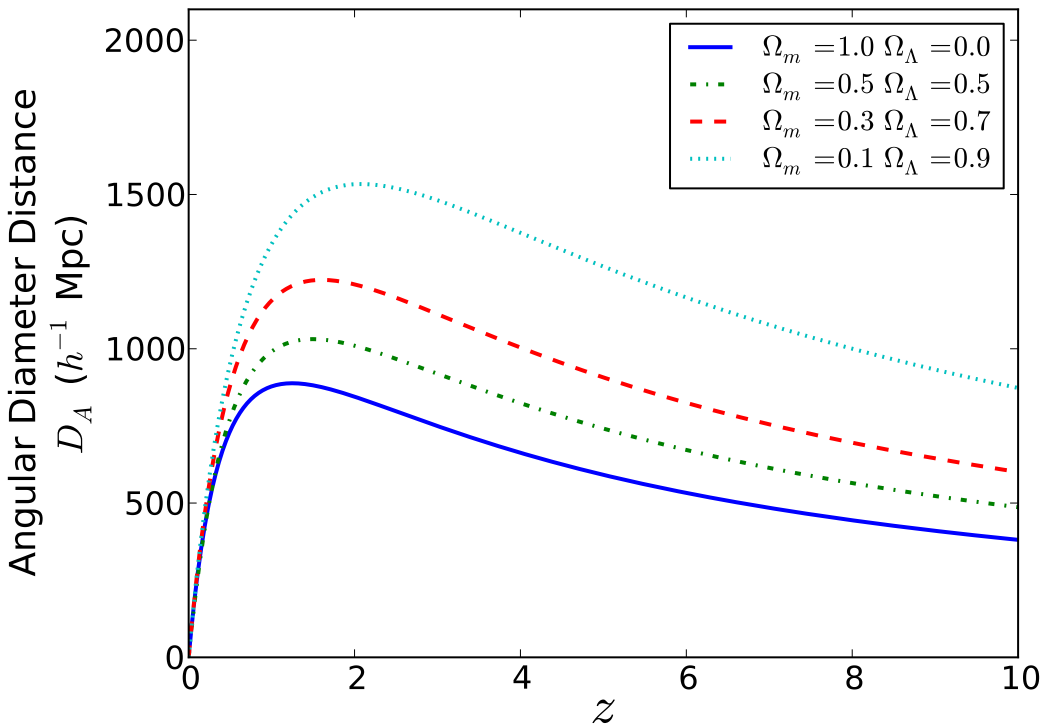

Figure 1–1: Angular diameter distance as a function of cosmological parameters, where Ω_m and Ω_Λ refer to the matter and cosmological constant densities respectively. In each model the function reaches a peak near a redshift of $z \approx 2$ and subsequently decreases with distance.

These parameters describe a spatially flat universe consisting of a baryonic component, cold dark matter and the cosmological constant Λ, whose energy density is spatially homogeneous and constant in time, such that $w \equiv -1$.

Table 1–1: Six-parameter ΛCDM model

Parameter	Description	WMAP7 Fit[1]
Base Parameters		
$10^2\Omega_b h^2$	Physical baryon density	$2.249^{+0.056}_{-0.057}$
$\Omega_c h^2$	Physical cold dark matter density	0.1120 ± 0.0056
Ω_Λ	Cosmological constant	0.727 ± 0.029
A_s	Curvature perturbation amplitude [2]	$(2.43 \pm 0.11) \times 10^{-9}$
n_s	Scalar spectral index	0.967 ± 0.014
τ	Optical depth to reionization	0.088 ± 0.015
Derived Parameters		
H_0	Hubble constant	70.4 ± 2.5 km s^{-1} Mpc^{-1}
σ_8	RMS mass fluctuations on $8h^{-1}$Mpc scales	0.811 ± 0.030
Ω_b	Baryon density	0.0455 ± 0.0028
Ω_m	Matter density	0.273 ± 0.029

[1] Results from Komatsu et al. [11]
[2] Evaluated at $k = 0.002$ Mpc^{-1}

The ΛCDM model also has two parameters describing the primordial density fluctuations, the primordial amplitude A_s and the spectral index n_s. These parameters will be explored in the subsequent section where their meanings will be clearly defined. The sixth parameter of the ΛCDM model presented in Table 1–1, τ, describes the integrated optical depth to a period known as *reionization*. This describes the epoch in which matter in the universe transitioned from a neutral to an ionized state due to the emergence of ionizing sources [12, 13]. From this base set of parameters one can derive other useful measures of cosmology; some examples are listed in Table 1–1.

Support for the ΛCDM model is provided through a variety of observable phenomena including Big Bang Nucleosynthesis [14], Baryon Acoustic Oscillations [15], Supernovae distance measures [16, 17], and the Cosmic Microwave Background [11, 18, 19]. Despite the broad observational support for the ΛCDM model, there are a few anomalies, including but not limited to: an anomalously low quadrupole in the Cosmic Microwave Background [20], an apparent dearth of galactic dark matter satellites [21], and inconsistencies between the predicted and observed lithium abundance [22]. Discrepancies in the late-time abundance of massive galaxy clusters have also been reported; these claims are addressed in Chapter 7 [23, 24].

A key feature of the ΛCDM model is that the dark energy component assumes the form of a time-independent cosmological constant. This particular form of dark energy is characterized through its equation of state, as defined in Equation 1.15, such that $w \equiv -1$, rendering its energy density independent of time, as per Equation 1.17. However, this time-independence of the dark energy density is not required. In particular, there exist classes of dark energy models which permit a dark energy equation of state of $w \neq -1$ [7, 25, 26, 27, 28, 29].

These models can be parameterized through an additional seventh parameter, w, which will describe the seven-parameter "wCDM" cosmological model. A detailed review of the various interpretations of this framework is presented in Copeland et al. [7]. Some dark energy models allow for an additional time-evolution in the dark energy equation of state, requiring an additional parameter governing this evolution. For simplicity we do not include such models in our exploration. A dark energy density with $w \neq -1$ will be parameterized as Ω_{DE} so as to distinguish it from the cosmological constant dark energy density, Ω_Λ. Thus, the wCDM model is described by the same base parameters as the ΛCDM model, as presented in Table 1–1, with the addition of a seventh parameter describing the dark energy equation of state, w.

One example of a class of non-cosmological-constant dark energy models is the *quintessence* model and has been the subject of study in recent years [7, 30, 27, 28, 29]. Quintessence models describe dark energy in terms of a scalar field ϕ, where the equation of state for this scalar field is related to its kinetic and potential components such that [7]

$$w_\phi = \frac{p}{\rho} = \frac{\dot{\phi}^2 - 2V(\phi)}{\dot{\phi}^2 + 2V(\phi)}. \tag{1.26}$$

A regime of interest occurs when the potential term dominates the kinetic term such that $\dot{\phi}^2 \ll V(\phi)$. This is referred to as the *slow-roll* condition where $w_\phi \simeq -1$). Although general quintessence models permit a time-varying equation of state, a constant equation of state parameter forms a good approximation for many models [31, 32, 33].

Further analysis of Equation 1.26 reveals it to be bounded from both above and below such that $-1 \leq w_\phi \leq 1$. As shown in Equation 1.6, an accelerated expansion ($\ddot{a} > 0$) occurs only when $w < -1/3$. This $w \geq -1$ lower limit of the quintessence model precludes it from violating the dominant energy condition which requires that $\rho \geq |p|$. Models which cross this divide are presented in Copeland et al. [7] and Caldwell et al. [28]. Thus, while not accessible by quintessence models, it is possible to make a generalized negative-pressure condition for dark energy, requiring only that $w < 0$ for a generic wCDM model.

Having introduced the time evolution of the matter and radiation energy density components in the preceding section we will now conclude that discussion by examining the evolution of the dark energy density as a function of its equation of state. To do so we will consider three key regimes for the dark energy equation of state: $w \equiv -1$, $-1 < w < -1/3$ and $w < -1$.

First, we will consider the scenario described in the previous section, that of a cosmological constant form of dark energy where $w = -1$. In this case, we find (through Equation 1.16) that ρ_Λ does not evolve in time, instead remaining constant as a function of redshift. This behaviour contrasts with that of the radiation and matter components, both of which dilute with the spatial expansion. Thus, at early times, the matter and radiation energy densities will be dominant when compared with the dark energy density while at sufficiently late times the cosmological constant will dominate as both matter and radiation densities will decrease with the expansion of the universe.

When compared with a matter-dominated ($\Omega_m = 1$) universe without a dark energy component, and with other parameters held fixed, the ΛCDM expansion rate will be suppressed at early times. Given the observed state of the universe today, a universe with a cosmological constant form of dark energy will be older than one without. The cosmological constant will also alter the acceleration of the expansion, as characterized by Equation 1.6. For both matter and radiation, this acceleration term remains negative, indicating a slowing expansion. The addition of a cosmological constant permits a positive value for the acceleration, indicating that in the late-time dark-energy-dominated era the expansion of the universe will be accelerating. These contrasting scenarios are presented in Figure 1–2 which displays the past and future expansion histories for cosmologies both with and without a form of dark energy. As demonstrated in this figure, measurements of the past expansion rate provide a means by which we may test cosmological models.

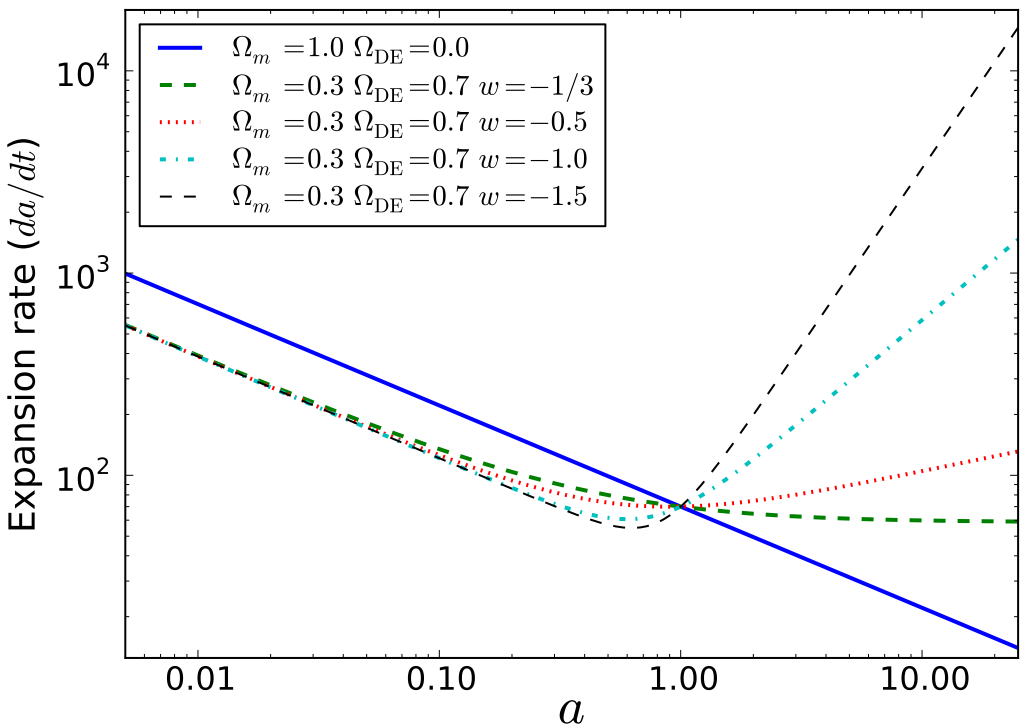

Figure 1–2: Expansion histories as a function of cosmology and scale factor. As shown in Equation 1.6, cosmologies with $w <$ -1/3 display an accelerating expansion in the current epoch (a = 1) while both the w = -1/3 and Ω_m = 1 cosmologies indicate a decelerating expansion during that same period.

The second dark energy equation of state regime occurs for $-1 < w < -1/3$. As shown in Equation 1.6 and displayed in Figure 1–2, these cosmologies also produce an accelerating expansion in the current era. The transition between an accelerating and decelerating expansion occurs for $w = -1/3$ at which point, as shown in Figure 1–2, the expansion rate asymptotes to a constant value. Although we will consider dark energy equations of state in the regime $-1/3 < w < 0$ it is common to consider dark energy as providing a positive acceleration to the expansion at late times, a condition satisfied for all $w < -1/3$. For equations of state with $-1 < w < -1/3$, the dark energy density is decreasing with time and thus had a larger dark energy density in the past. The past expansion rates for these cosmologies would be higher than comparable ΛCDM cosmologies, which renders these universes younger than their $w = -1$ counterparts. This behaviour may be inferred from Figure 1–2, as the cosmic age may be calculated through an integration of the inverse of the expansion rate da/dt.

We also consider an exotic regime for the dark energy equation of state, the so-called "phantom"[1] regime where $w < -1$. Inspection of Equation 1.17 indicates that for these cosmologies $\rho_{\rm DE} \propto a^n$ where $n > 0$. This relation implies that the dark energy density in this scenario increases with the expansion, rapidly resulting in a universe dominated by dark energy. The end states for such a model are documented in Caldwell et al. [28] wherein they show that this form of dark energy would eventually disassociate atoms in a "big-rip" scenario. Conversely, as shown in Figure 1–2, the expansion rate for these models is suppressed at early times when compared

[1] This terminology is explained in Caldwell [34] as: "A phantom is something which is apparent to the sight or other senses but has no corporeal existence - an appropriate description for a form of energy necessarily described by unorthodox physics..."

with a similar ΛCDM cosmology, resulting in a comparatively older universe. The expansion experiences a positive acceleration at late times, the degree of which depends upon the exact value of w, through Equation 1.6. Constructing theoretical models for phantom dark energy and, in particular, avoiding a finite-time singularity can be challenging; we will treat the exploration of this space primarily in terms of obtaining evidence for deviations from the standard cosmological model ($w \equiv -1$) rather than the validation of a specific physical model of dark energy [28, 35, 36].

1.4 Inflation and Primordial Perturbations

The observed abundance of structure in the late-time universe requires the existence of primordial fluctuations. One possible origin is a period of early, rapid spatial expansion known as *inflation* [37, 38, 39, 40, 41, 42]. During this period the scale factor had the form

$$a(t) \sim e^{Ht}, \tag{1.27}$$

indicating an accelerated expansion such that $\ddot{a} > 0$. The inflationary paradigm alleviates seeming cosmological inconsistencies, such as the observed approximate spatial flatness of the universe, an absence of magnetic monopoles and the observed isotropy and homogeneity on large scales [37, 42]. Similar to the dark energy models discussed in the previous section, simple models of inflation rely upon an homogeneous inflationary scalar field ϕ, often referred to as the *inflaton*. In this section we will present a brief overview of the possible inflationary origins of the primordial perturbations.

In the simple, single-field inflationary model, the energy density and pressure of the inflaton may be described in terms of the inflaton potential $V(\phi)$ as [4, 41, 42, 43]

$$\rho = \frac{1}{2}\dot{\phi}^2 + V(\phi) \tag{1.28}$$

$$P = \frac{1}{2}\dot{\phi}^2 - V(\phi). \tag{1.29}$$

If the potential term $V(\phi)$ dominates over the kinetic term $\frac{1}{2}\dot{\phi}^2$ (such that $V(\phi) \gg \dot{\phi}^2$) then the equation of state for the inflaton is described as

$$p \simeq -\rho \tag{1.30}$$

such that $w \simeq -1$. This equation of state satisfies the conditions for an accelerating expansion ($\ddot{a} > 0$), as defined by the second Friedmann equation (Equation 1.6).

We can express the two Friedmann equations (1.8 and 1.9) in terms of this inflaton field as

$$H^2 = \frac{8\pi G}{3}\left(\frac{1}{2}\dot{\phi}^2 + V(\phi)\right) \tag{1.31}$$

$$\dot{H} = -4\pi G\,(\rho + p) \simeq 0, \tag{1.32}$$

where the second equation indicates that the physical Hubble radius (Equation 1.12), which defines the region in which causal processes may operate, is roughly constant during this inflationary period. Inflationary models often end with a period known as "reheating", wherein the energy density is transferred to the matter component [44, 45].

Single-field inflationary models offer a method by which the primordial cosmological perturbations, from which structure will form, may be generated. Here we will consider the first order perturbation to the inflaton field, $\delta\phi$. The inflaton perturbation can be expressed in Fourier space as

$$\delta\phi_k = \int d^3\mathbf{x}\delta\phi(\mathbf{x},t)e^{-i(\mathbf{k}\cdot\mathbf{x})}. \tag{1.33}$$

In the simple, single-field inflationary model, primordial quantum perturbations are generated in the inflaton field with physical scales ($\lambda = 2\pi a/k$) which grow quickly with the accelerating scale factor, eventually exceeding the horizon scale during the inflationary period. This permits primordial quantum perturbations to grow to super-horizon scales during inflation. Assuming an end to the inflationary period, these perturbations subsequently re-enter the horizon during the radiation or matter-dominated eras, during which the Hubble radius again grows ($\dot{H} < 0$). The inflaton perturbation in this model describes a field with zero mean and non-zero variance, composed of Fourier modes with uncorrelated phases, describing a Gaussian spectrum. Thus, the single-field inflationary model predicts a Gaussian spectrum of primordial perturbations across an enormous range in scale [4, 41, 42, 43, 44].

It will also be useful to consider the expectation value for the fluctuations in the inflaton field which we may express as

$$\langle\delta\phi(\mathbf{k}_1)\delta\phi(\mathbf{k}_2)\rangle = (2\pi)^3\delta^3(\mathbf{k}_1+\mathbf{k}_2)P_\phi(k_1), \tag{1.34}$$

where angle brackets indicate an ensemble average, δ^3 represents the Dirac delta function, and $P_\phi(k)$ is known as the *power spectrum* (where ϕ has replaced $\delta\phi$ for clarity). It is also convenient to define a dimensionless power spectrum, expressing the variance per ln k as

$$\Delta_\phi^2(k) \equiv \frac{4\pi k^3 P_\phi(k)}{(2\pi)^3} = \frac{k^3 P_\phi(k)}{2\pi^2} \tag{1.35}$$

It is common to express this primordial power spectrum in terms of the comoving curvature perturbation $\mathcal{R}$. Within this parameterization, this primordial spectrum is conventionally expressed in terms of a scale-dependent amplitude parameter and a tilt parameter [46, 47, 11]:

$$\Delta_\mathcal{R}^2 = \Delta_\mathcal{R}^2(k_0)\left(\frac{k}{k_0}\right)^{n_s-1}, \tag{1.36}$$

where $n_s = d\ln\Delta_\mathcal{R}^2/d\ln k$ represents the "tilt" of the spectrum and k_0 defines the normalization scale. When $n_s \equiv 1$ the spectrum is constant in k and is referred to as *scale invariant*.

The amplitude $\Delta_\mathcal{R}^2(k_0)$ and tilt n_s of the primordial spectrum described in Equation 1.36 also comprise two of the fundamental parameters of the ΛCDM and wCDM cosmological models defined in Section 1.3. As per Table 1–1, in this work the normalization scale of the amplitude parameter is defined to be $k_0 = 0.002$ Mpc^{-1} and the corresponding amplitude is parameterized as A_s.

Finally, we wish to relate this primordial curvature perturbation to primordial perturbations in the gravitational potential, Φ, and to the fractional density fluctuation, $\delta \equiv \delta\rho/\rho_0$. The comoving curvature can be related most simply to the gravitational potential during epochs in which the equation of state parameter w (here not necessarily referring to dark energy) is constant, wherein the following relation applies:

$$\Phi = \frac{3+3w}{5+3w}\mathcal{R}, \tag{1.37}$$

transitioning from $\Phi = 2/3\mathcal{R}$ during radiation domination to $\Phi = 3/5\mathcal{R}$ in the matter-dominated epoch [41, 42, 43]. From this relation, and through Equation 1.36, we can relate the dimensionless power spectrum of the gravitational potential to the comoving curvature

$$\Delta^2_\Phi \propto \Delta^2_\mathcal{R} \propto k^{n_s-1}. \tag{1.38}$$

The gravitational potential is related to the fractional density perturbation through the Poisson equation:

$$\left(\frac{k}{a}\right)^2 \Phi = 4\pi G\rho\delta \tag{1.39}$$

such that

$$\Delta^2_\delta \propto k^{n_s+3} \tag{1.40}$$

and therefore, through Equation 1.35,

$$P_\delta \propto k^{n_s}. \tag{1.41}$$

Thus, simple inflationary models predict a period of accelerated expansion in the early universe, during which primordial quantum fluctuations are "stretched" to super-horizon scales. This process results in a spectrum of nearly scale-invariant, Gaussian density fluctuations which act as the seeds of structure formation in the universe.

1.5 Structure Growth and the Matter Power Spectrum

Having introduced a mechanism for generating primordial density fluctuations, we now explore the growth of cosmic structure. The details of this process can be found in most modern cosmology texts, including Dodelson [4], J. E. Peebles [5], Peacock [6], and Brandenberger [44], and will be summarized in this section. First, we will consider some fractional density fluctuation in an expanding, flat spacetime:

$$\delta \equiv \frac{\delta\rho}{\rho_0}, \tag{1.42}$$

where ρ_0 describes the homogeneous background matter density (where $\rho_0 = \rho_{\rm crit}\Omega_m a^{-3}$). In a non-expanding universe, the gravitational force will act upon this perturbation such that

$$\delta\ddot{\rho} \propto G\delta\rho, \tag{1.43}$$

where overdots represent derivatives with respect to time. Density perturbations in a non-expanding universe will grow exponentially in time. However, a static background universe is unstable. We will instead focus upon the growth of perturbations within an expanding universe, as defined by the FLRW metric. As we shall see, the effect of the spatial expansion will lie in the addition of a damping term to Equation 1.43.

In order to examine the evolution of the fractional energy density perturbation in an expanding universe, we will first shift our coordinate system to one that is constant with respect to the background expansion. As shown in Section 1.2, in these comoving coordinates we can map $\mathbf{x}(t) = a(t)\mathbf{r}(t)$ where $a(t)$ is the expansion factor and $\mathbf{r}(t)$ represents the comoving coordinate.

Perturbations with respect to the homogeneous background for the density, pressure, velocity, and potential fluid variables may be defined as follows:

$$\begin{aligned}
\rho(\mathbf{r},t) &= \rho_0(t) + \delta\rho(\mathbf{r},t) \\
p(\mathbf{r},t) &= p_0(t) + \delta p(\mathbf{r},t) \\
\mathbf{v}(\mathbf{r},t) &= \mathbf{v}_0(\mathbf{r},t) + \delta\mathbf{v}(\mathbf{r},t) \\
\Phi(\mathbf{r},t) &= \Phi_0(\mathbf{r},t) + \delta\Phi(\mathbf{r},t).
\end{aligned} \tag{1.44}$$

Since we are interested in the fractional energy density perturbations ($\delta \equiv \delta\rho/\rho_0$) we can rewrite the first line of Equations 1.44 as

$$\rho(\mathbf{r},t) = \rho_0(t)\left(1 + \delta(\mathbf{r},t)\right). \tag{1.45}$$

Treating the matter field as an ideal fluid, we can describe its dynamics through hydrodynamical equations. These equations consist of the continuity, Euler, and Poisson fluid equations, defined respectively in the physical frame by

$$\dot{\rho} + \nabla_x \cdot (\rho\mathbf{v}) = 0 \tag{1.46}$$

$$\dot{\mathbf{v}} + (\mathbf{v}\cdot\nabla_x)\mathbf{v} + \frac{1}{\rho}\nabla_x p + \nabla_x\Phi = 0 \tag{1.47}$$

$$\nabla_x^2\Phi = 4\pi G\rho. \tag{1.48}$$

These equations may be translated into the comoving frame via the transformations $\mathbf{x} = a\mathbf{r}$, $\nabla_x = \nabla_r/a$ and $\mathbf{u} = a\dot{\mathbf{r}}$, resulting in [44, 48, 41]

$$\dot{\rho} + 3\frac{\dot{a}}{a}\rho + \frac{1}{a}\nabla_r \cdot (\rho\mathbf{u}) = 0 \tag{1.49}$$

$$\dot{\mathbf{u}} + \frac{\dot{a}}{a}\mathbf{u} + \frac{1}{a}(\mathbf{u} \cdot \nabla_r)\mathbf{u} + \frac{1}{a\rho}\nabla_r p + \frac{1}{a}\nabla_r \Phi = 0 \tag{1.50}$$

$$\nabla_r^2 \phi = 4\pi G \rho_0 a^2 \delta, \tag{1.51}$$

where $\phi = \Phi - (2/3)\pi G \rho_0 a^2 r^2$ and is often referred to as the peculiar potential.

Prior to solving for the general case, we will first inspect the perturbed Poisson equation (1.51) and, following Dodelson [4], derive a relation between the fractional overdensity δ and the potential perturbation. Taking the Fourier transform of Equation 1.51 we may rearrange it as

$$\delta_k = \frac{k^2 \phi_k}{4\pi G \rho_m a^2}. \tag{1.52}$$

Substituting in expressions for the background matter density, $\rho_m = \rho_{crit}\Omega_m/a^3$, and the critical density, $\rho_{crit} = 3H_0^2/8\pi G$, we find

$$\delta_k = \frac{k^2 \phi_k a}{(3/2)\Omega_m H_0^2}, \tag{1.53}$$

which describes the relationship between the fractional overdensity and the potential perturbation. Examination of Equation 1.53 indicates that, for a fixed potential, δ_k varies inversely with Ω_m. This property will prove relevant when analyzing the results of the galaxy cluster analysis performed in later chapters.

Returning to the general case, and still working in comoving coordinates, the perturbed fluid equations may be solved for the evolution of adiabatic energy density perturbations in an expanding universe. Doing so yields

$$\ddot{\delta} + 2\frac{\dot{a}}{a}\dot{\delta} - \frac{c_s^2 \nabla^2}{a^2}\delta = 4\pi G \rho_0 \delta, \tag{1.54}$$

where $c_s^2 = \partial p / \partial \rho = 0$ for pressureless matter. Making use of Equation 1.7, Equation 1.54 can be re-arranged and expressed in Fourier space as

$$\ddot{\delta_k} + 2H\dot{\delta_k} = 4\pi G \rho_0 \delta_k. \tag{1.55}$$

This solution describes the differential equation which governs the evolution of density perturbations in an expanding universe. In particular, it is evident that when the expansion term is ignored ($H = 0$), Equation 1.55 reduces to the static universe approximation presented in Equation 1.43, resulting in the previously inferred exponential growth. The inclusion of the expansion-related damping term serves to modify this exponential growth where, in the matter-dominated epoch ($\Omega \simeq \Omega_m \simeq 1$), the general solution to Equation 1.55 reduces to

$$\delta_k(t) = c_1 t^{2/3} + c_2 t^{-1}, \tag{1.56}$$

where c_1 and c_2 are integration constants. The solution presented in Equation 1.56 represents both a decaying mode, which can be ignored at late times, and a growing mode where, during matter domination, $\delta_k(t) \propto a$. Thus, in an expanding universe the density fluctuations grow with a power law dependence rather than the exponential behaviour expected in a static universe. This growing mode is also independent of k indicating that perturbations at all scales grow at the same rate during the matter-dominated era.

At early times, the radiation energy density would dominate over the matter energy density. During this period, it can be shown that small-scale dark matter perturbations are able to grow logarithmically with time, a phenomenon which is sometimes referred to as the "Meszaros effect" [49, 44, 48].

We will now assume a convenient separation of the spatial and temporal dependence of the density perturbations such that

$$\delta(k,t) = \delta_{\mathrm{p}}(k)T(k)D(a(t)). \tag{1.57}$$

Here $\delta_{\mathrm{p}}(k)$ represents the primordial value of the overdensity, as set during inflation, $T(k)$ refers to the *transfer function*, which encompasses the scale-dependent behaviour of the perturbations, and we will introduce $D(a)$ as the cosmological *linear growth function*, which describes the scale-invariant growth of perturbations at late-times [8, 50]. For massive neutrinos this decomposition must be modified to include the effects of a scale-dependent growth factor [50]. Here we will derive a form for this late-time measure of cosmic structure growth and subsequently describe the behaviour of the transfer function.

By making use of Equations 1.13 and 1.14 we can rewrite Equation 1.55 in the form

$$\ddot{\delta} + 2H\dot{\delta} - \frac{3}{2}\Omega_m(z)H^2\delta = 0, \tag{1.58}$$

where $\Omega_m(z)$ is defined in terms of the present day matter density Ω_m such that

$$\Omega_m(z) = \frac{\Omega_m(1+z)^3}{E(z)^2}. \tag{1.59}$$

Here it is both conventional and convenient to recast the differential form for the growth equation in terms of the linear growth function $D(a)$. Employing a change of variables, we may rewrite Equation 1.58 in terms of $D(a)$; doing so we find

$$D'' + \left(\frac{\ddot{a}}{\dot{a}^2} + 2\frac{H}{\dot{a}}\right) D' - \frac{3\Omega_m H_0^2}{2a^3\dot{a}^2} D = 0, \tag{1.60}$$

where $' \equiv \frac{d}{da}$. This equation can be further simplified yielding

$$D'' + \left(\frac{d\ln H}{da} + \frac{3}{a}\right) D' - \frac{3\Omega_m H_0^2}{2a^5 H^2} D = 0. \tag{1.61}$$

For a matter-dominated universe, Equation 1.61 is exactly solvable and yields the previously described result, $D(a) \propto a$: matter fluctuations grow linearly with the scale factor. For more general cosmologies one also needs to take into account radiation, dark energy and perhaps even a time-varying equation of state. In these situations, the differential equation in Equation 1.61 must be solved numerically. For some cosmologies (e.g. standard ΛCDM, cosmological constant and cold dark matter) analytic solutions are possible. For these cosmologies we can express the growth function as a function of redshift as follows [51, 52]:

$$D(z) = \frac{5}{2}\Omega_m E(z) \int_z^\infty dz'(1+z')E(z')^{-3}. \tag{1.62}$$

Examples of the growth function are plotted in Figure 1–3.

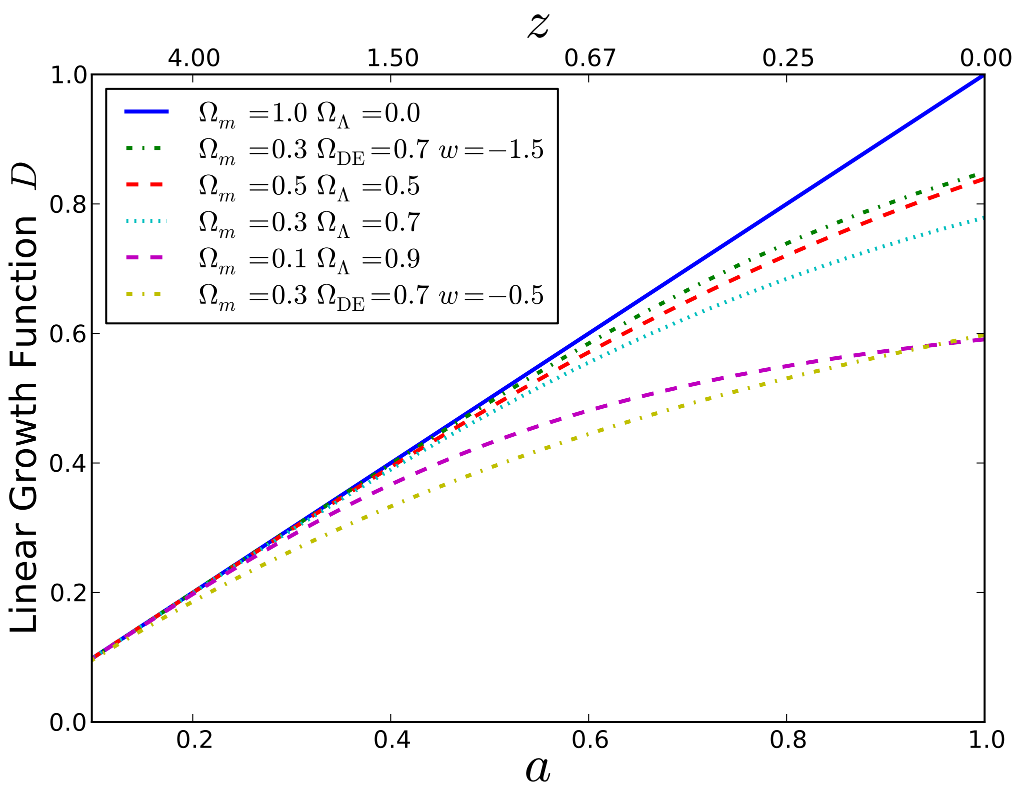

Figure 1–3: Linear growth function for a suite of ΛCDM and wCDM cosmologies. Cosmological models are plotted in decreasing order from the $\Omega_m = 1$ case, as per the legend. For an $\Omega_m = 1$ universe the growth function scales with a. Also shown is the late-time suppression of growth due to the addition of dark energy with various equations of state, where once again Ω_Λ refers to the cosmological constant dark energy density.

In this figure, the effect of dark energy on the linear growth rate is apparent: the suppression of growth at late times. In ΛCDM, the dark energy density is time-independent and thus one expects its effects to be most apparent at late times, when the matter density has decreased with the expansion to the point where dark energy is the dominant energy density in the universe. Thus, while insignificant at early times (as can be seen in Figure 1–3), the addition of dark energy in the ΛCDM model serves to suppress the growth of structure during the period in which the matter and dark energy densities are comparable and into the era of dark energy domination.

For the wCDM cosmological model, as presented in Section 1.3, we again examine regimes differentiated by the time-dependence of the dark energy density. Examples of growth functions within these regimes are plotted in Figure 1–3. As with the ΛCDM model, we find that the strongest growth occurs for a universe without a dark energy component where matter is able to quickly collapse and form structure.

For equations of state which predict a deceasing dark energy density ($-1 < w < -1/3$) we again find that the addition of dark energy suppresses the growth of structure compared with the $\Omega_m = 1$ case. However, within this regime, the magnitude of this suppression is increased when compared with the $w \equiv -1$ case described above. The origin of this increased suppression lies in the evolution of the dark energy density, as defined in Equation 1.17. When normalizing to the present day dark energy density of the ΛCDM case, cosmologies with equations of state $-1 < w < -1/3$ must have possessed larger dark energy densities in the past. This increased dark energy density would serve to suppress the gravitational collapse of matter at early times and thus decreases the amplitude of the growth function at late times, as shown in Figure 1–3.

For cases of increasing dark energy density ($w < -1$) we observe a behaviour opposite to that just described for the $-1 < w < -1/3$ regime. In order to produce a similar present-day dark energy density, cosmologies with $w < -1$ must have originated with a reduced density of dark energy. This implies that the growth of structure in such universes would be similar to that of the matter-only case until such a time as the dark energy density begins to dominate over the matter component. Thus, we find that the growth rate of cosmic structure is a means for placing constraints upon the nature of the cosmological model and the parameters which define it.

Having presented an expression for the linear growth function we will now introduce the scale-dependent transfer function $T(k)$, as presented in Equation 1.57. In Section 1.4, a period of cosmic inflation was shown to have seeded potential fluctuations on all scales, including modes with wavelengths larger than the current cosmic horizon (as defined by Equation 1.21). As the universe gets older, the horizon grows and these modes will become smaller than the horizon. In this fashion, the small scale modes will cross the horizon earlier than large scale modes.

An important delimiter in this horizon-crossing timeline occurs when the matter and radiation energy densities are equivalent, a period known as matter-radiation equality, occurring at redshift z_{eq}. For modes which enter the horizon during the radiation-dominated phase, the matter perturbation remains roughly constant and thus the associated potential decays with the expansion. The epoch of matter-radiation equality can be approximated as [53]

$$z_{eq} = 2.50 \times 10^4 \Omega_m h^2 \Theta_{2.7}^{-4}, \tag{1.63}$$

where $\Theta_{2.7}$ is the temperature of the Cosmic Microwave Background normalized to 2.7 K and the scale of the particle horizon at that redshift may be written as

$$k_{eq} \equiv \left(2\Omega_m H_0^2 z_{eq}\right)^{1/2} = 7.46 \times 10^{-2} \Omega_m h^2 \Theta_{2.7}^{-2} \text{ Mpc}^{-1}. \tag{1.64}$$

Thus small-scale perturbations, which cross the horizon during this radiation-dominated phase, will appear suppressed compared with those that enter after; this behaviour is encoded in the transfer function. In the era of matter domination the perturbations, as shown in Section 1.5, grow with the scale factor. In this fashion, the scale of matter-radiation equality is imprinted upon the power spectrum. This scale-dependence is described by the transfer function $T(k)$, which is presented in Figure 1–4. While analytic approximations for the transfer function exist (see for example Eisenstein and Hu [53], and Eisenstein and Hu [50]) it may also be calculated numerically. A common and efficient routine for executing this calculation is the Code for Anisotropies in the Microwave Background (CAMB)[1] [54]. Examples of the transfer function for various cosmological models are plotted in Figure 1–4.

We now wish to evolve the initial power spectrum for the matter overdensity to the current epoch in the form of the *matter power spectrum*. Following from Equation 1.57, we will separate the evolution of the matter power spectrum into a scale-dependent and redshift-dependent component. Leading from Equations 1.34

[1] `http://camb.info/`

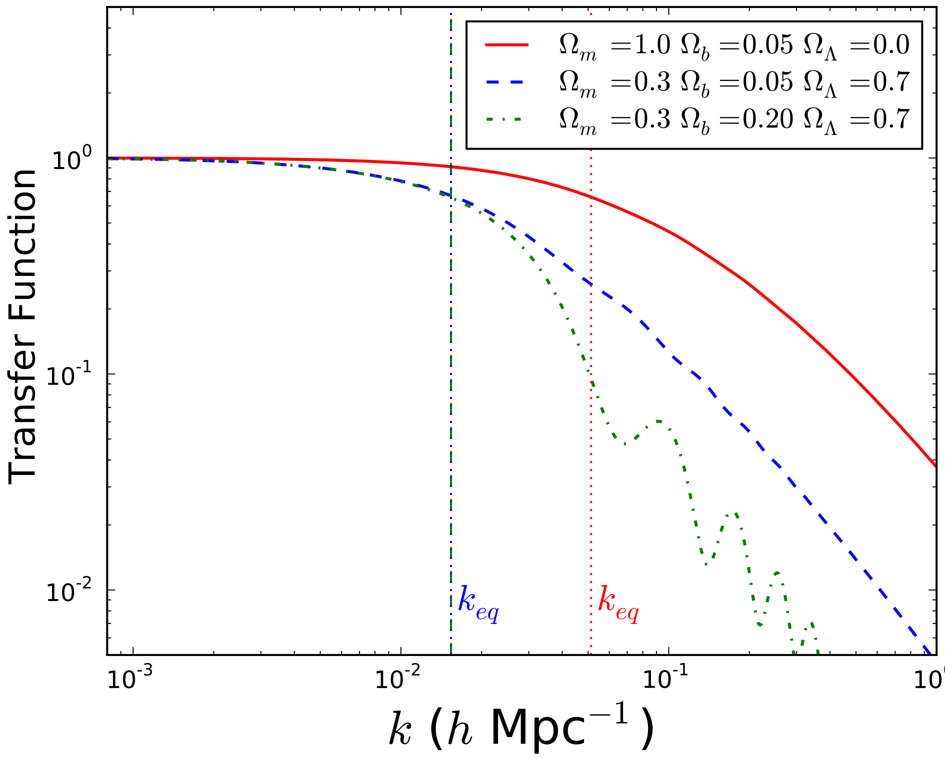

Figure 1–4: Transfer function for three cosmologies with differing matter contents, computed through CAMB [54]. Also shown is the matter-radiation equality scale for each cosmology. At small scales the baryon acoustic oscillations and damping are evident.

and 1.57, we will express the matter power spectrum at given scale and redshift as

$$P(k,z) \propto \delta(k,z)^2 \propto P_{\delta_{\rm p}}(k)T^2(k)D_1(z)^2 \propto k^n T^2(k)D_1(z)^2, \tag{1.65}$$

where $T(k)$ again represents the scale-dependent transfer function and $D_1(z)$ is the linear growth function, normalized to unity today:

$$D_1(z) \equiv \frac{D(z)}{D(z=0)}. \tag{1.66}$$

Through calculations of both the growth function and transfer function, we are able to compute the matter power spectrum, as defined in Equation 1.65. To do so, we will again make use of the numerical calculation performed by the CAMB software package. This will allow us to calculate the matter power spectrum for any input cosmology, across a wide range of scale and redshift. This ability will prove invaluable when calculating expected galaxy cluster counts in Chapter 4. Matter power spectra for the cosmologies represented in Figure 1–4 are presented in Figure 1–5.

One final quantity of note is the variance in the linear density field when smoothed on a given physical scale. This quantity is defined as

$$\sigma_R^2 = \frac{1}{2\pi^2} \int_0^\infty k^2 P(k) W(kR)^2 dk, \tag{1.67}$$

where the length scale R can be related to mass M through the cosmological background density ($\bar{\rho}_m = \Omega_m \rho_{crit}$) so that

$$R = \left(\frac{3M}{4\pi\bar{\rho}_m} \right)^{1/3} \tag{1.68}$$

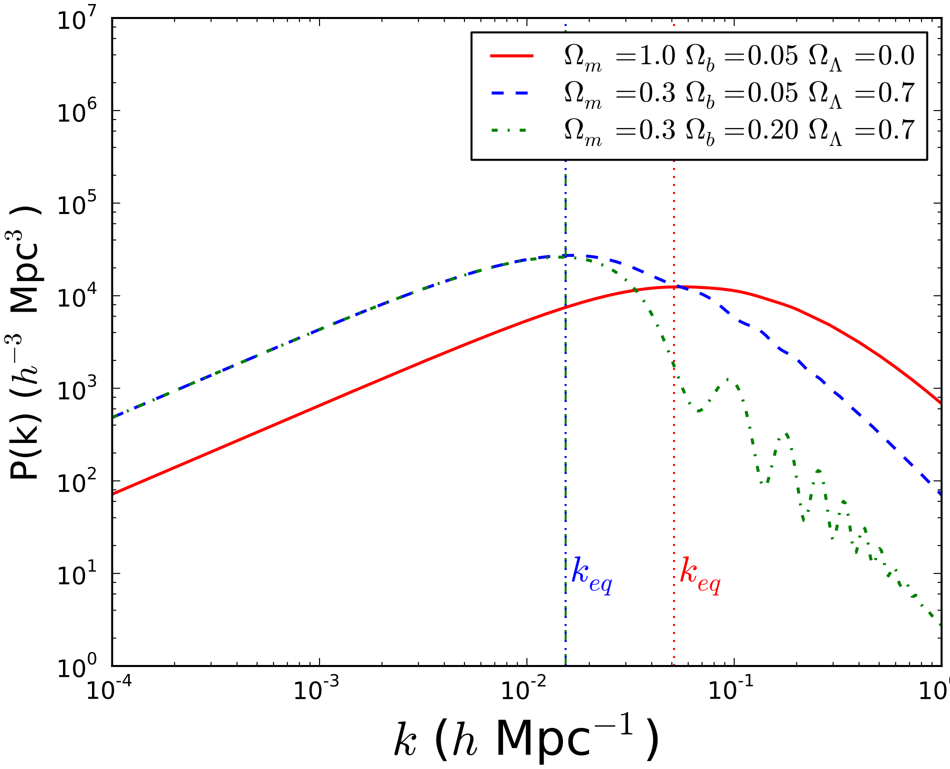

Figure 1–5: Matter power spectra for the three cosmologies presented in Figure 1–4. Units for the spectra are h^{-3} Mpc^3 and the matter-radiation equality scale is again indicated for all cosmologies. Spectra are normalized to recent results from the WMAP experiment [11, 18]. As indicated by Equation 1.53, for a fixed potential the amplitude of the matter power spectrum varies inversely with the matter density in the universe.

and W is the window function over which the linear matter power spectrum is smoothed, defined as the Fourier transform of the real-space, spherical top-hat function:

$$W(kR) = 3\left(\frac{\sin(kR)}{(kR)^3} - \frac{\cos(kR)}{(kR)^2}\right). \tag{1.69}$$

The rms of the smoothed density field is commonly normalized at $8h^{-1}$ Mpc where its value is expected to be of order unity; this quantity is denoted as σ_8. Examples of this function are presented in Figure 1–6.

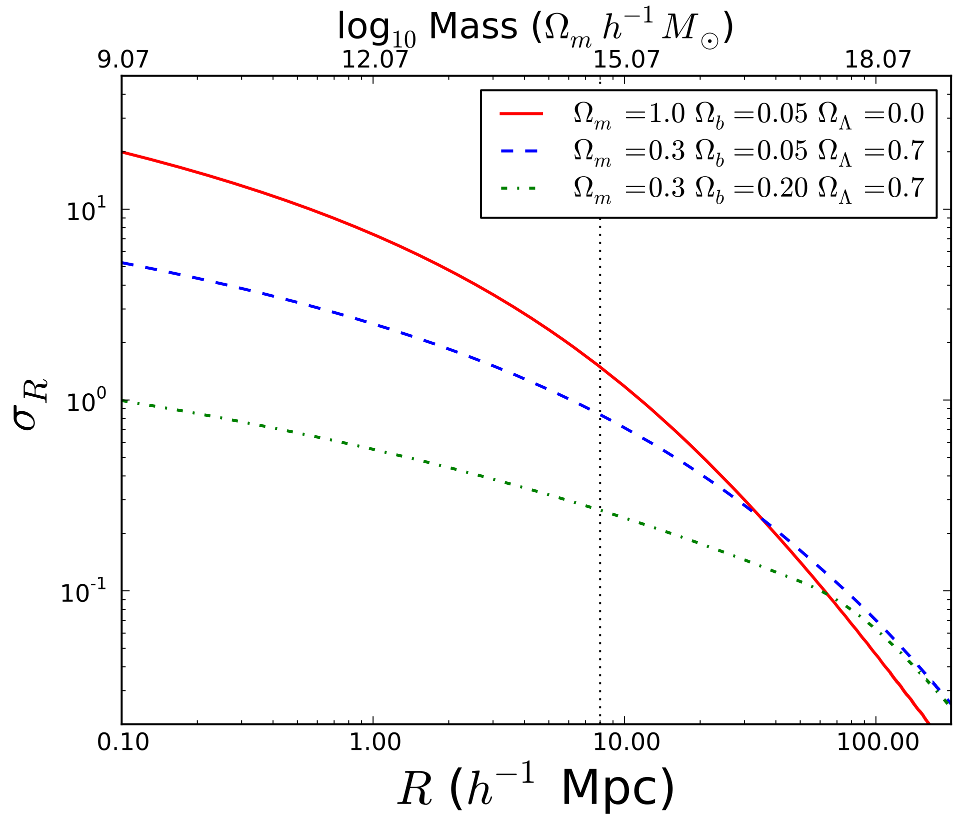

Figure 1–6: Variance in the linear matter density field as a function of smoothing radius/mass for the cosmologies and normalizations presented in Figure 1–5. The common normalization scale of $8h^{-1}$ Mpc is marked by the black dotted line.

1.6 Non-Gaussian Fluctuations

In Section 1.4 the simple, single-field inflationary model was presented as a model which produces a spectrum of primordial fluctuations whose distribution is predicted to be Gaussian in nature. In this section we will expand upon this prediction and review the implications of possible non-Gaussian features in these primordial fluctuations. A cosmology possessing such features will be considered to be distinct from the fiducial ΛCDM model, and will be examined further in Chapter 7. The aim of this investigation will be to motivate and examine the effects of primordial non-Gaussianity on the late-time density field, as probed by galaxy clusters. To do so, we will introduce a parameterization for the degree of primordial non-Gaussianity and describe its predicted value for the simple, single-field inflationary model introduced earlier.

In Section 1.4 we introduced the concept of inflation through a single scalar field, referred to as the inflaton. We described that under certain conditions such a scalar field can cause an early inflationary period of exponential expansion in the universe. One key aspect to these conditions lay in the slow-roll approximation wherein the potential energy of the inflaton field must dominate over its kinetic term. In such situations the inflaton field is able to slowly "roll" down its potential from an initial "false" vacuum towards the "true" vacuum state, precipitating an exponential cosmic expansion during this period [4, 41, 42, 43, 44]. Throughout this accelerated expansion, quantum fluctuations in the inflaton field would produce fluctuations in the energy density which are predicted to be very nearly Gaussian in nature. The physical wavelength of these perturbations ($\lambda = 2\pi a/k$) would then be stretched by the exponential expansion until the perturbations exit the horizon (which itself is nearly constant throughout inflation). The result of this process is a nearly scale-invariant spectrum of Gaussian fluctuations which remain to act as the seeds for the growth of structure in the universe.

While a Gaussian signature in the density perturbations arises naturally out of single-field inflationary models, this characteristic is not necessarily shared amongst all models. As reviewed in Bartolo et al. [43], there are a variety of inflationary scenarios which produce appreciable non-Gaussian signals. For example, hybrid or multi-field inflationary models containing more than one inflationary scalar field have been shown to be capable of producing significant non-Gaussianity [55, 56]. For these models it is common to express these non-Gaussian features in terms of the non-Gaussianity parameter: f_{NL}. Within this parameterization, the non-Gaussianity is modeled as an additional skew term to the underlying Gaussian field. This generalized formulation, as adopted in Bartolo et al. [43] and used in many others (e.g. [57, 58, 59, 60, 61, 62, 63, 64]), casts f_{NL} as a dimensionless parameter and defines the non-Gaussian potential as

$$\Phi(\mathbf{x}) = \Phi_G(\mathbf{x}) + f_{NL}\left(\Phi_G^2(\mathbf{x}) - \langle\Phi_G^2\rangle\right), \tag{1.70}$$

where Φ_G is a Gaussian field and this form of non-Gaussianity is commonly referred to as the *local* form whereby both sides of Equation 1.70 are evaluated at the same point in space [65]. When presented in terms of the comoving curvature perturbation $\mathcal{R}$, Equation 1.70 takes the form [66, 67]

$$\mathcal{R}(\mathbf{x}) = \mathcal{R}_G(\mathbf{x}) + \frac{3}{5} f_{NL}\left(\mathcal{R}_G^2(\mathbf{x}) - \langle\mathcal{R}_G^2\rangle\right) \tag{1.71}$$

where the prefactor of 3/5 is conventional and related to the correspondence between the comoving curvature perturbation and the gravitational potential during the matter-dominated regime: $\Phi = (3/5)\mathcal{R}$, as presented earlier.

More thorough analyses of the expected primordial non-Gaussianity present in single field slow-roll inflationary models have been performed in Acquaviva et al. [68], Bartolo et al. [43], and Maldacena [66]. In these works the prediction of a very nearly Gaussian spectrum of perturbations for single field slow roll inflation is upheld, where deviations from this condition are found to be of the order $f_{NL} \lesssim 1$.

The motivation for constructing such a simplified form for primordial non-Gaussianities is that it places few specific claims or restrictions upon the underlying inflationary model. Non-Gaussianities can arise from a variety of sources including, for example, non-linear coupling between the inflationary field or fields and the matter and radiation during the post-inflationary phase [43, 55, 56]. In this formulation we are interested mainly in constraining the level of non-Gaussianity present in the density perturbation spectrum without proposing a specific mechanism for its creation. This approach is similar to that described for the wCDM cosmological model presented in Section 1.3 where, as with the dark energy equation of state parameter w, we are interested in deviations from the fiducial case of $f_{NL} = 0$ (or $w = -1$). As we shall explore in future chapters, one of the aims of this work will be to constrain the level of primordial non-Gaussianity using the abundance of massive galaxy clusters in the late-time universe.

CHAPTER 2
Halo Mass Functions

2.1 Introduction

An important aspect of the analysis presented in this work lies in formulating a comparison between the predicted and observed abundance of structure in the late-time universe. As such, we require a means by which we may calculate these theoretical abundances. In this chapter we will examine methods for performing such a calculation.

Unlike the nearly Gaussian density perturbations present in the early universe and described in Section 1.5, the late-time distribution of structure in the universe appears decidedly more complex. As the perturbations grow they cease to satisfy linear perturbation theory and enter the non-linear domain, where their evolution can become difficult to analyze. We will explore methods of modeling this non-linear density field with the aim of accurately predicting the abundance of collapsed structure as a function of mass, redshift and cosmology.

We will first explore what defines the conditions under which an object can be said to have "collapsed". This process will lead to an estimation of the fraction of volume which has undergone collapse on a given a scale at a cosmic epoch. From this calculation we will introduce the concept of the *halo mass function* as an estimator for the abundance of cosmic structure for a given cosmology, described in terms of the dark matter halos in which structure forms.

In this process, we will introduce modern forms of the halo mass function with the aim of selecting a suitable candidate for our analysis. The practice of calibrating mass functions to numerical simulations will be examined and convenient measures for halo masses will be explored.

2.2 Press-Schechter Formalism

Estimating the halo mass function was pioneered by Press and Schechter [69], using what is now often referred to as the Press-Schechter (PS) formalism. This approach assumes that the location and abundance of collapsed structures at some later time will correspond to points in the initial density field that, once smoothed on some scale and allowed to grow with time, exceed a threshold value required for collapse. This threshold linear overdensity value will be denoted as δ_c where, for spherical collapse models, the perturbation collapse condition is $\delta_c \simeq 1.69$ in the linearly evolved density field [70]. Rewriting Equation 1.68 in terms of a smoothed mass scale, $M = \frac{4}{3}\pi\bar{\rho}_m R^3$, we can express the smoothed matter variance of Equation 1.67, σ_R, in terms of a corresponding mass scale, σ_M. From the predicted Gaussian nature of the density field imposed by inflation we can express the probability density function (PDF) of the smoothed density field δ_M as

$$P(\delta_M) = \frac{1}{\sqrt{2\pi\sigma_M(z)^2}} \exp\left(\frac{-\delta_M^2}{2\sigma_M(z)^2}\right), \tag{2.1}$$

where the redshift dependence of $\sigma_M(z)$ is defined through the linear growth function such that $\sigma_M(z) = \sigma_M D_1(z)$.

As shown in Press and Schechter [69], the probability for the smoothed density field to exceed the condition for collapse may be expressed as

$$P(\delta_M > \delta_c) = \frac{1}{\sqrt{2\pi\sigma_M(z)^2}} \int_{\delta_c}^{\infty} \exp\left(\frac{-\delta_M^2}{2\sigma_M(z)^2}\right) d\delta_M = \frac{1}{2}\mathrm{erfc}\left(\frac{\delta_c}{\sqrt{2}\sigma_M(z)}\right). \quad (2.2)$$

Here it will be convenient to define $\nu_c \equiv \delta_c/\sigma_M(z)$ so that the above equation may be rewritten as

$$P(\delta_M > \delta_c) = \frac{1}{2}\mathrm{erfc}\left(\frac{\nu_c}{\sqrt{2}}\right) \quad (2.3)$$

where $\nu_c \to 0$ as $\sigma_M \to \infty$ such that $\int_0^{\infty} P(\delta_M > \delta_c) = 1/2$. At arbitrarily low mass all matter should be contained within a halo, however, the PS approach only accounts for half of those objects. This is referred to as the "cloud-in-cloud" problem whereby a region which is smoothed at a particular threshold may be below δ_c but may exceed it when smoothed at a larger scale. More rigorous derivations (e.g. [71, 72]) account for this factor correctly.

This quantity (Equation 2.3) may be differentiated with respect to mass and divided by the volume ($V = M/\bar{\rho}_m$) to yield the differential number density within a mass range $d\ln M$ at a redshift z:

$$\frac{dn}{d\ln M} = \frac{\bar{\rho}_m}{M}\frac{d}{d\ln M}\mathrm{erfc}\left(\frac{\nu_c}{\sqrt{2}}\right) \quad (2.4)$$

$$= \sqrt{\frac{2}{\pi}}\frac{\bar{\rho}_m}{M}\frac{d\ln\sigma^{-1}}{d\ln M}\nu_c \exp(-\nu_c^2/2), \quad (2.5)$$

where the mass and redshift dependence of both $\sigma(M,z)$ and $\nu_c(M,z)$ have been suppressed for clarity. We will refer to this expression as the Press-Schechter (PS) mass function.

It will also be convenient to define a general mass function as follows:

$$\frac{dn}{d\ln M} = f(\sigma)\frac{\bar{\rho}_m}{M}\frac{d\ln\sigma^{-1}}{d\ln M}, \tag{2.6}$$

where the mass and redshift dependence of $\sigma(M,z)$ is implicit and the definition of $f(\sigma)$ will be specific to the mass function in question. In the PS formulation this function is defined to be (as per Equation 2.5)

$$f_{PS}(\sigma) = \sqrt{\frac{2}{\pi}}\frac{\delta_c}{\sigma}\exp\left[-\frac{\delta_c^2}{2\sigma^2}\right] \tag{2.7}$$

and is normalized such that

$$\int_{-\infty}^{\infty} f_{PS}(\sigma) d\ln\sigma^{-1} = 1. \tag{2.8}$$

Evident in this expression, and displayed in Figure 2–1, is the asymptotic behaviour of the PS mass function. At high mass the mass function is exponentially damped, indicating that massive collapsed systems are exceedingly rare, while at low mass the function displays a power-law dependence, predicting an increasingly large number of low mass objects. This behaviour reveals the sensitivity with which the mass function is able to probe the high mass region, which, as will be discussed in Chapter 4, renders the mass function a useful tool for cosmological studies.

2.3 Beyond Press-Schechter

Although the PS mass function represents the overall behaviour of the halo mass function, some assumptions used in its derivation (e.g. spherical collapse) render it insufficient for use in a precise quantitative analysis. Fortunately, further

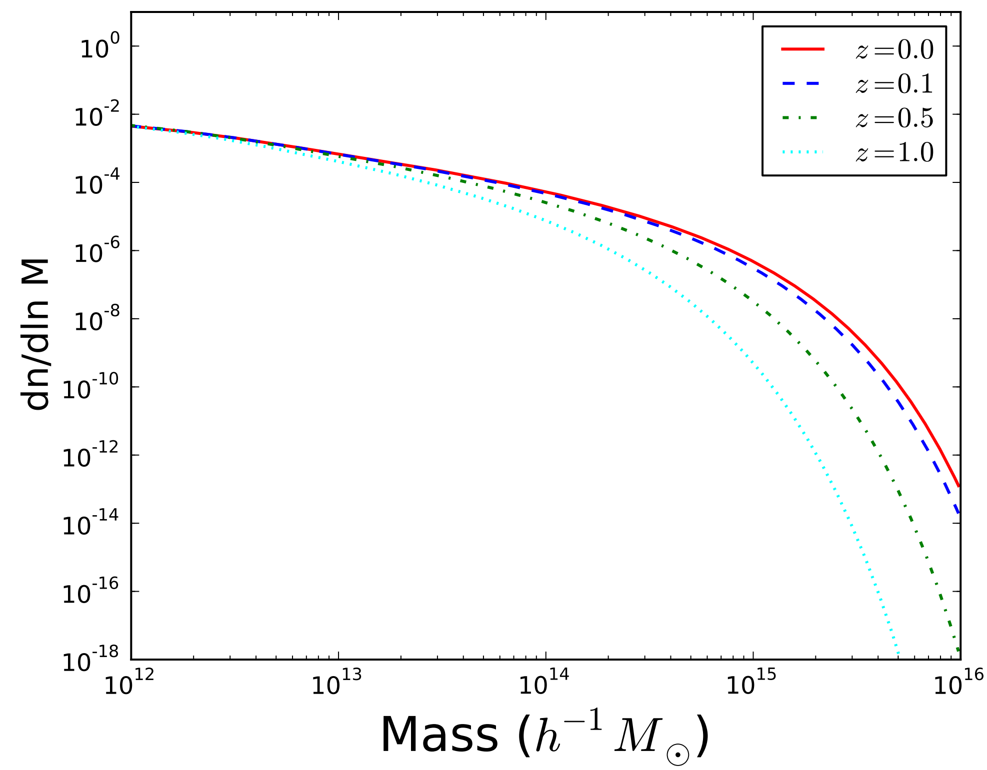

Figure 2–1: Differential number counts for the Press-Schechter mass function plotted as a function of both mass and redshift for the $\Omega_m = 0.3$, ΛCDM cosmology presented in Figures 1–4 and 1–5. At high mass the exponential form of the mass function is apparent.

refinements to the halo mass function are possible [71, 72, 73]. The Sheth-Tormen (ST) mass function is modeled to be similar in form to the PS mass function but has been calibrated through comparisons to numerical simulations of structure formation [72, 73]. The ST mass function can be written in terms of Equation 2.6 as

$$f_{ST}(\sigma) = A\sqrt{\frac{2a}{\pi}}\left[1 + \left(\frac{a\delta_c^2}{\sigma^2}\right)^{-p}\right]\frac{\delta_c}{\sigma}\exp\left[-\frac{a\delta_c^2}{2\sigma^2}\right], \tag{2.9}$$

where a and p are fit to simulated data and $A = \left[1 + \frac{2^{-p}\Gamma(0.5-p)}{\sqrt{\pi}}\right]^{-1}$ is defined so that the normalization of Equation 2.8 holds. This function demonstrates qualitative similarities with the PS mass function while having been calibrated to better agree with simulated data [73]. Throughout this section, both the redshift and mass dependence of $\sigma(M, z)$ will be left implicit.

Thus, refinements to the halo mass function are achievable through comparison with, and calibration to N-body simulations of cosmological structure formation. Examples of such simulations include the Millennium Simulation [74] and the MareNostrum Universe simulation [75]. These simulations model the evolution of cosmic structure by computing, through a variety of techniques, the gravitational interactions of billions of simulation particles. Through these calculations, the formation of structure within enormous ($\sim$Gpc^3) cosmological volumes may be modeled [74, 75, 76].

By calculating the interactions between particles, purely gravitational in the case of collisionless dark matter, these simulations are able to follow the growth of large scale structure in the universe across a wide range in mass. By performing these simulations with different input cosmological parameters, the cosmological dependence of the halo mass function may be modeled [76].

When using these simulations it is necessary to define the mass of a halo in terms of the simulated particles. There are two common approaches to measuring the mass of a halo within an N-body simulation.

The first method is known as the friends-of-friends (FOF) algorithm [77]. It has a single free parameter, the linking length parameter b, which sets the linking length equal to $b\bar{l}$, where $\bar{l}$ is the mean interparticle separation in the simulation. All particles separated by the linking length or less from each other are considered to be members of the halo. The advantage to this method lies in its simplicity (having a single free parameter), its speed, and its insensitivity to halo shape. It is, however, possible for the FOF algorithm to link distinct halos if there appears to be a bridge of particles between them. Another drawback is that the boundaries of FOF-identified halos will not in general correspond with isodensity contours [78].

A second method of halo identification is the Spherical Overdensity (SO) method [79]. It has as a free parameter Δ which denotes the ratio of the mean density of the (spherically averaged) halo to the mean (or critical) density of the universe. We can relate this ratio to the mass of the halo as follows:

$$M_{\Delta} = \frac{4\pi}{3} R_{\Delta}^{3} \Delta \bar{\rho_m}, \tag{2.10}$$

where the halo mass M_{Δ} depends explicitly upon the choice of Δ and decreases with increased Δ.

In the SO algorithm, candidate halo locations are identified and a sphere is grown around that location until the mean density in the sphere equals Δ times the mean (or critical) density of the universe. In this formulation, it is often necessary to iterate this process in order to properly center the spherical halo [80, 79]. The SO halo finding method can be more computationally intensive than the FOF method but it is less likely to erroneously link nearby independent halos and can be simpler to relate to galaxy cluster observables than the FOF method.

In Jenkins et al. [80] a large suite of N-body simulations were used to derive a fitting function for the halo mass function; we will refer to this as the Jenkins mass function. In this work, they employed both the FOF and the SO halo finding algorithms and made comparisons to both the PS and ST mass functions. They found that the following fitting functions reproduced the simulated results for a ΛCDM cosmology to better than 20% accuracy, offering significant improvements over previous mass functions:

$$\begin{aligned} f_{Jenkins}(\sigma, b = 0.164) &= 0.301 \exp\left[-\left|\ln \sigma^{-1} + 0.64\right|^{3.88}\right] \\ f_{Jenkins}(\sigma, \Delta = 324) &= 0.316 \exp\left[-\left|\ln \sigma^{-1} + 0.67\right|^{3.82}\right]. \end{aligned} \tag{2.11}$$

While providing accurate results over a wide range of masses, the Jenkins mass function is limited by being fitted at fixed values for both the SO and FOF halo-identification methods. This renders it difficult to apply this mass function to analyses in which the cluster mass definition differs from the values presented in Equation 2.11.

In Tinker et al. [76], the authors derived a mass function through measurements of a large set of cosmological simulations, representative of the ΛCDM cosmological model; we will refer to this as the Tinker mass function. The Tinker halo mass fitting function is described as

$$f_{Tinker}(\sigma, \Delta) = A(\Delta) \left[\left(\frac{\sigma}{b(\Delta)} \right)^{-a(\Delta)} + 1 \right] e^{-c(\Delta)/\sigma^2}, \tag{2.12}$$

where A, a, b, and c are fitted parameters that, unlike the ST approach, are not required to satisfy Equation 2.8. A key advantage of this approach is that unlike the Jenkins mass function, the fitting parameters for the Tinker mass function are also functions of the SO parameter Δ. In this approach, the resulting mass function is not limited to a single halo mass definition but can instead accommodate a variety of definitions. The Δ-dependence of the fitted parameters is obtained through a spline interpolation. They are also well-approximated via the following formulae:

$$A(\Delta) = \begin{cases} 0.1(\log\Delta) - 0.05 & \text{if } \Delta < 1600 \\ 0.26 & \text{if } \Delta \geq 1600 \end{cases} \tag{2.13}$$

$$a(\Delta) = 1.43 + (\log\Delta - 2.3)^{1.5}) \tag{2.14}$$

$$b(\Delta) = 1.0 + (\log\Delta - 1.6)^{-1.5}) \tag{2.15}$$

$$a(\Delta) = 1.2 + (\log\Delta - 2.35)^{1.6}). \tag{2.16}$$

Along with being Δ-dependent, the fitting parameters in Equation 2.12 were also found to vary as a function of redshift [76]. This evolution with redshift is described as follows:

$$A(z) = A_0(1+z)^{-0.14} \tag{2.17}$$

$$a(z) = a_0(1+z)^{-0.06} \tag{2.18}$$

$$b(z) = b_0(1+z)^{\alpha} \tag{2.19}$$

$$\log\alpha(\Delta) = -\left(\frac{0.75}{\log(\Delta/75)}\right)^{1.2}. \tag{2.20}$$

These dependencies indicate that, unlike the Jenkins mass function, the Tinker mass function form $f(\sigma)$ is a redshift-dependent quantity, a characteristic which is also observed in other simulations [81, 82]. It is argued in Tinker et al. [76] that this evolution may be due to the evolution of halo density profiles and merger rates. The Tinker halo mass function is presented in Figure 2–2 together with the Press-Schechter, Sheth-Tormen and Jenkins mass function.

The end result of the Tinker simulation-calibrated formalism is a mass function which forecasts the abundance of halos with masses in the range $10^{10.5}\ h^{-1}M_{\odot} \lesssim M \lesssim 10^{15.5}\ h^{-1}M_{\odot}$ with an accuracy of $\lesssim 5\%$ when compared with simulation [76]. The galaxy clusters utilized in this analysis are not expected to lie outside this range, however, it is noted in Tinker et al. [76] that this mass range may be extended at the expense of some loss in accuracy [83, 84]. The high fidelity with which the Tinker halo mass function is able to reproduce simulated cluster abundances at varied cosmologies, as well as its adaptability in cluster mass definition renders the Tinker mass function a powerful tool. As such, it will act as an integral component in our analysis of galaxy cluster abundances, as will be presented in Chapters 5, 6, and 7.

2.4 Non-Gaussian Mass Functions

Although the Tinker mass function presented in the previous section offers a precise and well-calibrated measure of cosmological halo abundances, it does so with the underlying premise of an initial set of perturbations which are purely Gaussian in nature. In the following subsections we will explore the effects of non-Gaussian density perturbations on the predicted abundance of galaxy clusters in the universe.

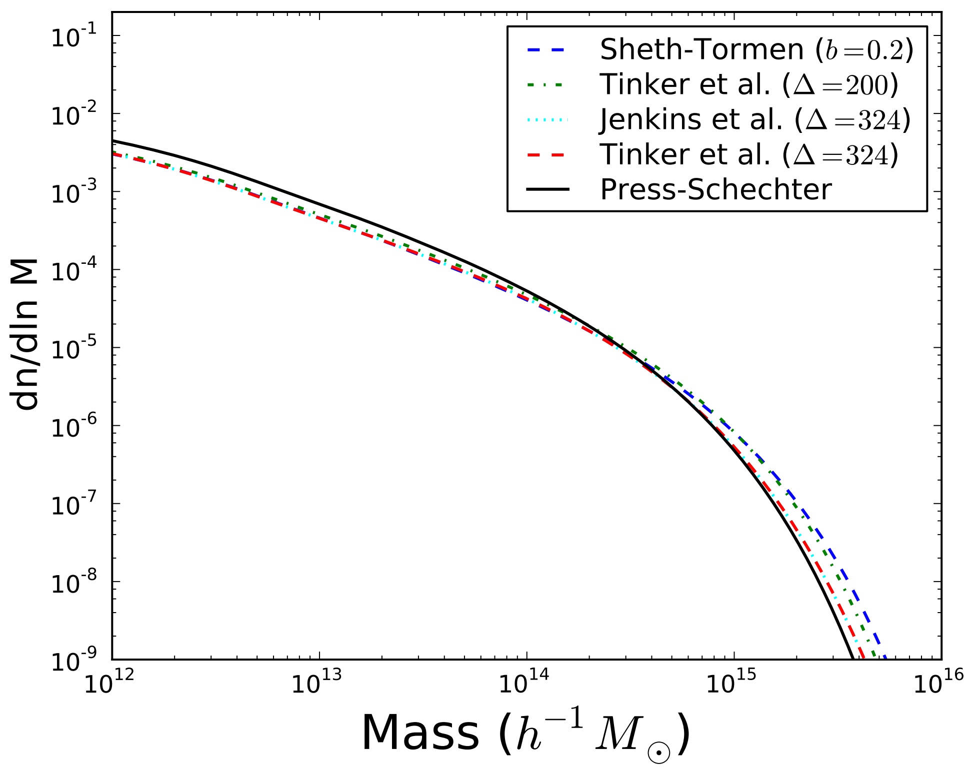

Figure 2–2: Differential number counts for the Press-Schechter, Sheth-Tormen, Jenkins and Tinker halo mass function at $z = 0$ for the $\Omega_m = 0.3$, ΛCDM cosmology presented in Figures 1–4 and 1–5. For simulation-calibrated mass functions representative values of the halo mass definition are noted. The Tinker and Jenkins mass function show good agreement for $\Delta = 324$ while the Sheth-Tormen $b = 0.2$ and Tinker $\Delta = 200$ mass functions show reasonable agreement for $M \lesssim 2 \times 10^{15} h^{-1} M_\odot$. The Press-Schechter mass function is included for illustrative purposes.

While there exists an infinite variety of non-Gaussian forms, we will investigate the local form of non-Gaussianity, as described in Section 1.6 and characterized by Equation 1.70. In these subsections we will review three separate techniques for modifying the halo mass function to include the effects of primordial non-Gaussianity.

The resulting functions will be employed in our analysis of galaxy cluster data, as presented in Chapter 7.

2.4.1 LoVerde and Smith (LVS) Mass Function

The first of these techniques uses the Press-Schechter formulation, as described in Section 2.2, extending it to the non-Gaussian case. Since the standard Press-Schechter (PS) mass function is acknowledged as a poor fit to N-body simulations, this approach derives the ratio of the non-Gaussian to the standard Gaussian PS mass function and then applies this ratio to the Gaussian form of a better-calibrated mass function (such as the Tinker mass function):

$$n_{\text{Tinker},NG} = \left(\frac{n_{\text{PS},NG}}{n_{\text{PS},G}}\right) n_{\text{Tinker},G}, \tag{2.21}$$

where n refers to the differential number count and the subscripts G and NG refer to the Gaussian and non-Gaussian forms respectively. This technique has been explored in numerous works (e.g. Enqvist et al. [85], Grossi et al. [60], LoVerde and Smith [62], and Matarrese et al. [86]) where here we will examine a recent revision presented in LoVerde and Smith [62], the results of which we will refer to hereafter as LVS.

The LVS approach re-examines the assumption of an initial field of Gaussian perturbations which lay as the foundation in Equation 2.1. Here we will summarize the technique adopted in LoVerde and Smith [62], re-expressing the PDF of collapsed halos (defined in Equation 2.2) as the fraction of volume contained in collapsed halos such that

$$F(M) = \int_{\nu_c}^{\infty} \rho(\nu, M) d\nu, \tag{2.22}$$

where, as per our earlier notation, $\nu_c = \delta_c/\sigma_M(z)$ and now $\nu = \delta_M/\sigma_M(z)$. As in Section 2.2, the Press-Schechter mass function can then be described as

$$\frac{dn}{d\ln M} = -2\frac{\bar{\rho}_m}{M}F'(M,z), \tag{2.23}$$

where primes will denote derivative with respect to mass M and the prefactor of 2 corresponds to the correction noted in Section 2.2. For Gaussian perturbations, as explored in Section 2.2, we showed that $\rho(\nu, M) = (2\pi)^{-1/2}\exp(-\nu^2/2)$ such that $F'(M,z)$ was analytically calculable, resulting in Equation 2.5. In this case, $\rho(\nu, M)$ is a non-Gaussian distribution. This can be expressed in terms of the Edgeworth expansion:

$$F(x) = \exp\left[\sum_{n=3}^{\infty}\frac{(-1)^n}{n!}\kappa_n\frac{d^n}{dx^n}\right]\frac{1}{\sqrt{2\pi}\sigma}\exp\left[-\frac{(x-\mu)^2}{2\sigma^2}\right], \tag{2.24}$$

where μ and σ^2 are the mean and variance and κ_n are the *reduced cumulants* which define the higher order properties of the distribution. These reduced cumulants are defined as [62, 61, 87]

$$\kappa_n(M) = \frac{\langle\delta_M^n\rangle_{\rm c}}{\langle\delta_M^2\rangle^{n-1}} \qquad \text{for } n \geq 3, \tag{2.25}$$

where $\langle\delta_M^n\rangle_{\rm c}$ is the $n^{\rm th}$ cumulant and $\kappa_n(M)$ are defined to be redshift-independent. For a distribution with zero mean, the first four cumulants may be described in terms of the moments of the distribution as [61, 87]

$$\langle\delta_M\rangle_{\rm c} = 0, \qquad \langle\delta_M^2\rangle_{\rm c} = \sigma_M^2, \tag{2.26}$$

$$\langle\delta_M^3\rangle_{\rm c} = \langle\delta_M^3\rangle, \quad \langle\delta_M^4\rangle_{\rm c} = \langle\delta_M^4\rangle - 3\sigma_M^2. \tag{2.27}$$

In the case of $\rho(\nu, M)$, the Edgeworth expansion can be applied to yield

$$\rho(\nu, M) = \frac{\exp(-\nu^2/2)}{(2\pi)^{1/2}}(1 + p_1(\nu, M) + p_2(\nu, M) + \cdots). \tag{2.28}$$

Here p_1 represents terms which are first order in f_{NL} while p_2 represents the second order terms, defined as [62]

$$\begin{aligned} p_1(\nu, M) &= \frac{1}{6}\kappa_3(M)H_3(\nu) \\ p_2(\nu, M) &= \frac{1}{24}\kappa_4(M)H_4(\nu) + \frac{1}{72}\kappa_3(M)^2 H_6(\nu), \end{aligned} \tag{2.29}$$

where $H_n(\nu)$ are the Hermite polynomials, defined as $H_n(\nu) = (-1)^n e^{\nu^2/2}\frac{d^n}{d\nu^n}e^{-\nu^2/2}$.

As noted in LoVerde and Smith [62], the reduced cumulants $\kappa_n(M)$ can be calculated either through Monte Carlo methods or through analytic integration. Both methods tend be slow and difficult. In LoVerde and Smith [62] this is solved through the use of fitting functions. These functions were found to be insensitive to changes in cosmology and varied slowly with mass: for example the reduced cumulant κ_3 is described by the following fit:

$$\kappa_3(M) \approx f_{NL}(6.6 \times 10^{-4})\left[1 - 0.016\ln\left(\frac{M}{h^{-1}M_\odot}\right)\right]. \tag{2.30}$$

The cumulant κ_4 was found to diverge with increasing simulation volume and thus the fitting function maintains an L dependence. For comparisons with simulations this length parameter can be defined in terms of the side length of the simulation volume. For comparisons with real data the "side length" of the observable universe may be approximated as $L \approx 2R_{\rm Hor}$ where $R_{\rm Hor}$ is the comoving causal horizon, found by integrating Equation 1.22 to $z = \infty$, where $R_{\rm Hor} \approx 14000$ Mpc today. This fit can then be described as

$$\kappa_4(M) \approx f_{NL}^2 \left[(6.9 \times 10^{-7}) \left(1 - 0.021 \ln \left(\frac{M}{h^{-1} M_\odot} \right) \right) + 48 \Delta_\Phi^2(k_0) \ln \left(\frac{L}{L_0} \right) \right], \tag{2.31}$$

where $L_0 = 1600 h^{-1}$ Mpc and $\Delta_\Phi^2(k_0) = \frac{9}{25} \Delta_\mathcal{R}^2(k_0) = \frac{9}{25} A_s$ as per Equations 1.37 and 1.38 and the definitions presented in Section 1.3. The scale-dependent divergence of κ_4 is somewhat concerning but this divergence is only logarithmic in nature.

With fitting functions for the required cumulants, Equations 2.22 and 2.23 can be expanded and calculated with the aim of forming the non-Gaussian to Gaussian PS mass function ratio. In LoVerde and Smith [62] the $F(M, z)$ term is expanded such that $F(M, z) = F_0(M, z) + F_1(M, z) + F_2(M, z)$, and these terms are given as

$$\begin{aligned} F_0(M, z) &= \frac{1}{2} \mathrm{erfc} \left(\frac{\nu_c}{\sqrt{2}} \right) \\ F_1(M, z) &= \frac{1}{(2\pi)^{1/2}} e^{-\nu_c^2/2} \left(\frac{\kappa_3(M)}{6} H_2(\nu_c) \right) \\ F_2(M, z) &= \frac{1}{(2\pi)^{1/2}} e^{-\nu_c^2/2} \left(\frac{\kappa_4(M)}{24} H_3(\nu_c) + \frac{\kappa_3(M)^2}{72} H_5(\nu_c) \right) \end{aligned} \tag{2.32}$$

where the mass and redshift dependence of ν_c have been suppressed for clarity. Corresponding expressions for the derivatives $F_0'(M, z)$, $F_1'(M, z)$ and $F_2'(M, z)$ are given in LoVerde and Smith [62]. The series may then be expanded and truncated in $\ln(F(M, z))$; this is presented in LoVerde and Smith [62] as

$$\ln(F(M, z)) \approx \ln F_0(M, z) + \frac{F_1(M, z)}{F_0(M, z)} + \frac{F_2(M, z)}{F_0(M, z)} - \frac{1}{2} \left(\frac{F_1(M, z)}{F_0(M, z)} \right)^2. \tag{2.33}$$

From this expansion LoVerde and Smith [62] obtain an expression for the mass function ratio:

$$\left.\frac{n_{NG}}{n_G}\right|_{\text{log-Edgeworth}} \approx \exp\left[\frac{F_1(M,z)}{F_0(M,z)} + \frac{F_2(M,z)}{F_0(M,z)} - \frac{1}{2}\left(\frac{F_1(M,z)}{F_0(M,z)}\right)^2\right] \tag{2.34}$$
$$\times\left(1 + \frac{F_1'(M,z)+F_2'(M,z)}{F_0'(M,z)} - \frac{F_1(M,z)F_1'(M,z)}{F_0(M,z)F_0'(M,z)} - \frac{F_1(M,z)+F_2(M,z)}{F_0(M,z)} + \frac{F_1(M,z)^2}{F_0(M,z)^2}\right).$$

This function, when combined with the Tinker mass function introduced in Section 2.3, yields what we will henceforth refer to as the LVS mass function:

$$n_{\text{LVS}} = \left[\left.\frac{n_{NG}}{n_G}\right|_{\text{log-Edgeworth}}\right] \times n_{\text{Tinker},G}, \tag{2.35}$$

where the non-Gaussianity is encapsulated in the multiplicative prefactor which depends upon mass, redshift and f_{NL}.

A final caveat regarding the the form of the non-Gaussian mass function presented in Equation 2.35 relates to the definition of halo mass. For the Gaussian, Tinker mass function this quantity is well-defined and calibrated to simulations. In analytic approaches, such as the Press-Schechter method, the definition of the halo mass is less clear and can depend upon factors such as the background cosmology and the geometry of the halo [88, 89, 90, 91].

For example, in an Einstein-de Sitter model ($\Omega_m = 1$) the overdensity, relative to the *critical* density ρ_c, at virialization may be expressed as $\Delta_c = 18\pi^2 \simeq 178$ [92, 93, 94]. In Robertson et al. [89] a fitting function is provided which calculates this overdensity for ΛCDM cosmologies. When applied, this function predicts an overdensity, relative to the mean density, of $\Delta \simeq 380$ for $\Omega_m = 0.25$. However, as shown in Robertson et al. [89], the PS mass function is not well-fit by N-body simulations, regardless of the halo mass definition. As such, it is somewhat unclear as to which mass definition is optimal for the PS-based non-Gaussian mass function. In this work we have adopted the convention of defining the halo mass in terms of the spherical overdensity centered at the cluster position whose radius is defined such that the average density in the sphere is 200 times that of the background (M_{200}). This convention, which is consistent with that defined in Tinker et al. [76], will be used to define the halo mass for the LVS non-Gaussian mass function. Since the aim of our analysis will be to constrain deviations from $f_{NL} = 0$ (where the LVS mass function reduces to the Gaussian, Tinker mass function) this choice of halo mass definition should not significantly affect the constraint of such deviations.

2.4.2 Paranjape, Gordon, and Hotchkiss (PGH) Mass Function

Another proposed method for including non-Gaussianity in the halo mass function is presented in Paranjape et al. [95] and will hereafter be referred to as the PGH method and mass function. Rather than performing the expansion and truncation shown in Equations 2.23 and 2.28, they instead attempt to find a closed form for the infinite sum of terms in the expansion. Similar to the LVS method, the Edgeworth expansion (presented in Equation 2.24) is utilized to construct the non-Gaussian PDF:

$$f_{\rm NG} = \sqrt{\frac{2}{\pi}}\nu \exp\left[\sum_{n=3}^{\infty} \frac{(-1)^n}{n!}\kappa_n \frac{d^n}{dx^n}\right] e^{-\frac{\nu^2}{2}}, \tag{2.36}$$

such that the non-Gaussian mass function may be constructed per Equation 2.6.

Two key assumptions are made. The first is that the cumulants κ_n are approximately constant in mass within the regime of interest. This assumption conflicts slightly with the logarithmic growth found in the fitting functions presented in Equations 2.30 and 2.31. The second key assumption is that the cumulants are perturbatively ordered such that $\kappa_n \sim (f_{NL}\sqrt{A_s})^{n-2}$, where A_s refers to the primordial amplitude parameter as defined in Section 1.3; this assumption is supported by Equations 2.30 and 2.31. The purpose of these assumptions is to create a non-Gaussian mass function tailored specifically to the high mass and high f_{NL} regime of interest to cluster studies [96, 23, 24, 97, 98, 84].

Through the assumption of an exact perturbative series of cumulants, such that $\kappa_n \equiv (f_{NL}\sqrt{A_s})^{n-2}$ (where $n \geq 3$), the first term in the series may be recast as $\kappa \equiv \kappa_3$ and a closed form solution to Equation 2.36 is presented in Paranjape et al. [95] as

$$f_{\mathrm{NG}}(\kappa, \nu_c) = \sqrt{\frac{2}{\pi}}\nu_c(1+\kappa\nu_c)^{-1/2}\exp\left[\frac{1}{\kappa^2}(\kappa\nu_c - (1+\kappa\nu_c)\ln(1+\kappa\nu_c))\right] \quad (2.37)$$

where, as in the LVS formulation, we have again defined $\nu_c = \delta_c/\sigma_M(z)$ and, in the limit of f_{NL} approaching zero, the Gaussian PS form is recovered:

$$\lim_{\kappa\to 0} f_{\mathrm{NG}}(\kappa, \nu_c) = \sqrt{\frac{2}{\pi}}\nu_c e^{-\nu_c^2/2} \equiv f_{PS}(\nu_c). \quad (2.38)$$

Since the PS mass function is known to not compare well with simulations, the non-Gaussian mass function is again defined in terms of the ratio of the non-Gaussian to

Gaussian PS mass function such that

$$n_{\rm PGH} = \left[\frac{n_{NG}}{n_G} \bigg|_{\rm PGH} \right] \times n_{{\rm Tinker},G}, \tag{2.39}$$

where this ratio is defined in Paranjape et al. [95] as

$$\frac{n_{NG}}{n_G} \bigg|_{\rm PGH} = (1+\kappa\nu_c)^{-1/2} \exp\left[\frac{1}{2}\nu_c^2 + \frac{1}{\kappa^2}(\kappa\nu_c - (1+\kappa\nu_c)\ln(1+\kappa\nu_c)) \right]. \tag{2.40}$$

The PGH non-Gaussian mass function has the advantage that it has been designed specifically to be applicable and stable in the high mass, high f_{NL} regime. Its derivation, however, requires a pair of assumptions concerning the mass dependence and relative ordering of the higher order cumulants and, more importantly, only holds provided $f_{NL} > 0$. This final limitation is particularly challenging as it limits the f_{NL} parameter space and permits only a positive skew for the non-Gaussian spectrum. This impediment was resolved in Paranjape et al. [95] through comparisons with other non-Gaussian mass function formulations (specifically LoVerde et al. [61]) and postulating the following *ad hoc* equivalence:

$$\frac{n_{NG}}{n_G} \bigg|_{\rm PGH} (M, z, -f_{NL}) \equiv \left[\frac{n_{NG}}{n_G} \bigg|_{\rm PGH} (M, z, f_{NL}) \right]^{-1} \tag{2.41}$$

such that the PGH non-Gaussian mass function may be calculated for both positive and negative input values of f_{NL}, as will be shown later in this section.

Since it is known already from the LVS method that the assumed mass independence and perturbative scaling of the reduced cumulants required by the PGH method are not entirely valid, the PGH mass function should not be relied upon at high precision in f_{NL}. However, this should still permit the formulation of constraints for deviations from $f_{NL} = 0$.

2.4.3 Dalal et al. (DHS) Mass Function

The third formulation of the non-Gaussian mass function differs significantly from the first two and mirrors more closely the simulation-based approach adopted by recent Gaussian mass functions [76]. In this technique, as documented in Dalal et al. [58], the non-Gaussian mass function is derived empirically from a suite of N-body simulations, in a manner very similar to that which describes the Tinker mass function derivation. The technique employed in Dalal et al. [58], referred to hereafter as the DHS method and mass function, involves generating large N-body simulations of cosmic structure, first from a Gaussian primordial potential and then subsequently from the local form of non-Gaussian potential described in Equation 1.70, such that f_{NL} can be varied between simulations. For each Gaussian realization ($f_{NL} = 0$) a series of non-Gaussian realizations with matching Fourier phases are also created ($f_{NL} \neq 0$). Unlike in the Gaussian case, the non-Gaussian potential elicits mode-mixing amongst the Fourier modes of the perturbations. As the simulations are limited by both a finite box size and resolution scale they cannot account for any mixing of power originating from modes beyond these scales. This effect is mentioned in Dalal et al. [58] where it was shown to not significantly alter the behaviour of the simulations.

For positive values of f_{NL} the evolution of overdense regions is accelerated, resulting in an overall increase in the abundance of massive collapsed structures at late times. For negative f_{NL} an opposite effect was observed whereby the evolution of overdense regions was slowed, resulting in an overall decrease in the abundance of massive halos. Since the simulations started from effectively the same seed perturbations, it is possible to "match" the resulting halos from the Gaussian and non-Gaussian simulations and, through this process, quantify the effect that altering f_{NL} has on the distribution of massive halos in the universe. This process is described in detail in Dalal et al. [58] but effectively amounts to mapping which halos "own" which particles across simulations. In this fashion, halos of a similar mass may be stacked to derive a probability distribution which describes the relationship between a halo's original (Gaussian) mass M_0 and its modified (non-Gaussian) mass M_f in terms of the non-Gaussianity parameter.

This inter-simulation mapping implies that the effect of non-Gaussianity on the abundance of cosmic structure can be modeled as a mass shift from some fiducial, Gaussian mass. This allows for a redefinition of the non-Gaussian mass function as a convolution of a well-calibrated Gaussian mass function (Tinker for example) and a probability distribution which governs these shifts in mass. The non-Gaussian mass function, expressed in terms of the original and shifted masses, is presented in Dalal et al. [58] as

$$\frac{dn}{dM_f} = \int dM_0 \frac{dn}{dM_0} \frac{dP}{dM_f}(M_0), \tag{2.42}$$

where dP/dM_f is the mass-dependent probability distribution which maps the initial, Gaussian mass M_0 to the final, non-Gaussian mass M_f. In Dalal et al. [58] this probability distribution takes the form of a Gaussian PDF whose mean and variance have been fitted to simulation results and are given as

$$\left\langle \frac{M_f}{M_0} \right\rangle - 1 = 1.3 \times 10^{-4} (f_{NL}\sigma_8)\sigma_{M_0}(z)^{-2} \tag{2.43}$$

$$\left\langle \left(\frac{M_f}{M_0}\right)^2 \right\rangle - \left\langle \frac{M_f}{M_0} \right\rangle^2 = 1.4 \times 10^{-4} (|f_{NL}|\sigma_8)^{0.8}\sigma_{M_0}(z)^{-1}. \tag{2.44}$$

A comparison between the non-Gaussian mass function ratios predicted by all three techniques is presented in Figure 2–3.

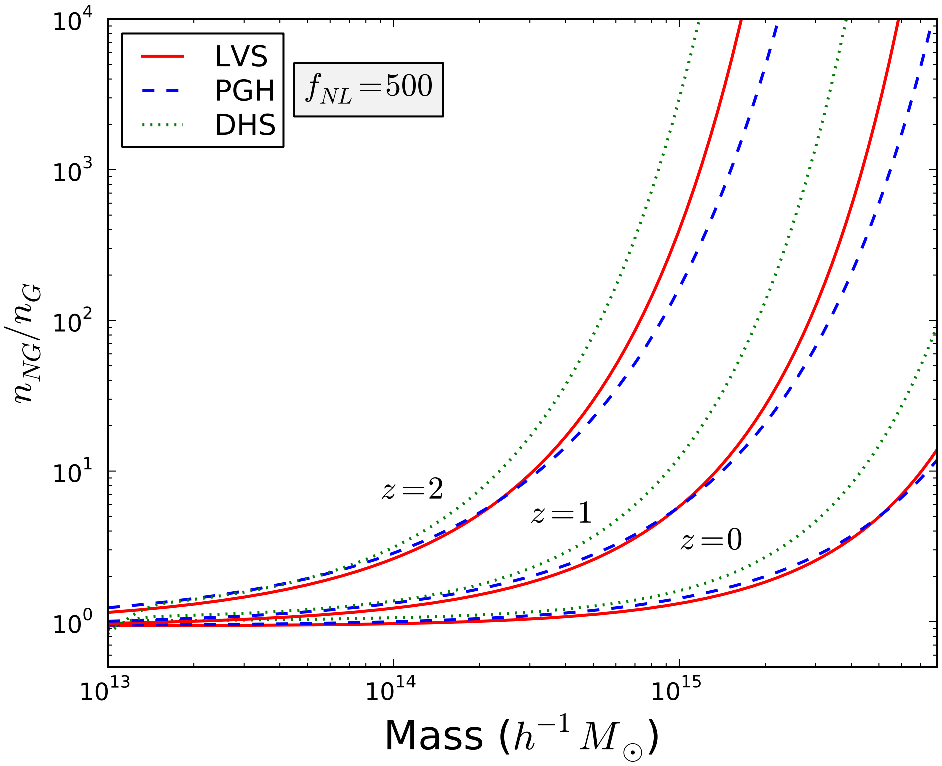

Figure 2–3: Non-Gaussian mass function ratios for $f_{NL} = 500$. The full non-Gaussian mass function is obtained through the product of these ratios and the Gaussian mass function, as per Equation 2.21.

One complication of this formulation lies in the mass definition utilized in its derivation. In Dalal et al. [58] the mass of a cluster is defined in terms of the FOF definition, rather than SO convention used in this work, with a linking length defined as $b = 0.2$. The relationship between these two mass definitions is explored in Tinker et al. [76] where it is found that, for a $\Delta = 200$ spherical overdensity and an $b = 0.2$ FOF linking length, the fractional relationship between the two masses is near unity, albeit with scatter. For the analysis performed in this work we will assume these masses to be equivalent.

The relationship between FOF and SO halo masses is explored more thoroughly in More et al. [78] where they fit a relation between the two mass definitions which is dependent upon the halo concentration and thus also its mass and redshift as well as the cosmology. With this relation, it is possible to obtain a broad estimate for the error associated with equating the FOF $b = 0.2$ halo mass definition with the $\Delta = 200$ SO definition.

To do so, we utilize the fitting function provided in Duffy et al. [99] to calculate the concentration of a halo of a given mass (for $\Delta = 200$) and redshift, assuming an NFW [100] cluster density profile. With this concentration, the fitting function in More et al. [78] may be utilized to calculate the spherical overdensity which best corresponds to the FOF $b = 0.2$ halo mass definition. From this new value for the spherical overdensity we may employ the technique presented in Hu and Kravtsov [93] to re-calculate the mass of the halo (again assuming an NFW profile) and compare it with the original $\Delta = 200$ mass. When we perform this test across the mass and redshift range relevant to our analysis ($M \sim 5 \times 10^{14} h^{-1} M_{\odot}$, $z \sim 0.6$) we find that the FOF $b = 0.2$ and $\Delta = 200$ SO halo mass definitions differ by $\lesssim 15\%$.

In the Dalal non-Gaussian mass formulation, the effect of this uncertainty in halo mass is a modification of the mean and variance of the convolution kernel, as described in Equations 2.42, 2.43, and 2.44. From these equations, we find that the mean and variance are functions of $\sigma(M)^{-2}$ and $\sigma(M)^{-1}$ respectively. However, for typical cluster masses ($M \sim 5 \times 10^{14} h^{-1} M_{\odot}$) we find that $\sigma(M) \propto M^{-0.25}$, implying associated uncertainties in the mean and variance of $< 10\%$. Thus, we do not expect this uncertainty in halo mass to be a significant source of uncertainty for the DHS non-Gaussian mass function.

There exist many advantages to the DHS non-Gaussian mass function formulation; among them is the relative simplicity of the calculation. This approach relies primarily upon the calculation of a mass, redshift and f_{NL}-dependent probability distribution. However, the empirical fit which facilitates this calculation has limitations. Among these is the number of simulations with which an empirical relation may be calibrated. In Dalal et al. [58], it is stated that several simulations were run for both the Gaussian and non-Gaussian starting positions for various f_{NL}. However, it may also be useful to test the fit against different cosmologies and for different halo mass definitions.

Within the simulations which were performed, the Gaussian PDF, defined through Equations 2.43 and 2.44, is claimed to achieve a level of precision of near 10% [58]. As stated above, this uncertainty is likely to be comparable to that imposed by converting from the FOF to the SO halo definition. This simulation-calibrated mass function is compared with those derived via analytical methods in Figure 2–3. In this figure we find some indication of inherent uncertainties associated with the non-Gaussian mass functions as, when evaluated with the same mass definition, the PS-based LVS and PGH non-Gaussian mass functions show some disagreement across the given mass range. The agreement between these mass functions is explored further in Chapter 7.

CHAPTER 3
Galaxy Clusters

3.1 Overview

Galaxy clusters are gravitationally-bound collections of galaxies and are the largest gravitationally-collapsed objects in the universe. Their abundance as a function of mass and redshift is dependent upon the growth of structure over cosmic time and can be described through the halo mass function definitions introduced in Chapter 2. The abundance and evolution of galaxy clusters depends sensitively upon cosmology.

In this chapter we will provide a general astrophysical description of galaxy clusters, discussing their physical properties as well as modes of detection and completed surveys. The Sunyaev-Zel'dovich (SZ) effect will be introduced as an important cluster observable and its relevance to galaxy clusters surveys will be explored.

We will also discuss the South Pole Telescope and its efforts in observing galaxy clusters via their SZ signatures. The methods for extracting galaxy clusters from survey maps will be discussed, focusing in particular upon galaxy clusters imaged via the SZ effect. Finally, recent cluster catalogs will be presented, providing the basis for the cosmological analysis presented in later chapters.

3.2 Optical and X-ray Properties

Halos are dominated by their dark matter component, possessing a baryon fraction similar to the cosmic mean ($\Omega_b/\Omega_m \sim 0.15$) [101, 102, 11]. The bulk of these baryons ($\sim 90\%$) do not lie within the member cluster galaxies but rather are dispersed within the halo, constituting the intra-cluster medium (ICM) [103, 104]. This ICM is a rarefied, hot plasma with typical temperatures of a few 10^7 K and particle densities of approximately 10^{-1} to 10^{-4} cm^{-3} [105, 106]. High energy emission from this plasma, in the form of thermal bremsstrahlung, correlates strongly with halo mass and has allowed for X-ray-based galaxy cluster surveys [107, 108, 109].

The remaining luminous baryons rest in the member cluster galaxies, bound in the gravitational well of the host halo. Properties of these cluster galaxies can also be shown to correlate to varying degrees with the host halo mass and may be observed at optical wavelengths. Examples include the velocity distribution of the the cluster galaxies (dispersion velocities), their abundance within some radius (optical richness), cluster galaxy luminosities, the luminosity of the brightest cluster galaxy (BCG) and others [110]. Optical cluster surveys have a long history, including early work by Abell [111] and Zwicky et al. [112]. Examples of more recent surveys, and their resulting cosmological constraints, include the Red-Sequence Cluster Survey (RCS) [113, 114] and the MaxBCG catalog [115] from the Sloan Digital Sky Survey (SDSS) [116].

X-ray galaxy cluster surveys detect clusters via the X-ray emission from the ICM. From an assumption of simple hydrostatic equilibrium for the intra-cluster gas present within the cluster's gravitational potential, the electron temperature T_e is approximated in Birkinshaw [117] as

$$
\begin{aligned}
k_B T_e &\approx \frac{G M m_p}{2 R_{\text{eff}}} && (3.1) \\
&\approx 7 (M / 3 \times 10^{14} M_\odot)(R_{\text{eff}}/\text{Mpc})^{-1}\ \text{keV}, && (3.2)
\end{aligned}
$$

where k_B is the Boltzmann constant and $M \sim 3 \times 10^{14} M_\odot$ and $R_{\text{eff}} \sim 1$ Mpc are typical masses and radii. For X-ray cluster surveys, the primary cluster observables consist of X-ray flux, temperature, and the constructed cluster mass proxy Y_X [118, 108]. Verification of candidate X-ray sources can be accomplished by resolving the spatial profile of the candidate, studying its spectral properties or through follow-up observations at other frequencies [106]. Numerous X-ray cluster surveys have been performed in recent years, from which informative cosmological constraints have been obtained [119, 120, 121, 122, 108, 109].

3.3 The Sunyaev Zel'dovich Effect

The Sunyaev-Zel'dovich (SZ) effect permits a method by which galaxy clusters may be observed through their interaction with the Cosmic Microwave Background (CMB) [123, 124]. The thermal SZ effect is characterized by the slight spectral distortion of the CMB caused by the inverse Compton scattering of cold CMB photons by hot intra-cluster electrons. This scattering results in an average increase in the scattered CMB photon's energy by an amount roughly equal to $k_B T_e / m_e c^2$, where k_B is the Boltzmann constant and T_e, m_e refer to the electron temperature and mass respectively [117, 125].

This distribution of hot intra-cluster electrons serves to modify the spectrum of the CMB radiation passing through it. Massive galaxy clusters are optically thin at microwave frequencies; there is only a percent-level probability of a CMB photon scattering as it passes through the cluster [125]. This effect provides a frequency-dependent modification to the underlying CMB spectrum with an amplitude proportional to the Compton y-parameter, defined as

$$y = \int n_e \frac{k_B T_e}{m_c c^2} \sigma_T d\ell, \tag{3.3}$$

where $\sigma_T \simeq 6.6524 \times 10^{-25}$ cm^2 is the Thomson cross-section and the integral is performed along the line of sight through the cluster.

In general, the intensity change caused by the thermal SZ effect can be difficult to calculate, particularly when considering multiple scatterings and relativistic corrections [117, 126, 127, 128]. However, in the non-relativistic limit, the scattering process may be recast in terms of the Kompaneets equation, which describes a change in occupancy number, $n_\gamma(\nu)$, due to a diffusion process [129]:

$$\frac{\partial n_\gamma}{\partial y} = \frac{1}{x_e^2} \frac{\partial}{\partial x_e} x_e^4 \left(\frac{\partial n_\gamma}{\partial x_e} + n_\gamma + n_\gamma^2 \right), \tag{3.4}$$

where $x_e = h\nu/k_B T_e$ and y is the Compton parameter as defined above. Since, even for large galaxy clusters, the Compton parameter remains quite small ($y \sim 10^{-4}$) and electrons are largely non-relativistic ($T_e \sim 7$ keV) the Kompaneets equation can be used to obtain an analytic form for the spectral change caused by the scattering [117]:

$$\Delta I(x) = x^3 \Delta n_\gamma(x) I_0, \tag{3.5}$$

where $x \equiv \frac{h\nu}{k_B T_{CMB}}$ is a dimensionless frequency parameter and

$$\Delta n_\gamma = xy \frac{e^x}{(e^x - 1)^2} \left(x \frac{e^x + 1}{e^x - 1} - 4 \right) \tag{3.6}$$

with $I_0 = 2(k_B T_{CMB})^3/(hc)^2$. By combining Equations 3.5 and 3.6 we can express the change in intensity as follows:

$$\Delta I(x) = x^4 \frac{e^x}{(e^x - 1)^2} \left(x \frac{e^x + 1}{e^x - 1} - 4 \right) I_0 y; \tag{3.7}$$

this spectral distortion to the intensity is presented in Figure 3–1.

Further examination of Equation 3.7 reveals a few interesting features. The first is that the change in intensity due to the tSZ effect is independent of redshift. This attribute renders a cluster's SZ signature a rather unique observable and will have important implications when analyzing SZ surveys. The second feature is that the amplitude of the intensity change scales with the Compton y parameter. This simplified scaling is true only in the non-relativistic approximation and more thorough calculations show a more complicated dependence on both the optical depth τ_e and temperature T_e of the intra-cluster electrons [117, 126]. It is possible to solve Equation 3.7 for $\Delta I(x) = 0$ and locate the SZ 'null' at $x_0 \simeq 3.83$ or $\nu_0 \simeq 218$ GHz. This implies that, independent of y or T_e, the amplitude of the spectral distortion will go to zero at $\nu \simeq 218$ GHz; this 'null' is presented as a vertical dotted line in Figure 3–1.

If the scattering medium which induces the thermal SZ effect is moving along the line of sight, relative to the CMB rest frame, then there exists a second component to the SZ effect [124]. This effect modifies the radiation temperature of the CMB as

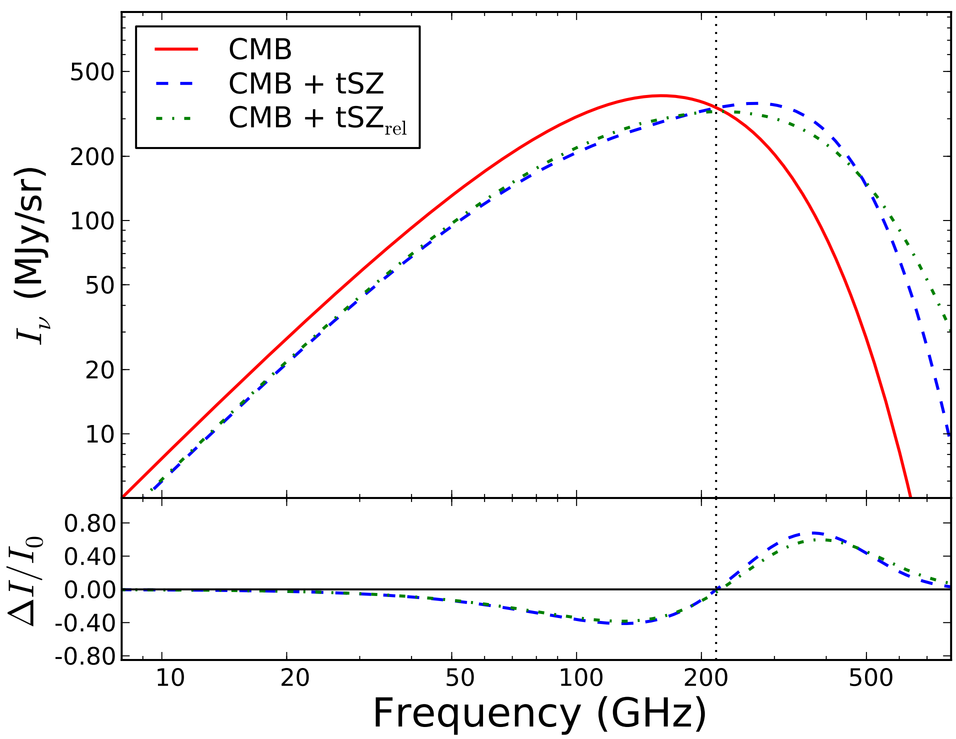

Figure 3–1: The undistorted CMB blackbody spectrum and the modification due to the spectral distortion of the tSZ effect. In this example, the cluster in question has an exaggerated Compton parameter that is 1000 times larger than normal. Relativistic corrections to the tSZ effect are presented for an electron temperature of $k_B T_e = 10$ keV. Also shown are the relative changes in intensity and the tSZ "null" at 218 GHz.

follows [124, 117]:

$$\frac{\Delta T}{T_{CMB}} \approx -\tau_e \frac{v_{\shortparallel}}{c}, \tag{3.8}$$

where $v_{\shortparallel}$ indicates a line of sight velocity. The spectral distortion to the intensity can be approximated assuming single scatterings and non-relativistic velocities such that [117]

$$\Delta I = -\tau_e \left(\frac{v_{\shortparallel}}{c}\right) I_0 \frac{x^4 e^x}{(e^x - 1)^2}. \tag{3.9}$$

There are two factors of note in Equation 3.9. The first is that the amplitude of the kSZ effect is expected to be suppressed when compared with the thermal effect. The magnitude of this suppression can be estimated roughly as $\frac{\Delta T_{kSZ}}{\Delta T_{tSZ}} \propto \left(\frac{v_{\shortparallel}}{c}\right)\left(\frac{k_B T_e}{m_e c^2}\right)^{-1}$ which corresponds to approximately an order of magnitude for reasonable cluster parameters. The frequency dependence of the kSZ effect is quite different from that of the tSZ, most notably lacking the tSZ null at 218 GHz. Although this implies that the two spectra may be separable near the tSZ null, the presence of relativistic effects provides percent-level corrections to both effects and precludes such a straightforward separation [130, 117]. These spectra are presented in Figure 3–2.

The SZ effect offers a unique approach to galaxy cluster surveys. It utilizes the CMB as a sort of "backlight" where, through the interaction of the CMB photons with the intra-cluster electrons, the cluster may appear either as a "hole" in the CMB (at frequencies below 218 GHz) or as a positive signal (at frequencies above 218 GHz). Perhaps the most promising and unique property of this cluster observable is that, for a given electron distribution, it is independent of redshift, thus facilitating the observation of high-redshift galaxy clusters.

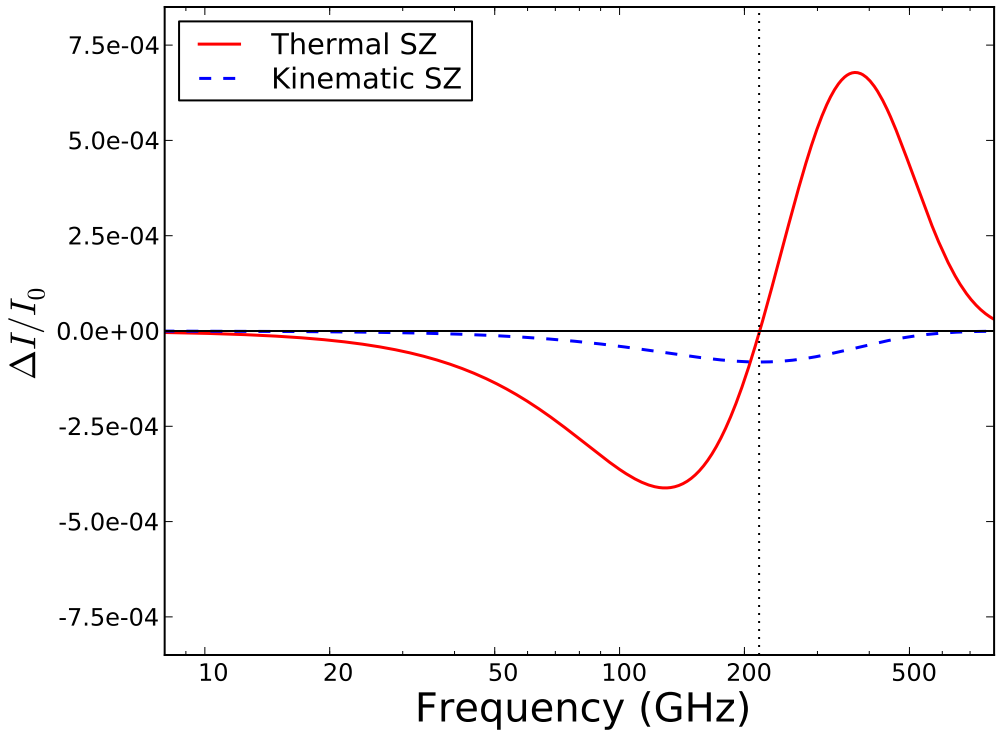

Figure 3–2: The spectral distortion caused by both the thermal and kinematic SZ effect, expressed in terms of the relative intensity. The cluster properties used for the calculation are $y = 1 \times 10^{-4}$, $\tau_e = 0.01$, and $v = 500$ km/s.

3.4 South Pole Telescope

The South Pole Telescope (SPT) is a 10-meter off-axis telescope, located at the South Pole and designed to observe galaxy clusters through their SZ signatures via observations with arcminute resolution of the microwave sky [131, 132, 133, 83]. The SPT imaging system consists of a 960-element array of superconducting transition edge sensor bolometers, designed with band-pass filters to observe at three frequencies: 95, 150, and 225 GHz [131, 132]. As seen in Figures 3–1 and 3–2, the latter of these frequencies correspond roughly to the null in the tSZ effect and the peak in the spectral decrement. In conjunction with the high altitude (2800 m) and low atmospheric moisture at the South Pole (median precipitable water vapour of 0.25 mm), these frequencies were also chosen to exploit atmospheric "windows" where absorption is low [131, 133]. The scan strategy of the SPT consists of rastering the sky via constant-elevation scans, which at the South Pole correspond to scans in constant declination. With the ability to scan at nearly a degree of azimuth per second, even with small steps in elevation the SPT is able to image fields of more than 100 square degrees in only a few hours (although achieving the desired "survey-depth" takes considerably longer) [133, 83].

In 2008, the SPT collaboration presented the first detection of previously unknown galaxy clusters via the SZ effect [133]. A small, 40 square degree region of sky was targeted and the four most significant galaxy cluster detections were presented. In 2010, a detection-significance-limited galaxy cluster catalog was presented from observations of nearly 200 square degrees of sky [83]. This presented not only the first statistically complete catalog of galaxy clusters detected via a non-targeted SZ survey but also provided the first cosmological constraints derived from such a sample. The underlying method and significance of these constraints will be detailed in Chapter 4.

3.5 Cluster Finding

In this section we will provide an overview of the cluster finding process, as employed by the SPT collaboration. The SZ cluster signal, as seen in Figure 3–2, is a small ($\Delta I/I_0 \sim 10^{-4}$) spectral distortion on a comparatively bright CMB background. This presents a clear challenge for detecting and extracting galaxy clusters from SZ maps. For this purpose, the SPT cluster finding process employed a method which utilized *spatially matched filters* [133, 83, 134, 135, 136, 137]. These filters are optimal for detecting objects with known morphologies.

The SPT collaboration applied the matched filter to SPT maps in the Fourier domain, creating filtered maps which optimize the signal-to-noise of the galaxy cluster sources. This matched filter is defined as

$$\Psi(k_x, k_y) = \frac{B(k_x, k_y)S(|\vec{k}|)}{B(k_x, k_y)^2 N_{astro}(|\vec{k}|) + N_{noise}(k_x, k_y)} \tag{3.10}$$

where B is the response of the SPT to signals on the sky and S is Fourier transform of the assumed galaxy cluster source template [83]. The SPT collaboration split the noise in this expression into two contributions: N_{astro} which includes astrophysical sources such as the primary CMB, the SZ background, and point sources and N_{noise} which includes the atmospheric and instrumental noise.

These "matched filters" require some form of prior knowledge concerning the spatial profile of galaxy clusters. It was demonstrated in Staniszewski et al. [133] that, for the SPT, the detection significance of galaxy clusters was relatively insensitive to the choice of profiles. Accordingly, in later works, such as Vanderlinde et al. [83], the source template was defined as

$$\Delta T = \Delta T_0 (1 + \theta^2/\theta_c^2)^{-1}, \tag{3.11}$$

where T_0 is the peak signal and θ_c is the core radius in angular units. In the cluster extraction process θ_c is varied to maximize the signal-to-noise for a given cluster [133, 83].

The final step in the cluster extraction process is to filter the maps at a series of θ_c scales, representing as many galaxy cluster sizes as possible, and subsequently to run a peak detection algorithm. For each cluster detection in the filtered maps, the filter scale which generates the largest signal-to-noise for that detection is chosen as the "true" filter scale for that cluster and this maximal signal-to-noise is denoted as ξ. In this fashion the matched filter maximizes the recovered signal-to-noise for each cluster as well as recovering the best-fit θ_c. This cluster extraction process was calibrated and tested extensively through the use of simulated cluster catalogs [83].

3.6 Cluster Catalogs

In this section we will present the two catalogs, as compiled by the SPT collaboration, which will form the basis of our cosmological analysis: a deeper catalog based upon 2008 data, and a wide-field catalog using the full 2500 square degree SPT survey.

In 2010, the first cosmological constraints derived from galaxy clusters detected via their SZ signatures were presented in Vanderlinde et al. [83], referred to hereafter as V10. The cluster catalog used for this analysis was derived from observations performed by the SPT during the 2008 observing season. Two similarly sized fields in the southern hemisphere were mapped through approximately 1500 hours of observation, resulting in a combined area of uniform depth totaling 196 square degrees which, after point sources were subtracted and bad pixels were masked, yielded 177.5 square degrees of map. The noise level in the fields was measured as 18μK-arcmin[1] at 150 GHz. The observation of the fields was performed at 150 and 225 GHz, while the cluster extraction was performed only for the 150 GHz data [83].

The V10 catalog was subjected to a straightforward selection cut, defined as a step function in both SZ significance and redshift space, with cutoffs at $\xi = 5.0$ and $z = 0.3$. The $\xi \geq 5.0$ cutoff was selected to mitigate the possibility of random noise fluctuations entering the sample. This selection cut is expected to yield approximately one false cluster candidate in the survey area [83]. In order to obtain redshifts, optical follow-up observations were performed for each cluster candidate, the details of which are presented in High et al. [138] and will be described further in Section 4.4. The resulting catalog consists of a statistically complete sample of 18 galaxy clusters, and is presented in Table 3–1.

The second cluster catalog to be used in this analysis is one which was derived by the SPT collaboration from wide-area observations designed to detect the most massive galaxy clusters. As a probe of the extreme end of the cluster mass function, this catalog will be employed in Chapter 7 as a test of non-Gaussianity. This catalog, as well as its selection methodology, is presented in Williamson et al. [84] and will be referred to hereafter as the W11 cluster catalog.

[1] i.e. a 1 square arcminute pixel would have an rms of 18μK

Table 3–1: The SPT V10 cluster cosmology catalog

Object Name	ξ	θ_c	Photo-z	Spec-z	σ_z
SPT CL J0509-5342	6.61	0.50	0.47	0.4626	-
SPT-CL J0511-5154	5.63	0.50	0.74	-	0.05
SPT-CL J0521-5104	5.45	1.00	0.72	-	0.05
SPT-CL J0528-5300	5.45	0.25	0.75	0.7648	-
SPT-CL J0533-5005	5.59	0.25	0.83	0.881	-
SPT-CL J0539-5744	5.12	0.25	0.77	-	0.05
SPT-CL J0546-5345	7.69	0.50	1.16	-	0.06
SPT-CL J0551-5709	6.13	1.00	0.41	0.4230	-
SPT-CL J0559-5249	9.28	1.00	0.66	0.6112	-
SPT-CL J2301-5546	5.19	0.50	0.78	-	0.05
SPT-CL J2331-5051	8.04	0.25	0.55	0.5707	-
SPT-CL J2332-5358	7.30	1.50	0.32	-	0.03
SPT-CL J2337-5942	14.94	0.25	0.77	0.7814	-
SPT-CL J2341-5119	9.65	0.75	1.03	0.9983	-
SPT-CL J2342-5411	6.18	0.50	1.08	-	0.06
SPT-CL J2355-5056	5.89	0.75	0.35	-	0.04
SPT-CL J2359-5009	6.35	1.25	0.76	-	0.05
SPT-CL J0000-5748	5.48	0.50	0.74	-	0.05

As with the V10 catalog, the W11 sample is a catalog of SZ-selected galaxy clusters, observed with the South Pole Telescope with redshifts obtained via optical follow-up observations. Once again the selection criteria for this catalog is based upon SZ-detection significance, parameterized via ξ, which again ensures that the sample is complete (by definition) above a given cutoff. For W11, an emphasis was placed upon maximizing the surveyed area and thus the amplitude of this noise map is somewhat higher than in V10, measured as 54μK-arcmin at 150 GHz for W11 versus 18μK-arcmin for the V10 sample [84]. The W11 cluster extraction procedure also included data from observations performed at both 150 and 95 GHz, unlike the V10 catalog.

The selection functions provided for the W11 sample are also similar to those employed in V10, defined again as step functions in both significance and redshift space such that $\xi \geq 7$ and $z \geq 0.3$. The final difference between these two catalogs lies in the surveyed area, with the V10 field spanning 177.5 square degrees whereas the W11 field area is quoted as 2532.4 square degrees, nearly 15 times larger. This increased survey area includes an overlap with the fields utilized for the V10 catalog and includes one cluster from the V10 sample, SPT-CL J2337-5942. However, this cluster falls below the W11 $\xi \geq 7$ selection cut and is thus not included in the sample utilized in our analysis. The resulting catalog (after applying the selection function) includes a total of 14 massive clusters and is presented in Table 3–2.

While only observed to a shallow depth, the W11 survey area represents the total area surveyed by the SPT. A recent catalog of clusters obtained from 720 square

Table 3–2: The SPT Wll cluster cosmology catalog

Object Name	ξ	Photo-z	Spec-z	σ_z
SPT-CL J0040-4407	10.27	0.40	-	0.070
SPT-CL J0102-4915[1]	18.62	0.78	-	0.089
SPT-CL J0243-4833	8.52	0.53	-	0.077
SPT-CL J0304-4401	7.94	0.52	-	0.076
SPT-CL J0417-4748	7.44	0.62	-	0.081
SPT-CL J0438-5419[2]	8.96	0.45	-	0.073
SPT-CL J0549-6204	12.62	0.32	-	0.066
SPT-CL J0555-6405	7.14	0.42	-	0.071
SPT-CL J0615-5746	11.21	1.0	-	0.10
SPT-CL J2031-4037[3]	9.50	-	0.342	-
SPT-CL J2106-5844	8.11	-	1.132	-
SPT-CL J2248-4431[4]	20.82	-	0.348	-
SPT-CL J2325-4111[5]	7.12	0.37	-	0.069
SPT-CL J2344-4243	12.13	0.62	-	0.081

[1] ACT-CL J0102-4915

[2] ACT-CL J0438-5419

[3] RXC J2031.8-4037

[4] ABELL S1063, RXC J2248.7-4431

[5] ABELL S1121

degrees of SPT observations at the V10 noise level was presented in Reichardt et al. [139] wherein 158 galaxy clusters are presented.

CHAPTER 4
Cluster Cosmology

4.1 Introduction

In this chapter we construct a formalism for comparing theoretical predictions of galaxy cluster abundances with observations. For this comparison, both the theoretical and observed cluster abundances will be expressed in terms of the same cluster properties. For the SPT SZ catalogs employed in this analysis, the physical observables correspond to the cluster's SZ significance ξ and its redshift z. For our analysis, we elect to transform the theoretical cluster abundances, defined in terms of the mass function, from their native mass space into the SZ significance space. For the observed cluster redshifts, follow-up observations must be made at other wavelengths, most notably optical, where redshifts may be acquired through spectral or photometric analysis; the details of such an analysis are presented in High et al. [138] and will be discussed in Section 4.4.

An important quantity for cluster surveys is known as the *selection function*, which describes the criteria upon which clusters are included in the sample. The selection function describes the purity of the sample, which quantifies the expected presence of false detections, and the completeness, which describes the potential for missed detections. The selection function for the survey will also depend upon which cluster observable is used. Great effort has therefore been put into using cluster observables with well-understood selection functions, for example the SZ-significance-based mass proxy ξ (used in V10 and W11), optical richness [115, 140], X-ray luminosity L_X or the constructed low-scatter X-ray proxy Y_X [141, 142, 108, 118]. The final step in this analysis is then to re-express the theoretical cluster abundances in terms of the cluster observable and then to compare theory with observation; this process will be described in detail in the following sections.

4.2 Calculating Cluster Likelihoods

In its simplest guise, cosmological analysis by way of cluster abundances is a counting experiment. Galaxy clusters are observed and their abundance is compared with what is expected from theory. The parameters of the cosmological model may be estimated from this comparison by way of a likelihood estimator for the observed dataset. The formulation of such an estimator depends, in general, upon the statistical properties of the given dataset. For binned datasets with few events per bin (which can be enforced by arbitrarily small bin sizes) the data follow Poisson rather than Gaussian statistics and the χ^2 statistic is not appropriate for parameter estimation [143, 144]. For such data, the Cash C statistic can be shown to form an appropriate likelihood estimator [143, 144]:

$$\mathcal{L} = \prod_{i=1}^{N} P_i = \prod_{i=1}^{N} \frac{x_i^{n_i} e^{-x_i}}{n_i!}, \tag{4.1}$$

where N is the number of bins in the space, x_i and n_i are the theoretically expected and observed counts for bin i respectively, and P_i is the Poisson probability in the i^{th} bin.

For the analysis performed in V10, the bin dimensions are defined by the cluster observable (the SZ-detection significance ξ) and the cluster redshift z. A two-dimensional grid can be created that spans the full observational range of both ξ and z. Enforcement of the low-count condition required by Equation 4.1 is met through requiring that every bin in the ξ-z space contains either zero or one clusters. This can be guaranteed through interpolating the finite grid of expected number counts to the exact location of the observed cluster in question, thus emulating the effect of an arbitrarily small bin size. This practice helps to illustrate one drawback of the Cash statistic (Equation 4.1), in that its explicit dependence upon bin size (expected counts in a bin) makes estimating the "goodness-of-fit" somewhat challenging. In practice, it is possible to estimate the goodness-of-fit for an observed catalog through comparisons with fit values generated from simulated catalogs.

Rather than directly calculating the likelihood presented in Equation 4.1, it is more convenient, even for limited catalogs, to calculate the log-likelihood. We define the log-likelihood as

$$\ln \mathcal{L} = \sum_{i=1}^{N} \left[n_i \ln(x_i) - x_i - \ln(n_i!) \right]. \tag{4.2}$$

If we make the explicit assumption that each bin contains only zero or one cluster(s) and thus $n_i = [0, 1]$ (depending on whether or not a cluster is observed) and recognize that $\sum_{i=1}^{N} x_i$ is simply the total of the expected number counts across the grid, which we will denote as x_{tot}, Equation 4.2 simplifies to

$$\ln \mathcal{L} = \sum_{i=1}^{N} \ln(x_i) - x_{tot}. \tag{4.3}$$

Thus the total log-likelihood reduces to simply calculating the log of the expected cluster number counts where clusters are observed and subtracting the total of the expected grid.

4.3 Scaling Relations

As described in the opening section of this chapter, formulating cosmological constraints from galaxy cluster abundances requires expressing the observed and theoretical cluster abundances in terms of the same cluster properties. For V10, this observable was the SZ-detection significance of the cluster, denoted ξ, as described in Section 3.5, and the cluster redshift z. To express the theoretical cluster abundances in terms of ξ, a scaling relation which defines ξ in terms of the mass function variables is required. The details of the cluster scaling relation formulated by the SPT collaboration are provided in V10, the results of which will be presented here.

The relationship between the SZ-significance ξ and the cluster mass is affected by both intrinsic and observational scatter as well as an empirically determined bias arising from the three free parameters with which the cluster-finding algorithm maximizes the signal-to-noise (map position in x and y and angular core size θ_c). Therefore, an unbiased SZ-detection significance, ζ, was introduced. This unbiased SZ-detection significance is equal to $\langle\xi\rangle$, the average detection significance over many noise realizations, when evaluated at the true cluster position and filter scale. Thus, the relationship between ζ and $\langle\xi\rangle$ describes the bias due to the cluster finder's freedom to maximize the detection significance by varying the position and filter scale of the cluster. These three degrees of freedom motivated the form of the relation between ζ and $\langle\xi\rangle$ which the SPT collaboration later calibrated on simulations. The results of this fit are presented in V10 as

$$\zeta \;=\; \begin{cases} \sqrt{\langle\xi\rangle^2 - 3} & \text{for } \zeta > 2 \\ \langle\xi\rangle & \text{for } \zeta \leq 2, \end{cases} \tag{4.4}$$

The unbiased significance was assumed to have a simple power-law dependence upon mass and redshift, with pivots chosen to reflect the survey's mass and redshift sensitivity. This scaling relation between mass, redshift, and unbiased significance is represented as

$$\zeta = A_{SZ}\left(\frac{M_{200}}{5\times 10^{14} M_{\odot} h^{-1}}\right)^{B_{SZ}} \left(\frac{1+z}{1.6}\right)^{C_{SZ}}, \tag{4.5}$$

where A_{SZ} represents the normalization of the mass-to-ζ scaling relation, B_{SZ} the slope in mass, and C_{SZ} the redshift evolution. The mass quantity M_{200} refers to the mass contained within a spherical region, centered at the halo position, with an average density of 200 times the mean density in the universe at that epoch, $\bar{\rho}_m(z)$.

The functional form of Equation 4.5 is physically motivated from self-similar scaling arguments based upon both the mass and redshift dependence of the observed SZ flux. The details of these arguments are presented in V10, where the SZ detection significance ζ is modeled as being sensitive to the central SZ decrement y_0 and the integrated SZ flux Y_{SZ}. The mass and redshift dependencies for these quantities are given as [83, 145, 146]

$$y_0 \propto M(1+z)^3 \tag{4.6}$$

and

$$Y_{SZ} \propto M^{5/3}(1+z)/D_A(z)^2. \tag{4.7}$$

The dependence of ζ upon mass and redshift is also expected to be affected by whether an individual cluster is resolved by the SPT beam ($\sim$1 arcminute FWHM at 150 GHz). As detailed in V10, if $\zeta \propto y_0$ then one would expect $B_{SZ} = 1$ and $C_{SZ} = 3$. If $\zeta \propto Y_{SZ}$ then, for unresolved sources, $D_A \propto (1+z)^{1.3}$ at $z \sim 0.6$ implying $B_{SZ} = 5/3$ and $C_{SZ} = -1.6$. For resolved sources, the significance depends upon the integrated noise, where in V10 it is shown that $\zeta \propto M^{4/3}(1+z)^2/D_A(z)$ if $\zeta \propto Y_{SZ}/N_{int}$ such that $B_{SZ} = 4/3$ and $C_{SZ} = 0.7$ at $z \sim 0.6$.

While the functional form of the scaling relation was motivated from self-similar arguments, the priors placed upon it were calibrated via simulations. As we will discuss below, these simulations were designed to include quantities specific to the SPT, including noise maps and beam profiles. These simulations also provided a means for evaluating the intrinsic scatter in ζ, which was found to follow a log-normal distribution and will be parameterized in the scaling relation as D_{SZ} [83].

The calibration of the scaling relation was accomplished by the SPT collaboration through a cluster-finding process on clusters with known masses in simulated SPT maps. This calibration utilized simulated SZ maps created through N-body simulations combined with a variety of gas models with the appropriate SPT noise maps superimposed (for both the V10 and W11 noise realizations) [147, 148, 149].

Table 4–1: Cluster scaling relation parameters

Scaling Relation Parameter	V10	W11
A_{SZ}	6.01 ± 1.80	3.51 ± 1.05
B_{SZ}	1.31 ± 0.26	1.30 ± 0.26
C_{SZ}	1.60 ± 0.80	0.85 ± 0.42
D_{SZ}	0.21 ± 0.04	0.16 ± 0.03

The best-fit values from these simulations were found for both the V10 and W11 catalogs and are presented in Table 4–1.

The discrepancies between the two scaling relations arise largely from the increased noise level in the shallower W11 cluster maps and the predicted differences in the reshift distribution of the more massive W11 clusters. Gaussian priors for the scaling relation parameters were motivated through testing of the scaling relation recovery when considering modified cluster gas models and pressure profiles [83]. The widths of these priors were defined to exceed the variations observed in the recovered scaling relation parameters and to reflect the uncertainty associated with the simulation-calibrated cluster scaling relation. The resulting priors were defined as Gaussians with 1σ uncertainties of 30%, 20%, 50%, and 20% about the best-fit points for the scaling relation parameters A_{SZ}, B_{SZ}, C_{SZ}, and D_{SZ} respectively for both the V10 and W11 cases. The best-fit values and 1σ priors are presented in Table 4–1.

4.4 Implementation

In this section we will describe, in detail, the process through which we calculate the likelihood for a catalog of galaxy clusters from an input set of cosmological and scaling relation parameters. The first step in this process involves computing the underlying halo mass function for the input cosmology. For this analysis we employ the Tinker mass function, presented in Section 2.3 in Equations 2.6 and 2.12. For the mass function calculation we must first compute the smoothed variance of the linear density field, $\sigma(M, z)$ (Equation 1.67), as a function of both mass and redshift. This requires calculating both the linear growth function $D(z)$ (Equation 1.61) and the matter power spectrum $P(k)$ (Equation 1.65). As described in Section 1.5, the CAMB software package provides an accurate and convenient method for calculating $P(k)$ and will be the method utilized in this analysis [54]. The calculation of $D(z)$ is performed through numerically solving the differential equation presented in Equation 1.61, for the cosmology in question.

The halo mass function yields the expected differential number counts of dark matter halos within a comoving volume for a given cosmology. However, the galaxy cluster data with which we wish to compare is expressed more easily in terms of sky area and redshift. By multiplying the expression for the differential number counts (Equation 2.12) by the comoving volume element (Equation 1.25) we are able to express the expected number of halos per mass, redshift and sky area interval as

$$\frac{dN}{dM d\Omega dz} = \frac{dV_c}{d\Omega dz} \frac{dn}{dM}. \tag{4.8}$$

This expression for the theoretically predicted halo abundances must then be translated into our observable parameter space. This requires the use of the cluster scaling relation (Equation 4.5) which translates the halo mass into the bias-free detection significance ζ. Additionally, we must take into account the scaling relation parameter which defines scatter in the mass-ζ relation, D_{SZ}. Computationally this is accomplished through first converting the mass function from mass to ζ-space, followed by a convolution of the resulting function with a log-normal Gaussian of width D_{SZ}.

The average detection significance $\langle\xi\rangle$ may then be calculated from the unbiased SZ-detection variable ζ, as described in Equation 4.4. Finally, the observable ξ is related to the average significance $\langle\xi\rangle$ through a Gaussian convolution of unit width, accounting for the observational uncertainty of the SZ-detection significance.

Through the processes described above, we are able to calculate the theoretically predicted abundances of galaxy clusters as a function of cosmology, SZ-detection significance, and redshift. This calculation is expressed as a surface in ξ and z with each $\xi - z$ coordinate pair corresponding to a predicted cluster abundance. An example of such a surface is presented in Figure 4–1, along with the result of summing over a threshold value in the ξ dimension.

The final step in the implementation of the cluster likelihood requires characterizing the selection function, in terms of both ξ and z, and subsequently computing the likelihood for an observed cluster sample given a cosmological model and scaling relation set. For the V10 and W11 analyses, the choice of ξ (the SZ-detection significance) as the cluster observable results in a simple and well-understood selection function. Since clusters are selected based upon detection significance, the selection function in that dimension is defined as a cut at the selection threshold: $\xi_{\text{cut}} = 5$ and $\xi_{\text{cut}} = 7$ for the V10 and W11 analyses respectively. The use of SZ-detection significance as the cluster observable guarantees that (by definition) all objects with

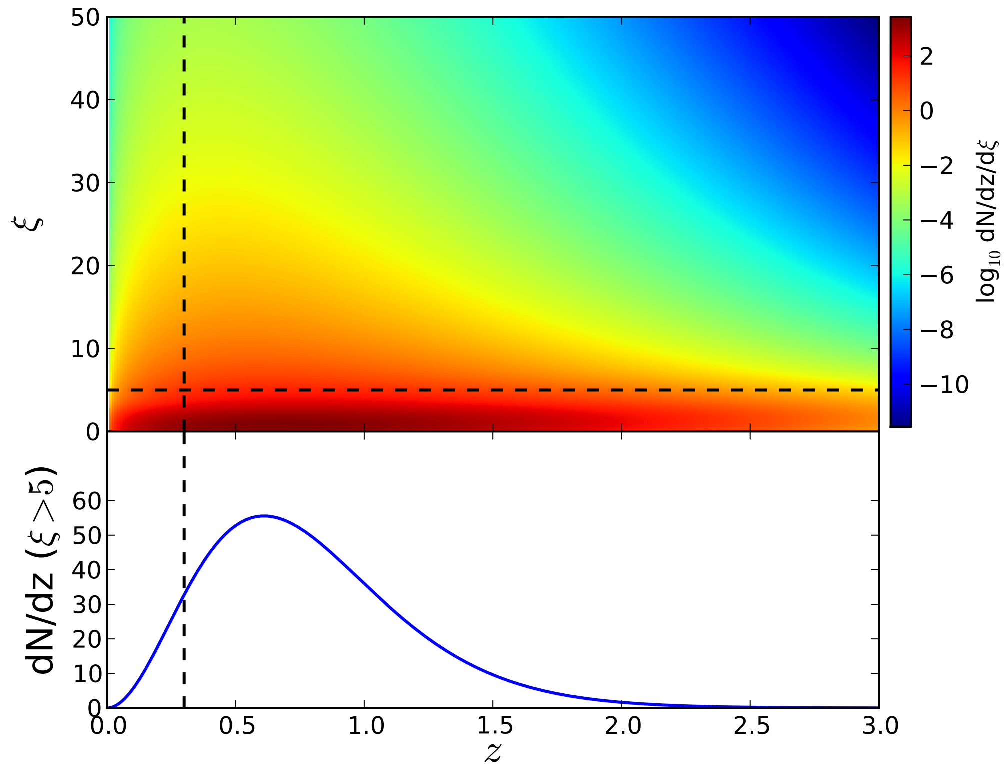

Figure 4–1: A grid of theoretically predicted cluster number counts as a function of ξ and z for the best-fit WMAP7 ΛCDM cosmology and fiducial mass-ζ scaling relation [18, 11]. Also shown is the selection function cut at $\xi = 5$ and $z = 0.3$ as well as the associated, integrated dN/dz curve. Survey area is defined to be the total surveyed area in V10, namely 177.5 square degrees.

an SPT SZ-significance greater than the threshold are included. This selection function is also independent of redshift and is straightforward to model in our theoretical predictions.

The selection function in the redshift dimension was motivated by the instrument response as well as the cluster-finding algorithm. In both analyses this selection function corresponded to a cut at redshift $z_{\mathrm{cut}} = 0.3$, which acts to conservatively exclude regions in redshift space where the cluster-finding algorithm has difficulty distinguishing the cluster signal from the primary CMB anisotropies. Thus, the selection function for each cluster catalog is characterized by the region of parameter space defined as $\xi > \xi_{\mathrm{cut}}$ and $z > 0.3$.

With a cosmology-dependent prediction for galaxy cluster abundances in the observational space defined by the cluster observable ξ, we are able to calculate the likelihood for an observed set of clusters within a survey volume. The details of this calculation are presented in Section 4.2 and are encapsulated in the final expression for the log-likelihood, presented in Equation 4.3. The implementation of this quantity requires: calculating the theoretically predicted abundances for all observed clusters in terms of their positions on the $\xi - z$ coordinate grid, accounting for observational uncertainties associated with the individual cluster redshifts, and integrating the total predicted cluster abundance within the survey volume.

First, we shall consider the uncertainties associated with the redshift estimates, as obtained by the SPT collaboration, for the galaxy clusters in the sample. The details concerning the acquisition and reduction of redshift data for the V10 and W11 samples are presented in Vanderlinde et al. [83], Williamson et al. [84], and High et al. [138]. For the V10 sample, there exists significant overlap with the Blanco Cosmology Survey (BCS [150]), a deep optical survey performed by the 4m Blanco telescope using g, r, i, and z filters [83, 138]. For V10 cluster candidates outside of the BCS region, as well as unconfirmed candidates, the twin 6.5m Magellan telescopes were used. Deeper images of each candidate were taken until detections of early-type galaxies were achieved and photometric redshifts could be obtained. The Magellan telescopes were also used to obtain spectroscopic redshifts for a subsample of the V10 catalog, where typical exposures times ranged from 20-60 minutes per candidate [83]. Clusters with only a photometric redshift were assigned an uncertainty associated with that redshift, σ_z, which was calculated through comparison between photometric and spectroscopic redshifts for clusters where both were measured. Clusters redshifts derived from spectroscopic analysis were assumed to be exact with no associated uncertainty. The magnitudes of the photometric uncertainties were found to be of order 3% in $(1 + z)$, where exact quantities are presented in Tables 3–1 and 3–2.

For the W11 catalog, redshifts for the previously-unknown candidates were obtained by the SPT collaboration using the 1m Swope telescope, the 4m Blanco telescope, the Very Large Telescope (VLT), and the Spitzer Space Telescope [84]. Spectroscopic redshifts were available for two of the previously-known clusters, as listed in Table 3–2, while new spectroscopic data for SPT-CL J2106-5844 was acquired with the VLT, as documented in Foley et al. [151]. The redshift uncertainties were derived using a method similar to that which was performed in V10 and included the use of the V10 clusters for calibration purposes. Photometric uncertainties were again found to be of order 3% in $(1+z)$ while spectroscopic redshifts were considered to be exact.

With these observational cluster redshift uncertainties we are able to calculate the first term in Equation 4.3; the sum of the expected abundances at the position of clusters. Although initially computed on a finite grid, we calculate the expected cluster abundance via an interpolation to the exact location of the observed cluster in $\xi - z$ space. We perform this interpolation in two steps. In the first step, we interpolate to the cluster location in ξ-space and extract, as a function of redshift, a vector of expected abundances. The redshift uncertainty associated with the cluster in question is taken into account through convolving this vector with a Gaussian of width σ_z. In the second step, we interpolate to the cluster's redshift value and find the expected abundance for that cluster. This same procedure is performed for all clusters in the analysis, excluding clusters with spectroscopic redshifts for which no convolution in redshift space is required.

Finally, we calculate the second term in Equation 4.3. This is achieved through integration of the expectation grid, taking into account the selection function in both ξ and z. The result of this integration is the total expected number of clusters, within the survey volume, for the cosmology, scaling relation, and selection function in question. Together, with the sum of the individual expected cluster abundances, this forms the total log-likelihood for the galaxy cluster analysis.

Testing of this cluster likelihood was achieved through the use of simulated cluster catalogs. Similar cluster catalogs were also employed in the calibration of the cluster scaling relation. For these tests, a number of simulated cluster catalogs, corresponding to multiple realizations of a known cosmology and scaling relation, were created. The cluster likelihood's recovered parameter fits were found to be consistent with the input parameter values and no significant biases were reported.

4.5 Markov Chain Monte Carlo

The cluster likelihood is sensitive to parameters which alter the expected abundances of galaxy clusters in the universe. These parameters can be broadly separated into two sets: cosmological parameters and the parameters which define the mass-observable cluster scaling relation. Cosmological parameters were introduced in Section 1.3, where the canonical ΛCDM cosmological model was described through six base parameters.

The parameters which comprise the mass-observable cluster scaling relation are described in Section 4.3 and defined through Equation 4.5. The combination of parameters defining both the input cosmology and scaling relation thus comprises a ten-parameter set which will provide the basis upon which constraints from the cluster likelihood will be made.

Described in general terms, we would like to explore the probability corresponding to a generalized set of model parameters ($\boldsymbol{\theta} = \theta_1, \theta_2, \cdots, \theta_d$) for an observed dataset, $\boldsymbol{D}$. This quantity, $P(\boldsymbol{\theta}|\boldsymbol{D})$, will be referred to as the *posterior* PDF of $\boldsymbol{\theta}$ and is the aim of the parameter estimation methodology. Introduced earlier was the likelihood $P(\boldsymbol{D}|\boldsymbol{\theta})$, which is a measure of the probability of the observed data given a particular set of model parameters. For the cluster likelihood, a method for calculating this expression was demonstrated in Section 4.2. The final quantity which we will introduce is the *prior* probability of the model parameters, $P(\boldsymbol{\theta})$, which encompasses any known constraints to the model space.

Through Bayes' theorem we can express the posterior PDF in terms of the likelihood and the prior as follows:

$$P(\boldsymbol{\theta}|\boldsymbol{D}) = \frac{P(\boldsymbol{D}|\boldsymbol{\theta})P(\boldsymbol{\theta})}{\int P(\boldsymbol{\theta})P(\boldsymbol{D}|\boldsymbol{\theta})d\boldsymbol{\theta}} \propto P(\boldsymbol{D}|\boldsymbol{\theta})P(\boldsymbol{\theta}). \tag{4.9}$$

For parameter estimation, the denominator in Equation 4.9 (which is independent of $\boldsymbol{\theta}$) may be ignored as parameter estimation is only concerned with relative likelihoods. Thus, Equation 4.9 states that (up to a normalization factor) the probability of the model given the data corresponds to the probability of the data given the model multiplied by any prior probability placed upon the model. For the cluster likelihood, the data corresponds to the cluster catalog while the model is characterized through the ten-dimensional space defined by the cosmology and scaling relation.

The primary difficulty in the approach shown in Equation 4.9 is that the computations required are prohibitive, especially in higher dimensional models. For instance, the posterior distribution for a single parameter θ_i requires an integral of the joint posterior distribution, *marginalizing* over all other model parameters:

$$P(\theta_i|\boldsymbol{D}) = \int\cdots\int P(\boldsymbol{\theta}|\boldsymbol{D})d\theta_1 d\theta_2\cdots d\theta_{i-1}d\theta_{i+1}\cdots d\theta_d. \tag{4.10}$$

From this expression, expectation values, such as the mean, may be calculated:

$$\langle\theta_i|\boldsymbol{D}\rangle = \int \theta_i P(\theta_i|\boldsymbol{D})d\theta_i. \tag{4.11}$$

For most models, analytic computation of Equation 4.10 is not possible and numerical means are required. One technique is to sample the posterior distribution in a grid whose dimensionality is defined by the number of model parameters. Calculating the cluster likelihood in such a fashion presents a clear challenge as even a sparse grid-like sampling of the ten-dimensional parameter space would scale as n^{10}, where n is the number of steps taken in any one dimension. For such a sampling, a fast method for calculating the likelihood is a necessity as, for a one second likelihood evaluation, calculating $\sim 10^{11}$ iterations would require thousands of years.

A more effective method of calculating Equation 4.10 is the Markov Chain Monte Carlo (MCMC) approach, whose use in scientific parameter estimation is well-documented [152, 153, 154, 155, 156]. The MCMC methodology is a way to calculate the posterior distribution for a set of model parameters given a sample dataset. Here we will briefly review this method; a much more thorough description can be found in Gilks et al. [157].

The MCMC effectively samples, or takes random draws, from the joint posterior distribution, moving from one point in parameter space to another, forming what is referred to as the "chain". The key to this approach is that rather than sampling the posterior in a regular grid, the Markov chain is designed such that its stationary or equilibrium distribution is representative of the joint posterior. With the MCMC approach the expectation values for model parameters can be expressed in terms of their density within the chain:

$$\langle \theta_i | \boldsymbol{D} \rangle \approx \frac{1}{N} \sum_{j=1}^{N} \theta_i^{(j)}, \tag{4.12}$$

where the summation is taken over chain steps and marginalization over the other model parameters is automatic.

A key component in the MCMC approach involves the construction of the Markov chain. One method for doing so is the Metropolis-Hastings alogrithm [158, 159]. This algorithm operates via a rejection sampling technique: a candidate step is accepted or rejected based upon a probability criterion. Starting from an initial position in parameter space ($\boldsymbol{\theta}_n$), a new candidate step ($\boldsymbol{\theta'}$) is generated from an assumed proposal distribution, $q(\boldsymbol{\theta'}|\boldsymbol{\theta}_n)$. The acceptance probability of this candidate step is expressed as the relative probability of the proposed step to the current one:

$$\alpha(\boldsymbol{\theta'}|\boldsymbol{\theta_n}) = \min\left\{1, \frac{P(\boldsymbol{D}|\boldsymbol{\theta'})P(\boldsymbol{\theta'})q(\boldsymbol{\theta}_n|\boldsymbol{\theta'})}{P(\boldsymbol{D}|\boldsymbol{\theta}_n)P(\boldsymbol{\theta}_n)q(\boldsymbol{\theta'}|\boldsymbol{\theta}_n)}\right\}, \tag{4.13}$$

where the denominator in Equation 4.9 cancels in this ratio. If $\alpha(\boldsymbol{\theta'}|\boldsymbol{\theta_n}) = 1$ (i.e., the new point is a better fit) then the new step is accepted and the MCMC continues. If $\alpha(\boldsymbol{\theta'}|\boldsymbol{\theta_n}) < 1$ then a uniform random variable in the interval $U \in (0, 1)$ is drawn and the acceptance/rejection criteria is expressed as

$$\begin{aligned}
&\text{If } U \leq \alpha(\boldsymbol{\theta'}|\boldsymbol{\theta_n}) \text{ then accept step and } \boldsymbol{\theta}_{n+1} = \boldsymbol{\theta'}\\
&\text{If } U > \alpha(\boldsymbol{\theta'}|\boldsymbol{\theta_n}) \text{ then reject step and } \boldsymbol{\theta}_{n+1} = \boldsymbol{\theta}_n.
\end{aligned}$$

The ratio of accepted to rejected steps is known as the *acceptance ratio* for the MCMC. As the chain approaches convergence, the distribution of points reproduces the joint posterior, allowing for estimates of any statistical quantity required.

There are, however, certain caveats to the technique. First, one must draw enough samples to ensure the stationarity and convergence of the Markov chain. This generally requires removing some initial portion of the chain (also known as *burn-in*), generating large numbers of samples, and employing convergence statistics.

Other concerns may relate to the selection of parameter step sizes and acceptance ratios where, for example, a chain stuck in a local minimum with a small step size may have a very high acceptance ratio or, alternatively, a chain with a large step size may have a very low acceptance ratio. In both cases the chains will be slow to explore the likelihood space, but in the limit of a large number of steps both chains will eventually converge. In cases such as these, it is possible to modify the proposal distribution as the likelihood surface is sampled, thus permitting a reasonable acceptance ratio and a more informed sampling of the space.

One example of a chain convergence test is the Gelman-Rubin "$\hat{R}-1$" statistic, which may be used when running multiple chains [160, 161]. This test forms a comparison between a parameter's variance within a chain and the variance of the mean of that parameter between chains. As the individual chains sample the space and each approach the stationary distribution this ratio will converge to a value of 1. While a small $\hat{R}-1$ value does not necessarily guarantee convergence it is a strong indicator, particularly when calculated across numerous parameters, and can be thought of as a necessary although not necessarily sufficient condition for convergence. In practice, chains are often run well past the point where $\hat{R} \simeq 1$ and convergence is not often a significant concern.

While the base implementation of an MCMC algorithm is fairly straightforward, optimizations ensuring reasonable acceptance ratios and rapid convergence can be complex. For the purposes of cosmological parameter estimation there exists an analysis package which implements the MCMC algorithm: Cosmological Monte

Carlo (CosmoMC)[1] [154]. The CosmoMC analysis package is an MCMC engine which is designed specifically for cosmological parameter analysis. Incorporated into CosmoMC is the CAMB package (referred to in Section 1.5) which generates theoretical predictions for both the matter power spectrum and the CMB anisotropy angular power spectra [54]. The CosmoMC engine is optimized to be computationally efficient while also employing the Gelman-Rubin convergence criterion described in this section. Other advantages to using CosmoMC lie in its ability to run multiple, simultaneous Markov chains, thus facilitating an efficient and thorough sampling of the posterior distribution, and also the ability to incorporate additional likelihoods, corresponding to other cosmological datasets.

[1] `http://cosmologist.info/cosmomc/`

CHAPTER 5
ΛCDM

5.1 Introduction

The standard cosmological paradigm, as explored in Section 1.3, is described through the six-parameter ΛCDM model. In Table 1–1 we presented the set of six parameters which define this model as well as a selection of derived parameters. In this chapter we present the primary focus of this work, an analysis of the comparison between the observed galaxy cluster abundance with that which is expected from theory. In particular, we will focus upon parameter constraints obtained through the cluster likelihood implementation, as derived in the previous chapter. We will also examine the impact of supplementary datasets, both independently and when combined jointly with the cluster data and likelihood.

5.2 Cluster Constraints

We employ the MCMC framework developed in Section 4.5 to constrain the ten-dimensional parameter space of cosmological and cluster scaling relation parameters. To implement the MCMC algorithm we use the CosmoMC analysis package introduced in Section 4.5 [154]. As it is designed for cosmological MCMC analyses, the CosmoMC package provides a convenient and efficient method for parameter estimation, while also permitting the incorporation of external cosmological datasets. As shown in Section 4.5, in the MCMC methodology, marginalization over model parameters is a straightforward procedure. Throughout this analysis, all "best-fit" parameter values will correspond to the mean of the marginalized posterior while parameter uncertainties will correspond to the standard deviation of this distribution (unless otherwise noted).

As described in Section 4.4, the cosmological dependence of the cluster likelihood is confined only to those parameters which affect the matter power spectrum, the linear growth function, and/or the comoving volume element. Cosmological parameters which have no bearing on these quantities will be unconstrained by the cluster-only analysis. Thus, priors will be placed upon both the cosmological and scaling relation parameters. Quantitative descriptions of these priors are presented in Table 5–1. We note for clarity that A_{SZ} refers to the normalization of the mass-significance scaling relation and not the relative amplitude of the SZ power spectrum, as defined in some literature [11, 162, 163, 164, 165].

As the optical depth to reionization τ does not enter into the cluster-only likelihood we have elected to fix this parameter to a fiducial value. We have also placed conservative top-hat priors upon the other cosmological parameters. These cosmological priors were informed through the fits and constraints provided by the WMAP 7-year dataset (WMAP7) [11, 18]. For these parameters, the extents of the top-hat priors were defined to exceed the 3σ limits of the WMAP constraints, limiting the cluster analysis to physically reasonable regions of parameter space. The prior placed on H_0 is enforced by default in CosmoMC. The prior constraints listed for the scaling relation parameters have been informed though the use of simulations as previously discussed in Section 4.3. They are modeled as Gaussian uncertainties and are presented in Table 5–1.

Table 5–1: Cluster-only ΛCDM parameter constraints

Parameter	Cluster-only Fit	Prior
Cosmological Parameters		
$\Omega_b h^2$	0.0230 ± 0.0073	0.010 - $0.035^{\dagger}$
$\Omega_c h^2$	0.109 ± 0.022	0.01 - $0.21^{\dagger}$
Ω_Λ	0.625 ± 0.180	0.0 - $1.0^{\dagger}$
A_s	$(2.387 \pm 0.242)\times10^{-9}$	$(2.0$ - $2.8)\times10^{-9\dagger}$
n_s	0.959 ± 0.036	0.90 - $1.03^{\dagger}$
τ	0.088^{1}	0.088^{1}
Scaling Relation Parameters		
A_{SZ}	5.74 ± 1.83	$6.01 \pm 1.80^{\ddagger}$
B_{SZ}	1.44 ± 0.18	$1.31 \pm 0.26^{\ddagger}$
C_{SZ}	1.67 ± 0.61	$1.60 \pm 0.80^{\ddagger}$
D_{SZ}	0.211 ± 0.042	$0.21 \pm 0.04^{\ddagger}$
Derived Parameters		
H_0 (km s^{-1} Mpc^{-1})	64.0 ± 15.2	40.0-$100.0^{\dagger}$
σ_8	0.745 ± 0.082	—
Ω_m	0.375 ± 0.180	—

[1] fixed to τ=0.088
† Top-hat prior
‡ Gaussian prior

The first step in this analysis will be to examine the parameter constraints provided by the V10 cluster data alone. To that end, we have taken the cluster likelihood calculation (detailed in Chapter 4) and incorporated it as a module in the CosmoMC package. For this cluster-only analysis the MCMC algorithm was run with four parallel chains, sampling more than 100 000 points in total and exceeded the recommended required convergence criteria for the the Gelman-Ruben statistic: $(\hat{R}-1) < 3\times10^{-2}$. The parameter fits obtained from this calculation are presented in Table 5–1 along with their associated 1σ uncertainties. A complete set of confidence intervals for all parameters is presented in Figure 5–1.

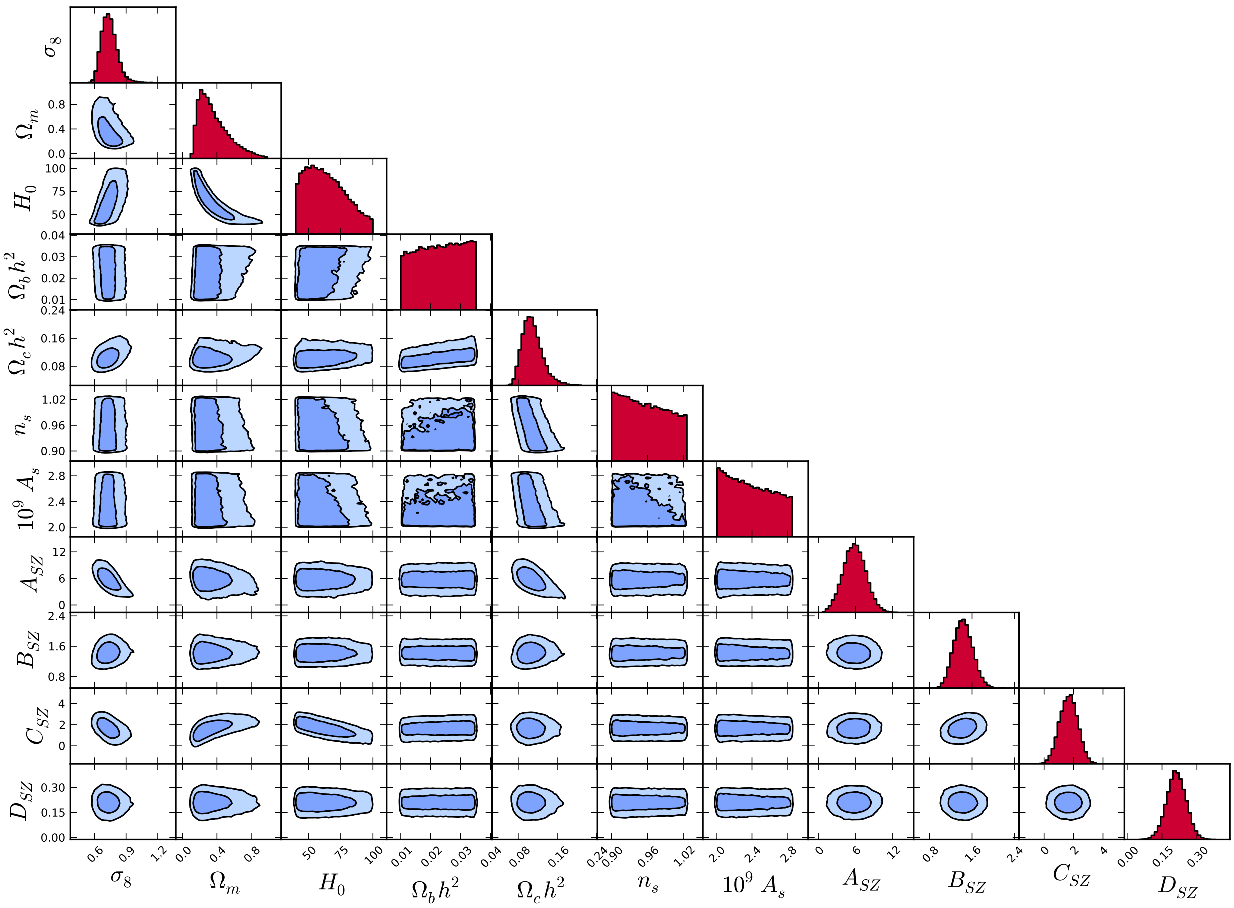

Figure 5–1: ΛCDM and scaling relation parameter grid displaying the 68% and 95% confidence contours for the V10 cluster-only likelihood. Also shown are the marginalized, one-dimensional histograms.

The analysis of the results presented in Table 5–1 will first focus primarily upon the constraints to the cosmological parameters, followed by those to the cluster scaling relation. We will begin by examining parameters to which the cluster likelihood demonstrates limited sensitivity. These will include the physical baryon density $\Omega_b h^2$, the spectral index of the initial density perturbation spectrum n_s, and the amplitude of the initial curvature spectrum A_s. The marginalized mean and 1σ uncertainties for these parameters are presented in Table 5–1 while their two-dimensional 68% and 95% confidence intervals are shown in Figure 5–1.

From Figure 5–1 it is clear that the constraints on these parameters originate largely from the top-hat priors utilized in this analysis. While the marginalized histograms presented in Figure 5–1 do indicate some limited constraining power, it is the imposition of the top-hat prior which constrains these parameters. As described earlier, these priors limit the cluster analysis to regions of parameter space not excluded at high significance by the WMAP7 dataset.

The apparent insensitivity of the cluster likelihood to A_s and n_s is not surprising, given the physical scale upon which these parameters are defined. In this cosmological parameterization, these parameters are defined with respect to the physical scale $k = 0.002$ Mpc^{-1}. This scale is much larger than those probed by galaxy clusters which, as massive collapsed objects, represent the non-linear regime. These smaller scales, which signify the onset of non-linear structure formation, are of the order $k \approx 0.2$ Mpc^{-1} today [166, 167].

The cluster likelihood also shows relative insensitivity to the physical baryon density $\Omega_b h^2$. As shown in Figure 5–1, within the range permitted by the top-hat prior, the cluster likelihood demonstrates only a weak preference for increased values of $\Omega_b h^2$. The main effect of an increased baryon density, as regards structure formation, is the suppression of power on small scales, as demonstrated in Figure 1–4 [4, 53]. Similar to the constraints on n_s and A_s, the cluster likelihood constraint on $\Omega_b h^2$ is largely an artifact of the top-hat priors used in this analysis.

As we shall present in the following section, parameters such as n_s and A_s are constrained to much higher precision by experiments which are sensitive to structure on very large scales, for example the measurement of the CMB angular power spectrum performed by the WMAP satellite [18, 11]. For this reason we will instead focus upon the derived parameter σ_8, which acts as a measure of the normalization of the matter power spectrum on scales ($8h^{-1}$ Mpc) close to those probed by galaxy clusters. The primary motivation for maintaining the large-scale normalization will rest in the ability to compare with, and include data from, experiments such as the WMAP satellite.

We will now examine the cosmological parameters which are most constrained by the cluster-only likelihood. We will begin by examining the cluster-scale matter-power spectrum normalization parameter, σ_8. In Table 5–1 we present the best-fit value and 1σ uncertainty for the derived σ_8 parameter. The full set of two-dimensional confidence intervals for this parameter are presented in Figure 5–1. From this figure, we see that not only is σ_8 well-constrained by the cluster analysis but that this constraint is largely independent of the priors placed upon the large scale normalization A_s or the spectral index n_s.

The origin of the cluster likelihood sensitivity to the σ_8 parameter can be traced back to the underlying halo mass function. This function, which is used to predict the abundance of galaxy clusters as a function of cosmology, scales quite steeply with mass, as shown in Figure 2–2. Quantitatively, we find that, within the mass regime relevant to this analysis ($M_{200} \sim 5 \times 10^{14} h^{-1} M_{\odot}$), the mass function for a fiducial WMAP-preferred cosmology varies steeply with mass; $dN \propto M^{-2.5}$. Moreover, through examination of Figure 1–6 we find that, by again focusing on cluster-relevant scales ($R \sim 8h^{-1}$Mpc), the mass varies with the variance in the smoothed density field such that $\sigma(M) \propto M^{-0.25}$. The combination of these two scalings indicates that, for a reasonable choice of cosmological parameters, the predicted abundance of galaxy clusters should scale roughly as σ_8^{10}. This rather steep dependency upon σ_8 is presented graphically in Figure 5–2, where this relation is supported through a comparison of the integrated cluster counts, as presented for the representative cosmologies.

There also exists degeneracies between σ_8 and other parameters in the cluster likelihood analysis. One example of such a degeneracy exists between σ_8 and the normalization of the mass-significance scaling relation A_{SZ}, as shown in Figure 5–1 and enlarged in Figure 5–3. Regions of parameter space with high A_{SZ} favour low values of σ_8 and vice-versa. The value of the constraint on A_{SZ} presented in Table 5–1 indicates that this constraint originates almost entirely from the Gaussian prior, as shown by the histogram in Figure 5–1.

It has been proposed that, for large cluster surveys, the normalization of the mass-observable relation may be calibrated through measurements of the evolution in the cluster abundance as a function of mass or redshift [168, 169, 170]. However, such self-calibration generally requires catalogs which are much larger than the V10 sample used here and are thus not employed in our analysis. This reliance upon the A_{SZ} prior indicates that the calibration of the mass-significance scaling relation is of crucial importance in the cluster likelihood, affecting both the accuracy and precision of the resulting constraints.

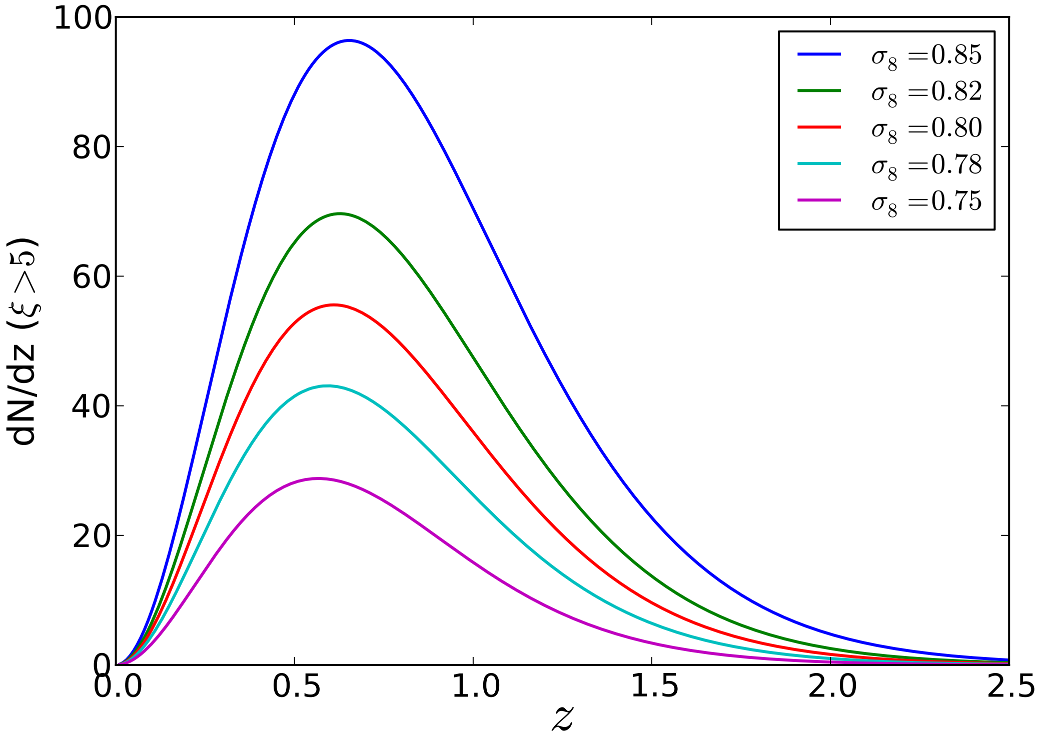

Figure 5–2: Differential numbers counts as a function of redshift for a suite of σ_8 values, ranging from 0.75 (bottom) to 0.85 (top). The integrated cluster number counts in each case are 24.0, 37.6, 50.0, 64.5, and 91.1 as a function of rising σ_8, scaling roughly as σ_8^{10}.

Although the amplitude and uncertainty of A_{SZ} is largely set by the simulation-derived prior, there are other promising methods of reducing this uncertainty. One such method is through the use of complementary cluster observables as sources of calibration for the cluster scaling relation [171]. Targeted optical, X-ray, and weak lensing observations are among these complementary cluster observables. Versions of these analyses involving SPT-detected galaxy clusters are ongoing, where recent examples can be found in Andersson et al. [172], Benson et al. [171], Reichardt et al. [139], and High et al. [173].

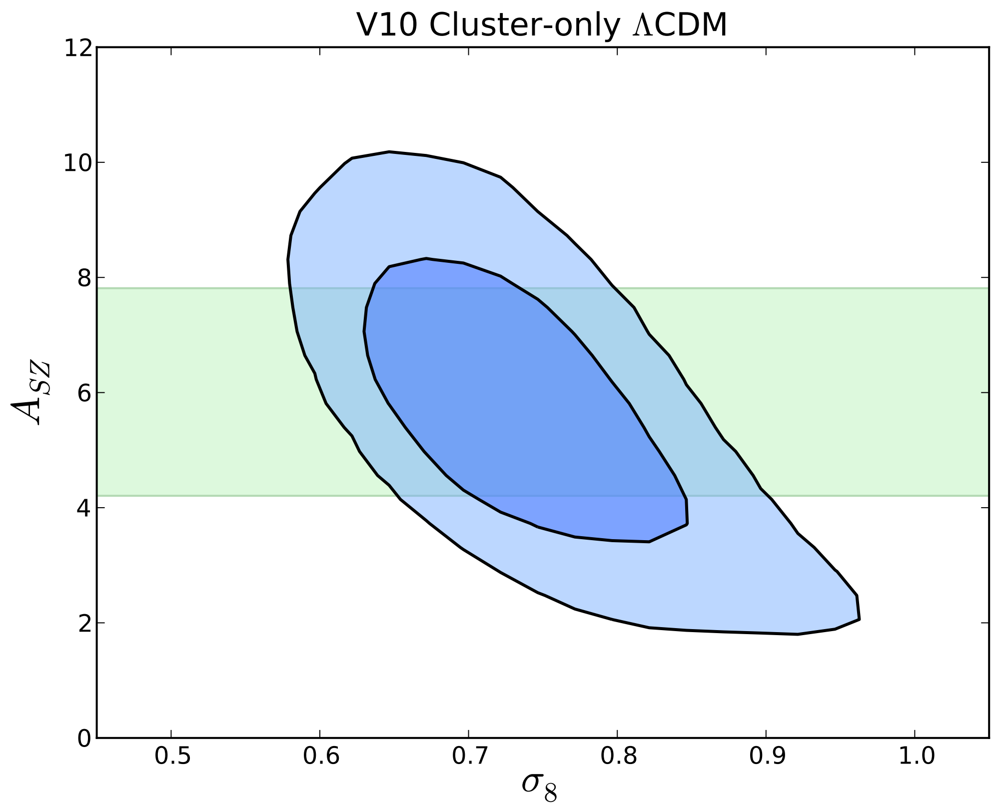

Figure 5–3: Two-dimensional 68% and 95% confidence intervals for the parameters σ_8 and A_{SZ} in the V10 cluster-only analysis. The 1σ Gaussian prior on A_{SZ} is represented by the shaded horizontal band. This panel is an enlargement of the confidence intervals presented in Figure 5–1.

The final two cosmological parameters which we will discuss are the Hubble constant H_0 and the matter density Ω_m. Each of these parameters serves to modify the matter power spectrum to which the cluster likelihood is sensitive, with the latter parameter, Ω_m, also affecting the cosmological growth function. The modification to the matter power spectrum by these two parameters is commonly parameterized through the *shape function* $\Gamma = \Omega_m h$ and, as evidenced by Figure 5–4, causes deviations in the matter power spectrum on cluster scales [4, 53, 50]. As shown in Table 5–1 and Figure 5–1, the Hubble parameter is only weakly constrained through these effects.

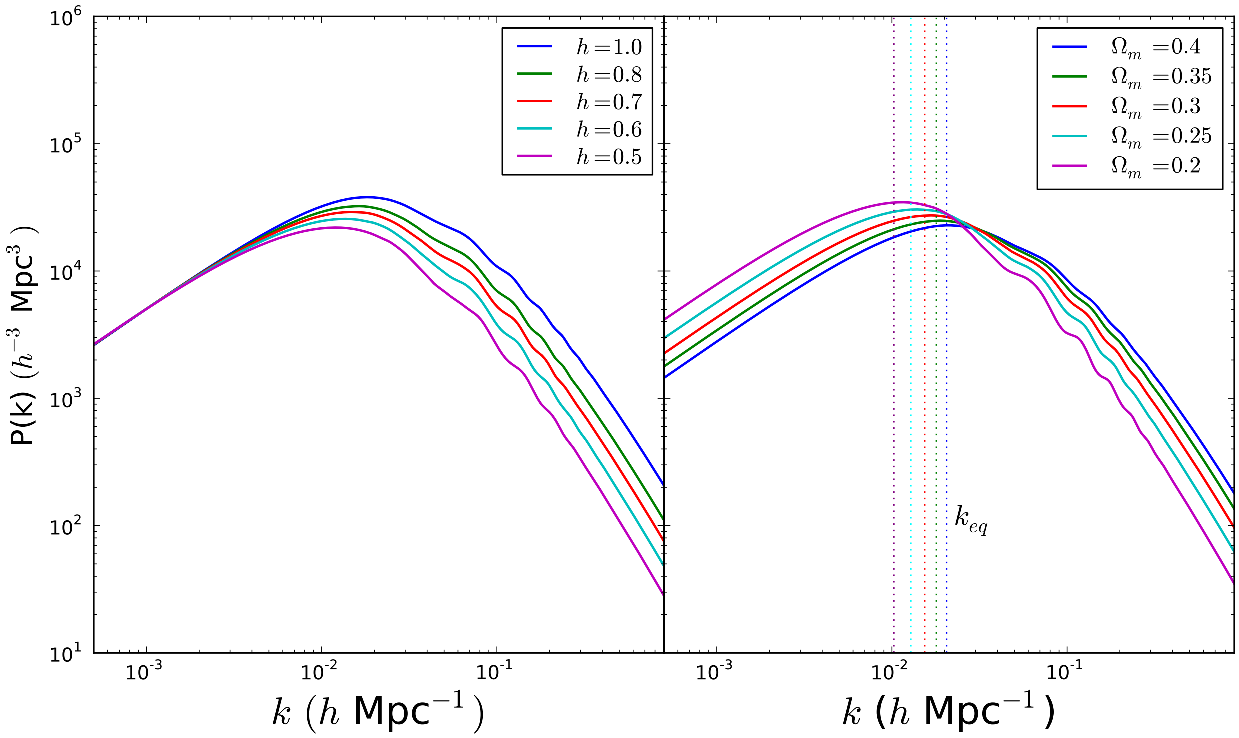

Figure 5–4: Matter power spectra are plotted as functions of both H_0 and Ω_m. On the left, spectra are plotted for a set of Hubble constant parameter values ranging from 50 (bottom) to 100 (top) km s^{-1} Mpc^{-1}. On the right, spectra are plotted for a set of matter densities ranging (at small physical scales) from 0.2 (bottom) to 0.4 (top). The amplitude of the matter power spectra on large physical scales varies inversely with the matter density. Also shown are the matter-radiation equality scales, which occur at decreasing physical scales as a function of increasing Ω_m.

The matter density Ω_m serves to modify both the amplitude and shape of the matter power spectrum, which in turn affects cluster abundances. These shifts in amplitude were first described in Section 1.5 through Equation 1.53, where it was shown that, for a fixed potential, the amplitude of the matter power spectrum varies inversely with the matter density; this relation is demonstrated in Figures 1–5 and 5–4.

The matter density also alters the cosmological growth function, as shown in Figure 1–3. These shifts in Ω_m modify the growth function and alter the predicted distribution of clusters as a function of redshift. In order to constrain the growth of structure, the input cluster catalog must provide a wide sampling of redshift space. Fortunately, through selecting clusters via their SZ signatures, the clusters utilized in this analysis span out to $z > 1$. The observed abundance of clusters at these high redshifts places informative constraints upon both the growth function and matter density.

This constraint on the evolution of the cluster abundances is also evident in the degeneracy between Ω_m and the scaling relation parameter C_{SZ}, as seen in Figure 5–1. Both parameters alter the predicted abundance of clusters as a function of redshift: Ω_m through the cosmological growth function and C_{SZ} through the evolution of the mass-observable scaling relation.

In terms of the cluster scaling relation parameters, Table 5–1 indicates no significant changes in their best-fits with respect to their prior values. However, the uncertainties associated with the mass and redshift evolution in the scaling relation,

B_{SZ} and C_{SZ}, are each reduced by approximately 25% when compared with their priors. Thus, the cluster analysis shows no discrepancy with the simulation-calibrated scaling relation priors.

5.3 Supplementary Data

In the previous section we explored the parameter constraints offered by the cluster-only likelihood analysis. Only cosmological parameters which alter the matter power spectrum, cosmological growth function or comoving volume element influence the cluster analysis and parameters which are sensitive to physical scales beyond the regime probed by galaxy clusters are poorly constrained by this analysis. Due to these limitations we applied broad top-hat priors to the cosmological parameters, limiting them to physically reasonable regions of parameter space (as defined by the WMAP7 constraints). In this section we will explore the use of supplementary datasets as a means of mitigating the need for these cosmological priors.

The primary dataset which we will employ is the WMAP experiment's 7-year results [11, 18, 174]. WMAP is a satellite designed primarily for the observation of anisotropies in the CMB. As described in Dunkley et al. [175], the WMAP likelihood function is defined as a sum of likelihood components. These individual likelihoods correspond to a variety of CMB-derived WMAP data products. Included in these are the CMB temperature (TT), E-mode polarization (EE), B-mode polarization (BB), and temperature-polarization cross-correlation (TE) power spectra. Detailed descriptions regarding the construction of this likelihood and cosmological parameter estimation methods can be found in Dunkley et al. [175] and Larson et al. [18]. WMAP data and likelihood software are provided by the Legacy Archive for

Microwave Background Data Analysis (LAMBDA)[1] . Illustrative examples of the temperature angular power spectrum are presented in Figure 5–5.

The WMAP satellite provides a powerful probe of the early universe and is capable of yielding stringent constraints for a variety of cosmological models. In this section we will explore the constraints provided by the WMAP 7-year dataset for the ΛCDM cosmological model while also studying the improvements from the addition of galaxy cluster data.

As a first step in this analysis, we will examine the constraints provided solely through the use of the WMAP7 dataset. To do so, we will again employ the MCMC process through the use of CosmoMC, now making use of the WMAP7 data. Here we fix all of the scaling relation parameters to their fiducial values as they will not influence this aspect of the analysis. We also attempt to mitigate as much as possible the effect of cosmological priors by extending the existing top-hat priors well beyond their previous limits, to values similar to those set in Larson et al. [18]. For this analysis, the MCMC algorithm was run with four parallel chains, again sampling more than 100 000 points in the parameter space and exceeding the required convergence criteria, satisfying the Gelman-Ruben statistic such that $(\hat{R} - 1) < 3 \times 10^{-2}$. The recovered cosmological constraints from this analysis are presented in Table 5–2 while the 68% and 95% confidence intervals for all relevant parameters are presented in Figure 5–6.

[1] We acknowledge the use of the Legacy Archive for Microwave Background Data Analysis (LAMBDA). Support for LAMBDA is provided by the NASA Office of Space Science: `http://lambda.gsfc.nasa.gov/product/map/dr4/likelihood_get.cfm`

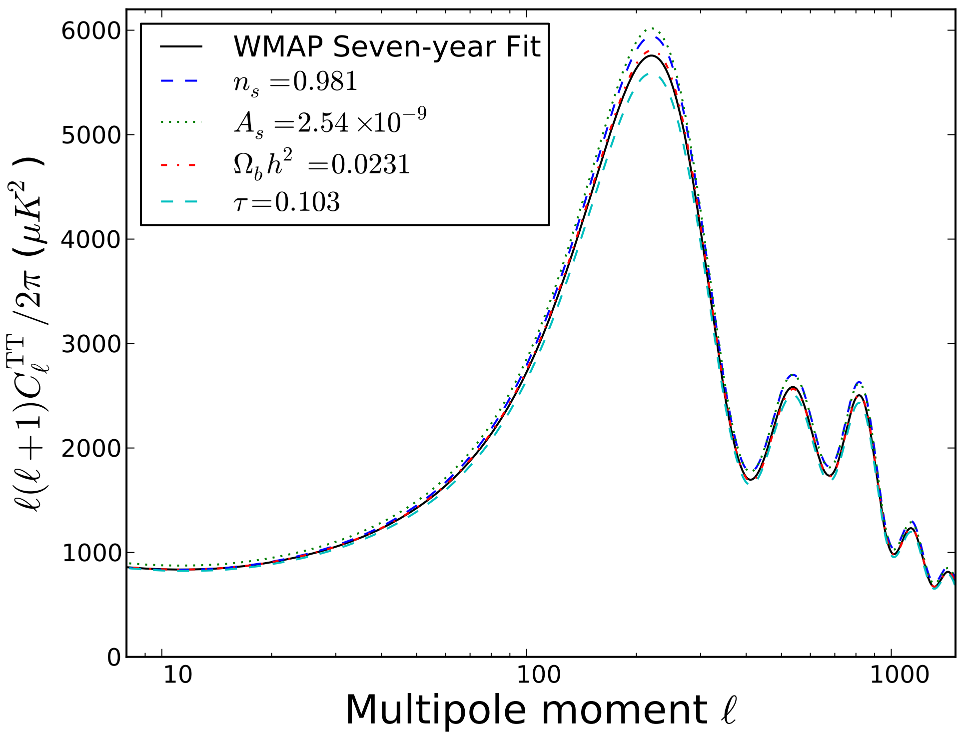

Figure 5–5: Examples of CMB temperature (TT) angular power spectra. The cosmological dependence of the temperature power spectrum is indicated for an illustrative subset of parameters. Spectra are modified from the best-fit cosmology to the parameter values indicated, while holding all other parameters fixed. The cosmological parameter values presented represent 1σ increments to their WMAP seven-year best-fit values, as defined in Table 5–2.

As with the cluster analysis, we will begin by examining the parameters which define the amplitude and tilt of the initial curvature and density perturbation spectra, specifically A_s and n_s. In the preceding cluster analysis it was found that these parameters were poorly constrained by the cluster-only data, due partially to the fact that they are defined on a scale much larger ($k = 0.002$ Mpc^{-1}) than that probed

Table 5–2: ΛCDM combined parameter constraints

Parameter	Cluster-only Fit	WMAP7 Fit	Cluster + WMAP7 Fit
Cosmological			
$\Omega_b h^2$	0.0230 ± 0.0073	0.0225 ± 0.0006	0.0225 ± 0.0006
$\Omega_c h^2$	0.109 ± 0.022	0.112 ± 0.006	0.109 ± 0.005
Ω_Λ	0.625 ± 0.180	0.725 ± 0.029	0.741 ± 0.025
$10^9 A_s$	2.387 ± 0.242	2.427 ± 0.112	2.385 ± 0.106
n_s	0.959 ± 0.036	0.967 ± 0.014	0.969 ± 0.014
τ	$0.088^\dagger$	0.088 ± 0.015	0.088 ± 0.015
Scaling Relation			
A_{SZ}	5.74 ± 1.83	$6.01^\dagger$	4.92 ± 1.00
B_{SZ}	1.44 ± 0.18	$1.31^\dagger$	1.48 ± 0.18
C_{SZ}	1.67 ± 0.61	$1.60^\dagger$	1.40 ± 0.45
D_{SZ}	0.211 ± 0.042	$0.21^\dagger$	0.209 ± 0.042
Derived			
H_0 (km/s/Mpc)	64.0 ± 15.2	70.1 ± 2.5	71.3 ± 2.3
σ_8	0.745 ± 0.082	0.813 ± 0.030	0.796 ± 0.026
Ω_m	0.375 ± 0.180	0.275 ± 0.029	0.259 ± 0.025

† fixed to fiducial value
Fiducial V10 scaling relation: $A_{SZ} = 6.01 \pm 1.80$, $B_{SZ} = 1.31 \pm 0.26$, $C_{SZ} = 1.60 \pm 0.80$, $D_{SZ} = 0.21 \pm 0.04$

by galaxy clusters. For WMAP, however, these large scales are well-constrained. Moreover, its ability to measure the CMB temperature anisotropy spectrum across a large range in scale permits an excellent measurement of n_s.

Beyond simply measuring the amplitude and observed tilt of the temperature anisotropy spectrum, WMAP is also able to measure the acoustic peaks. The heights and positions of these peaks are sensitive to the conditions present in the baryon-photon plasma in the early universe and their measurement yields constraints on the fundamental parameters which define cosmology [20, 46]. Based on this information, WMAP is able to place tight constraints on the physical matter density in the universe as well as the physical baryon density, a parameter to which the cluster likelihood showed very limited sensitivity. These constraints are presented in both

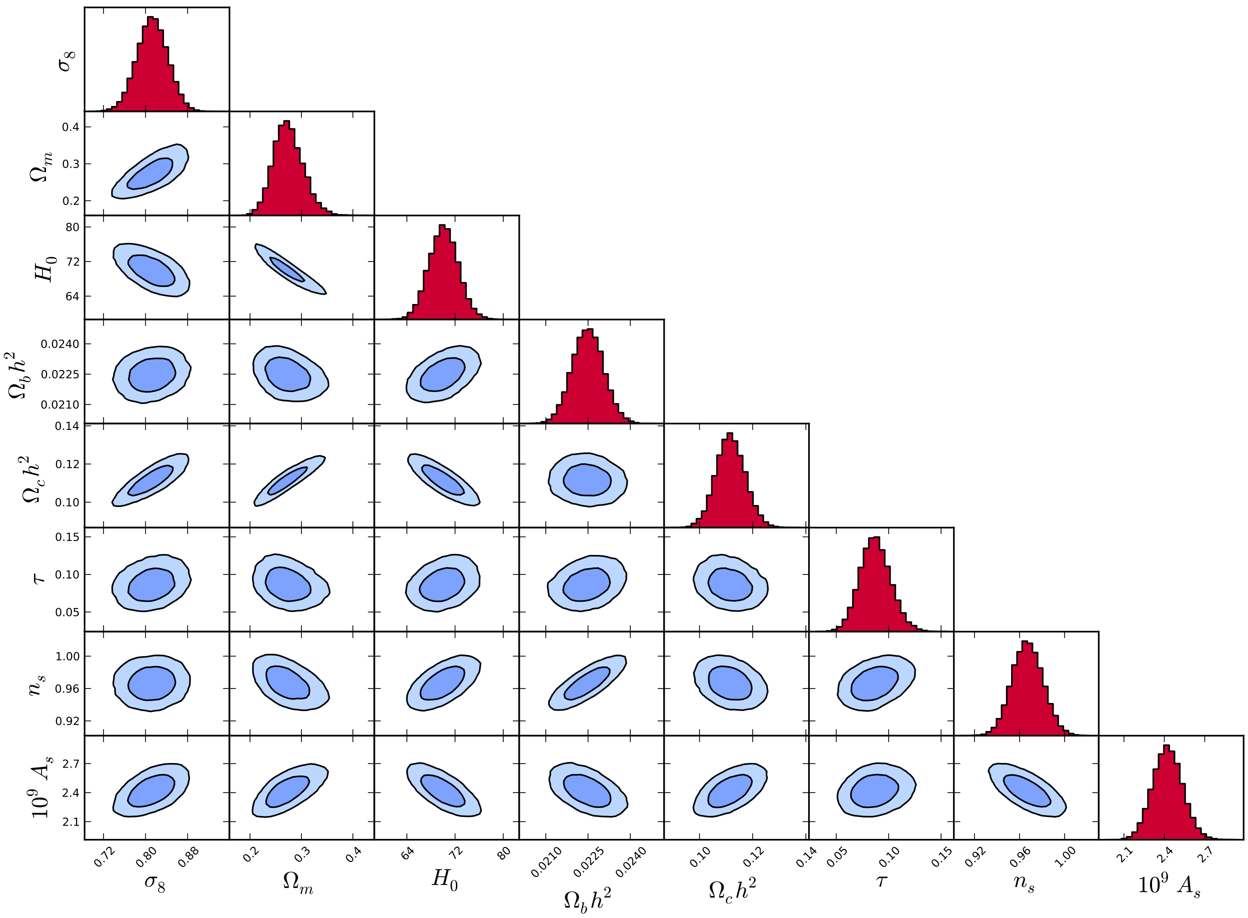

Figure 5–6: ΛCDM parameter grid displaying 68% and 95% confidence intervals for the WMAP7 dataset. Also shown are the marginalized, one-dimensional histograms.

Table 5–2 as well as Figure 5–6. The extents of these constraints lie well within the top-hat priors employed in the cluster-only analysis (which have been expanded here).

The inclusion of WMAP7 data also constrains the reionization history of the universe through the parameter which describes the optical depth to reionization,

τ. In the cluster-only analysis this parameter is fixed to a fiducial value as it is completely independent of the cluster likelihood. However, in the case of the WMAP7 observations, this parameter does affect the shape of the angular power spectra. The onset of the reionization period, as measured by τ, permits the scattering of CMB photons with free electrons and serves to provide a scale-dependent suppression of the temperature angular power spectra while also creating a polarization signal [20, 176, 46].

The final parameter to be examined from the WMAP7 analysis is the Hubble constant. The WMAP7 data does not constrain the Hubble constant directly, as this is a measure of the expansion rate of the local universe and the WMAP7 data primarily samples only a single surface, corresponding to the time of recombination. However, as noted in Spergel et al. [46] and presented in Equations 1.20 and 1.22, in the flat ΛCDM cosmological framework the distance to this last scattering surface depends only upon the component energy densities Ω_i and H_0 and thus a measurement of this distance is sufficient to place a constraint upon the Hubble parameter in the ΛCDM model. In non-flat universes, or those with a non-cosmological-constant dark energy component, this measurement of H_0 will be subject to strong degeneracies with other parameters.

From these WMAP7 results we can compare to, and evaluate the consistency of, the cluster likelihood constraints. As the cluster scaling relation parameters are fixed in the WMAP7 likelihood, we will focus upon the consistency of the cosmological constraints. From Table 5–2 we see that, when compared with the V10 cluster analysis, the WMAP7 analysis offers improved constraints for all cosmological parameters listed. For parameters to which the cluster likelihood showed limited sensitivity (τ and $\Omega_b h^2$ for example) this is not surprising. For parameters which have been shown to strongly affect cluster abundances (σ_8 for example) the cluster constraint, while competitive, is still weaker than that offered by the WMAP7 data.

Inspection of Table 5–2 also reveals the cluster and WMAP7 constraints to be quite consistent. For all cosmological parameters, the best-fit values from the cluster likelihood agree the corresponding WMAP7 values at the 1σ level. Therefore, despite increased uncertainties, the cosmological parameter fits recovered by the cluster analysis agree well with those derived from the WMAP7 data. Thus, while offering unique constraints based upon the late-time distribution of matter in the universe, the cluster likelihood is not yet able to single-handedly improve upon the precise early-universe constraints offered by the WMAP7 data.

We will now examine the effect of including both galaxy cluster and WMAP data in the combined likelihood. The resulting constraints are presented in Table 5–2. In Figure 5–7 we present the 68% and 95% confidence contours for both the WMAP7 data as well as the combined WMAP7 and cluster data.

From Table 5–2 we see that none of the cosmological parameters fits are significantly altered by the inclusion of cluster data. The uncertainties associated with these parameters are also largely unchanged, showing some improvement in the combined fit. In particular, the matter density Ω_m and the derived amplitude parameter σ_8 both display a $\gtrsim 10\%$ improvement with respect to the WMAP7 uncertainty. As shown in Figure 5–8, there exists a degeneracy between these two parameters. For

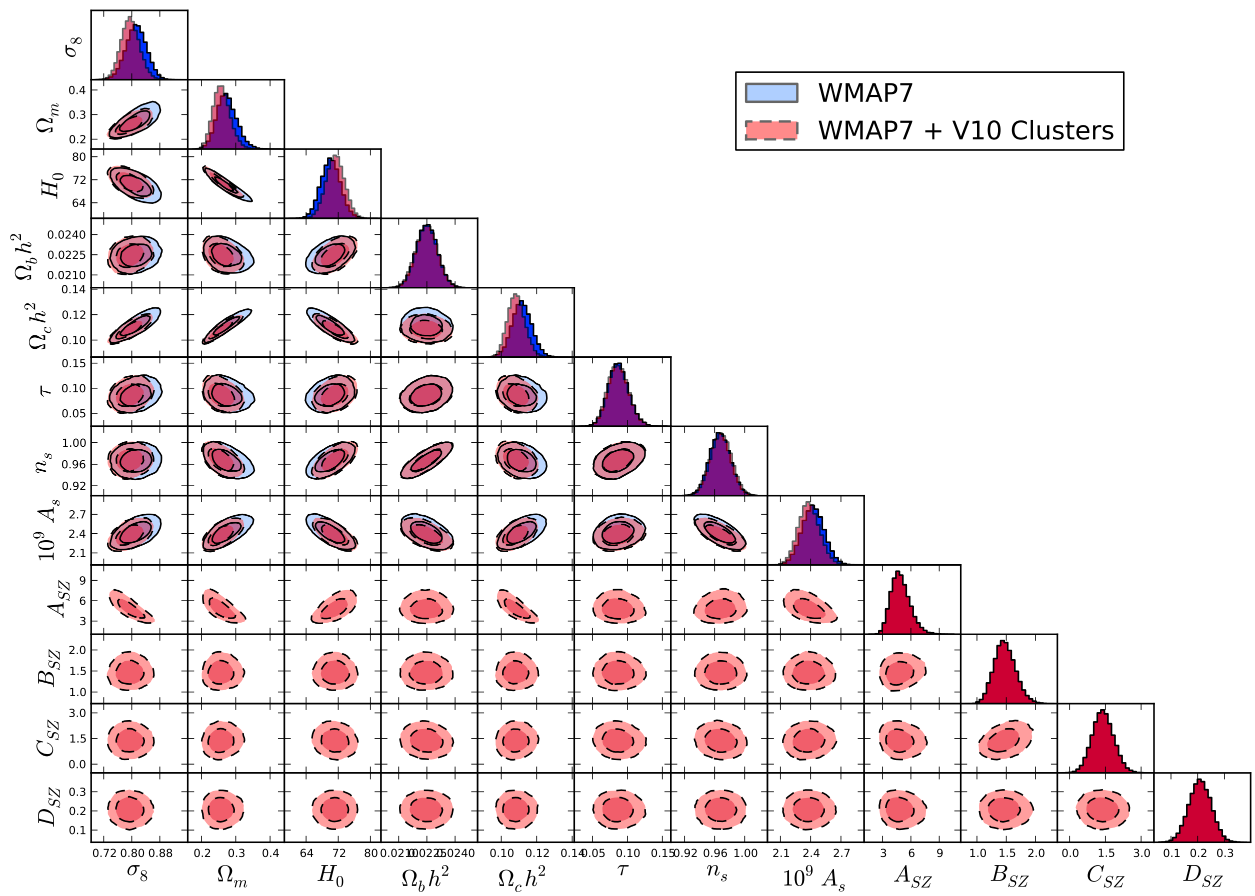

Figure 5–7: ΛCDM parameter grid displaying the 68% and 95% confidence intervals for the WMAP7 dataset as well as the combined WMAP7 and cluster dataset. Also shown are the marginalized, one-dimensional histograms. The added cluster data are shown to modestly improve constraints on parameters upon which the cluster likelihood relies.

these parameters, the origin of this improved constraint lies in the sensitive dependence of the cluster abundance to the amplitude of the matter power spectrum on cluster scales.

Beyond the small improvement to its uncertainty, the σ_8 parameter also decreases in the combined WMAP7 and clusters fit. This indicates that the V10 cluster catalog contains fewer clusters than would be predicted from the WMAP7-only fit using the fiducial scaling relation. For the approximate scaling derived in the previous section, this slight shift in σ_8 (ignoring changes to other parameters) results in a change of more than 20% in the predicted cluster abundance. However, this decreased abundance is still well within the range predicted by varying the scaling relation parameters within their priors.

The final parameters to be discussed are those which define the mass-ζ scaling relation. The uncertainty associated with A_{SZ} is decreased by more than 40% due to the addition of WMAP7 data to the cluster likelihood. Its best-fit value also shifts to a lower value (as shown in Table 5–2), decreasing from $A_{SZ} = 5.74 \pm 1.83$ to $A_{SZ} = 4.92 \pm 1.00$ in the joint WMAP7-cluster constraint. This decrease indicates that the fiducial normalization of the simulation-calibrated scaling relation may be slightly elevated, predicting an excess of clusters above our detection threshold. However, the recovered value from the joint analysis is still well within the scaling relation Gaussian prior of $A_{SZ} = 6.01 \pm 1.80$. This is presented graphically in Figure 5–9, where the improved constraint and trend to lower A_{SZ} is clear.

This decrease in the scaling relation normalization indicates that the observed SZ significances in the V10 catalog are, in general, slightly lower than those expected from simulation for the best-fit WMAP7 cosmology. This shift still lies well within the 1σ prior placed upon this parameter but does suggest that the simulated cluster data used in calibrating the mass-ζ scaling relation may slightly overestimate the

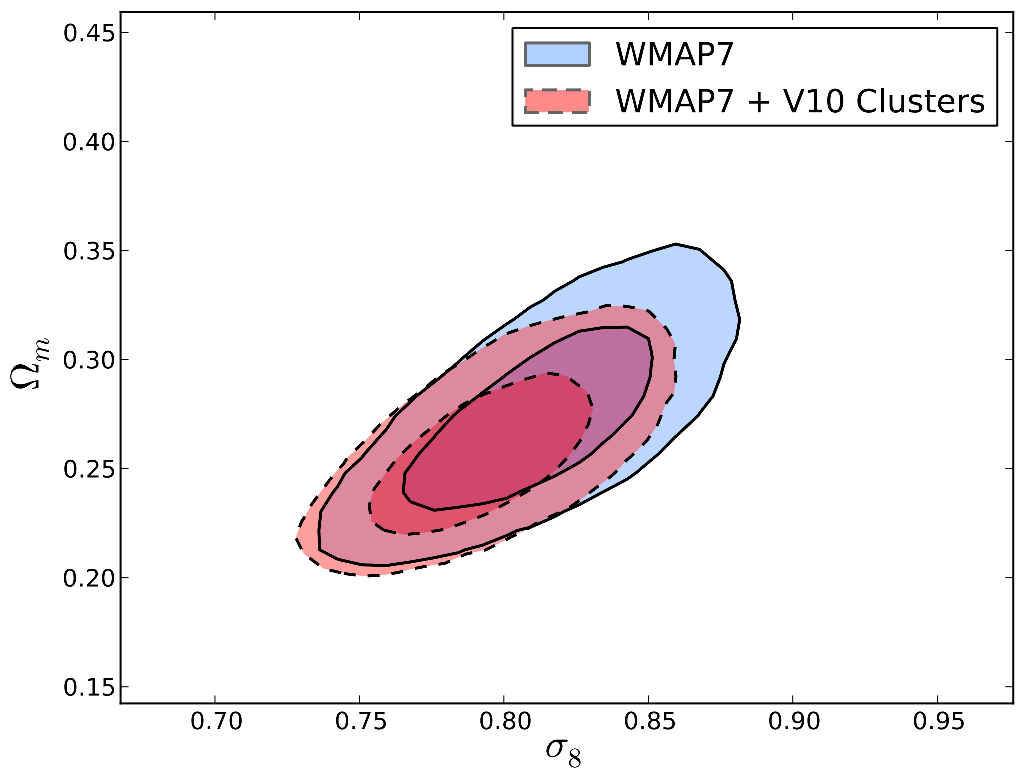

Figure 5–8: Two-dimensional 68% and 95% confidence intervals for the σ_8 and Ω_m parameters. Contours are plotted for WMAP7 data both with and without the V10 cluster data. This panel is an enlargement of the confidence intervals presented in Figure 5–7. Improvements to the constraints due to the addition of cluster data are evident.

cluster SZ flux. A similar behaviour is observed in measurements of the SZ power spectrum obtained from the small-scale CMB temperature anisotropy, where recent observations find a similar deficit in power when compared with fiducial models [162, 163, 164, 11]. Thus, through degeneracies between cosmological and scaling relation parameters in the cluster likelihood calculation, the addition of WMAP7 data shifts the best-fit value and decreases the uncertainty upon the normalization of the mass-ζ scaling relation.

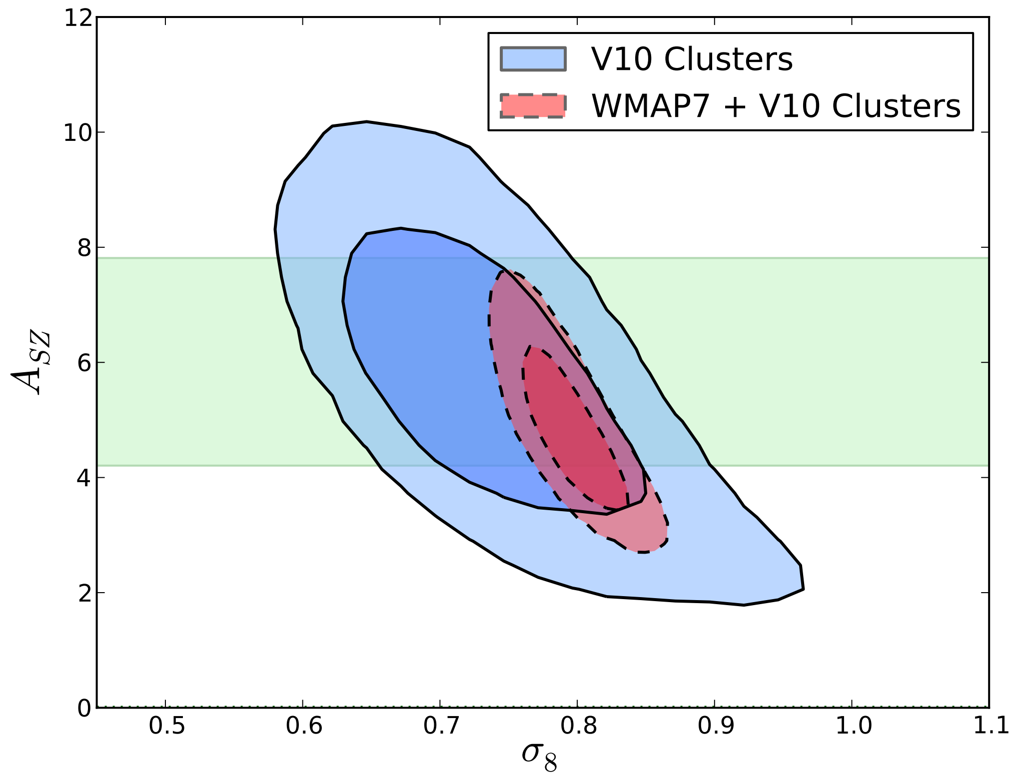

Figure 5–9: Two-dimensional 68% and 95% confidence intervals for the σ_8 and A_{SZ} parameters. Contours are plotted for cluster data both with and without the addition of WMAP7 data constraints. The 1σ Gaussian prior on A_{SZ} is represented by the shaded horizontal band.

As shown in Table 5–2, the best-fit values for B_{SZ} and C_{SZ} do not change appreciably with the addition of WMAP7 data. Only C_{SZ} displays a $\sim 25\%$ reduction in its uncertainty through the addition of this complementary data. Finally we find that neither the best-fit value nor the uncertainty of D_{SZ} (the parameter which governs intrinsic scatter in the the scaling relation) are significantly altered by the addition of WMAP7 data

5.4 Summary

In this chapter we demonstrated the successful implementation of the cluster likelihood evaluation in the presence of the V10 cluster dataset. In so doing, we were able to explore and gauge the effectiveness of the cluster likelihood in constraining parameters, generally separated into a cosmological component, describing the six-parameter ΛCDM model, and a four-parameter component describing the scaling between the cluster mass and its observable, the SZ significance parameter ξ. It was found that the cluster likelihood provides useful cosmological constraints, demonstrating consistency with the canonical ΛCDM model. It was also found that this analysis is sensitive to the shape and extent of the priors, in particular for the scaling relation parameters and, most notably, for the amplitude parameter A_{SZ}.

We explored the effects of including additional data, in the form of the WMAP7 dataset. Through this additional data we constrained parameters to which the cluster likelihood was insensitive, thus mitigating the need for some priors. The WMAP7 data also served to further constrain the cluster likelihood scaling relation parameters. Although the supplementary data did not constrain these parameters directly, degeneracies between scaling relation and cosmological parameters permitted improved constraints. The cluster data were demonstrated to provide limited improvements to constraints, with which the results from the cluster-only analysis were shown to be consistent. As the ΛCDM model is already quite well constrained by the WMAP7 CMB data, the additional constraints offered by the cluster likelihood are modest in comparison. In the following chapters we will again explore the use of supplementary datasets for cosmological models beyond the standard ΛCDM paradigm.

CHAPTER 6
wCDM

6.1 Introduction

In the previous chapter we explored and quantified the parameter constraints offered by galaxy cluster abundances within the ΛCDM framework. It was found that the V10 SZ-selected galaxy cluster data demonstrated general agreement with this standard cosmological model and offered useful constraints for a subset of its parameters. In this chapter we will look to broaden our analysis, exploring the nature of the dark energy component.

As introduced and explored in Section 1.3, the fiducial ΛCDM cosmology can be extended to permit a different equation of state for the dark energy component. In this extended model, we expand our cosmological model to encompass seven parameters: the standard six-parameter ΛCDM set and an additional parameter describing the dark energy equation of state, assumed to be constant in time. This cosmology will be referred to as the wCDM model.

6.2 Clusters and Dark Energy

The effect of dark energy will be manifested through modifications to the cosmic expansion history. This modified expansion rate will impact upon two key quantities which affect the galaxy cluster abundance: the comoving volume element (Equation 1.25) and the growth rate of structure (Equation 1.61).

In Section 1.3 we explored the modifications to the expansion history due to differing dark energy equations of state and contrasted them with the standard ΛCDM model. For the comoving volume element (at a given redshift z), cosmologies with increased expansion rates (less negative w) will possess correspondingly smaller comoving volume elements, thus decreasing the total predicted number of clusters per survey area. Similarly, decreased expansion rates (more negative w) will correspond to larger comoving volume elements (as a function of redshift) and thus increase the predicted abundance of clusters.

In the case of the growth function, the alteration to cluster abundances is characterized by way of the halo mass function, through the matter power spectrum, as per Equations 1.65, 1.67 and 2.12. From these equations we find that, from similar initial conditions, models which predict a reduction in the growth rate of structure also predict a reduction in the late-time abundance of collapsed objects while an opposite effect occurs for increased growth rates.

The combination of these modifications to the comoving volume element and linear growth function can lead to significant changes in the expected cluster abundance as a function of redshift and cluster mass (or SZ significance). Examples of these changes are presented in Figure 6–1, in which we have plotted the expected differential number counts as a function of redshift for a selection of wCDM cosmologies. From this figure it is clear that changes to the dark energy equation of state will manifest themselves through the observed distribution of galaxy clusters in the universe and can thus be constrained via the cluster likelihood evaluation.

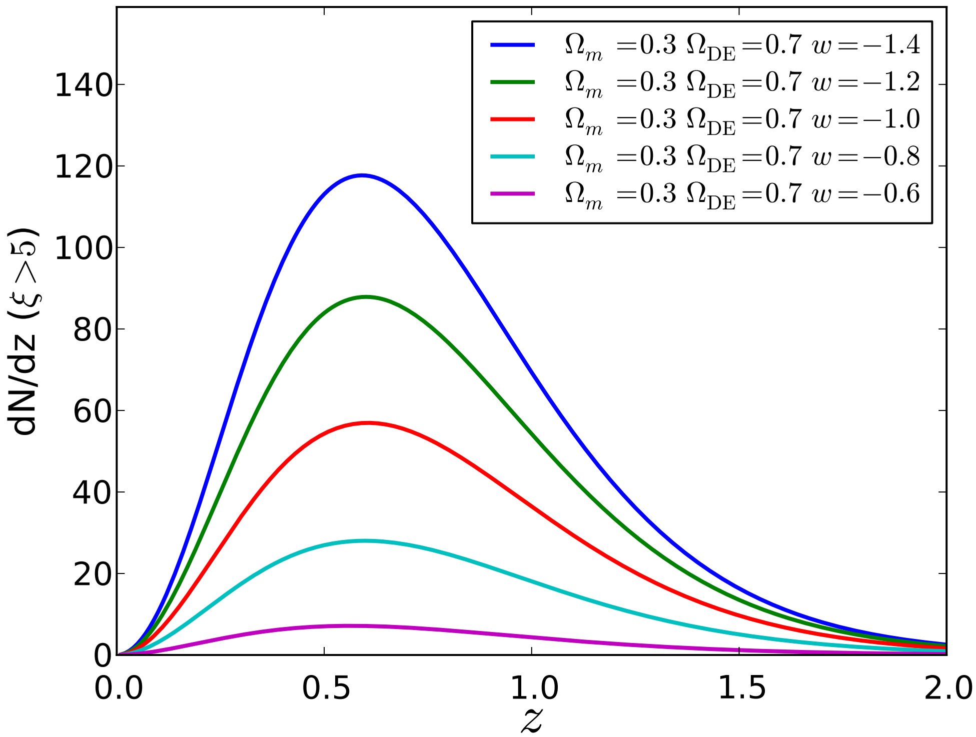

Figure 6–1: Differential cluster number counts as a function of redshift for a selection of cosmologies above an SZ-significance $\xi > 5$. Curves correspond to dark energy equations of state $w = -0.6, -0.8, -1.0, -1.2, -1.4$ from bottom to top respectively. Note that with all other cosmological parameters held fixed the derived σ_8 parameter also increases from 0.66 to 0.87 from bottom to top.

6.3 wCDM Cluster Analysis

For this analysis, we will utilize the same cluster catalog described in Chapter 5. The order of the analysis will also proceed in a manner similar to that followed in Chapter 5, such that we will first examine the cluster-only parameter constraints, followed by the examination of supplementary data and concluding with the joint constraints originating from combining the clusters with external data.

The parameters and priors presented in Table 6–1 are chosen to be identical to those presented in the previous chapter, save for the additional parameter describing the dark energy equation of state, w. For this parameter, we adopt a broad top-hat prior: $-2 < w < 0$. This prior was chosen to be centered about the value which describes the cosmological constant ($w \equiv -1$), as explored in the previous chapter, and permits both a phantom dark energy equation of state ($w < -1$) as well as the possibility of a decelerating expansion ($w > -1/3$).

The resulting posterior distribution is marginalized over all parameters of interest with the resulting best-fit values presented in Table 6–1 with the two-dimensional confidence intervals in Figure 6–2.

As a first point of comparison we contrast the cluster-only wCDM constraints, as presented in Table 6–1, with the previous ΛCDM constraints, as presented in Tables 5–1 and 5–2. The majority of the shared parameters appear largely unchanged under the addition of a varied dark energy equation of state. In fact, other than the additional parameter w, the only parameter listed in Table 6–1 which displays more than a percent-level shift in its best-fit value is C_{SZ}, the parameter governing the redshift evolution in the scaling relation. Even for this parameter, the observed change amounts to a shift of approximately 0.15σ, to a marginally higher value. The majority of the uncertainties listed in Tables 5–1 and 5–2 are also unchanged, except for a nearly 10% increase in the uncertainty of the dark energy density $\Omega_{\rm DE}$ in the wCDM model.

Table 6–1: Cluster-only wCDM parameter constraints

Parameter	Cluster-only Fit	Prior
Cosmological Parameters		
$\Omega_b h^2$	0.0231 ± 0.0072	0.010-0.035†
$\Omega_c h^2$	0.108 ± 0.025	0.01-0.21†
$\Omega_{\rm DE}$	0.627 ± 0.197	0.0-1.0†
A_s	$(2.390 \pm 0.246)\times10^{-9}$	$(2.0\text{-}2.8)\times10^{-9\dagger}$
n_s	0.959 ± 0.036	0.90-1.03†
τ	0.088[1]	0.088[1]
w	-1.16 ± 0.47	-[2.0-0.0]†
Scaling Relation Parameters		
A_{SZ}	5.83 ± 1.79	$6.01 \pm 1.80^\ddagger$
B_{SZ}	1.43 ± 0.18	$1.31 \pm 0.26^\ddagger$
C_{SZ}	1.76 ± 0.58	$1.60 \pm 0.80^\ddagger$
D_{SZ}	0.209 ± 0.042	$0.21 \pm 0.04^\ddagger$
Derived Parameters		
H_0 (km s^{-1} Mpc^{-1})	64.8 ± 15.7	40.0-100.0†
σ_8	0.745 ± 0.083	—
Ω_m	0.373 ± 0.197	—

[1] fixed to τ=0.088
† Top-hat prior
‡ Gaussian prior

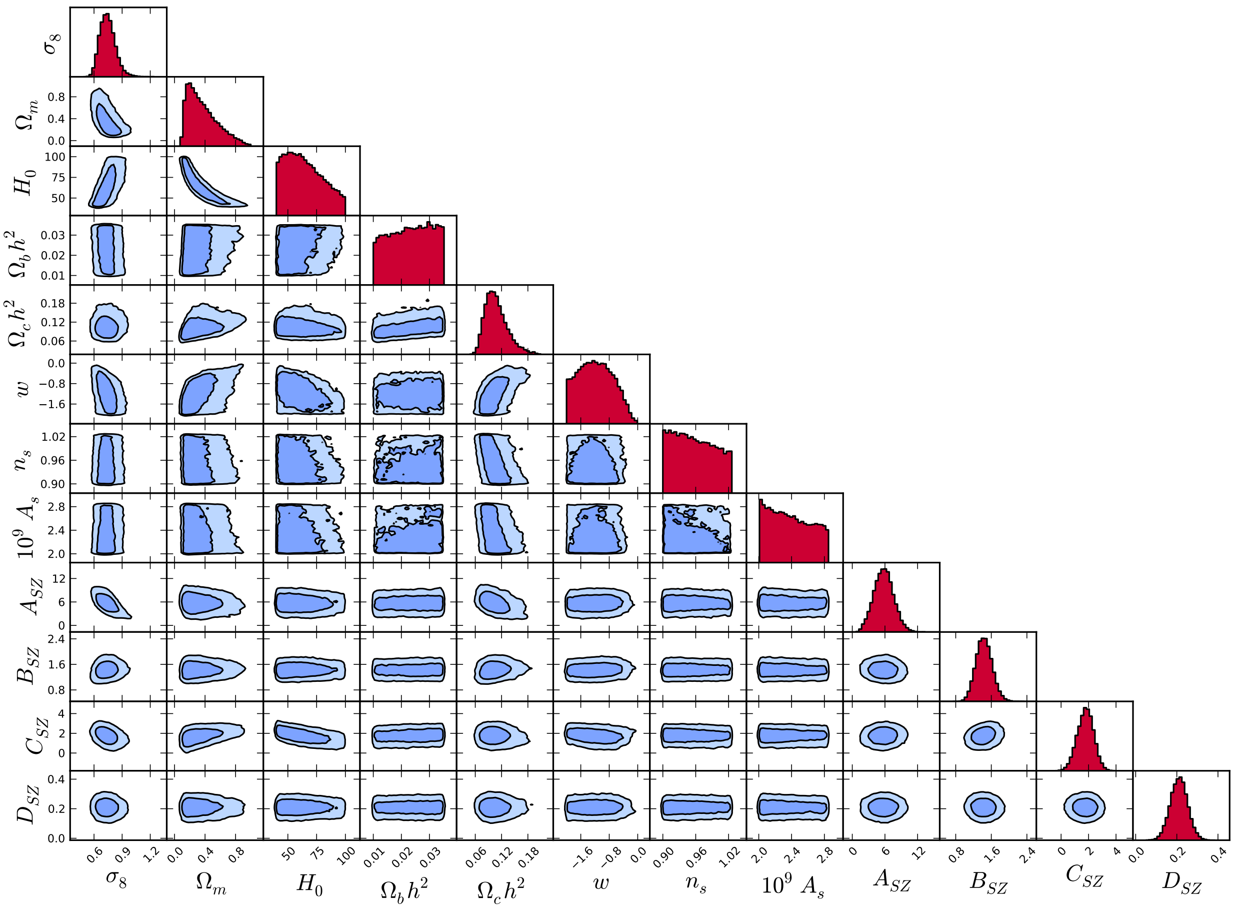

Figure 6–2: wCDM and scaling relation parameter grid displaying the 68% and 95% confidence contours for the cluster-only likelihood. Also shown are the marginalized, one-dimensional histograms.

One explanation for these stable constraints is that parameters which were unconstrained beyond their priors in the ΛCDM case are similarly unconstrained under the inclusion of an additional parameter, and thus their recovered fits are unchanged. This conclusion is supported by the contours and histograms displayed in Figure 6–2 which, as shown in Chapter 5, find n_s, A_s, and $\Omega_b h^2$ to be only weakly constrained by the cluster data, bounded instead by their individual priors.

As demonstrated in Figures 1–2 and 1–3 and detailed earlier in Section 6.2, we expect changes in the dark energy equation of state to affect the predicted abundance of clusters through modifications to the expansion rate, as manifested by the comoving volume element and growth function. As such, we may expect to observe degeneracies between the dark energy equation of state and parameters which affect either or both of these quantities.

The constraint on dark energy, as given in Table 6–1 and Figure 6–2, is $w = -1.16 \pm 0.47$. This is consistent with the ΛCDM requirement that $w = -1$, lending no evidence to a form of dark energy different from that of a cosmological constant. While the constraint offered by the cluster-only analysis is not very stringent, it does illustrate the effectiveness of the cluster likelihood and hints towards the power of future cluster analyses. The constraint provided by the V10 sample does not rule out models with phantom dark energy equations of state and the best-fit value is well into the $w < -1$ domain. The asymmetry shown in the one-dimensional histogram, as presented in Figure 6–2, disfavours cosmologies without an accelerating expansion ($w > -1/3$) and, in particular, we find that $w < -0.26$ at 95% confidence. It is also apparent from the two dimensional confidence intervals that w displays some degeneracies with other parameters.

The next parameter to be examined is one to which the cluster likelihood has demonstrated great sensitivity: the normalization of the smoothed density field on $8h^{-1}$ Mpc scales, σ_8. The best-fit is $\sigma_8 = 0.745 \pm 0.083$ and is nearly identical to the constraint reported in the ΛCDM case: $\sigma_8 = 0.745 \pm 0.082$ (Table 5–1). The $\sigma_8 - w$ plane is enlarged and presented separately in Figure 6–3.

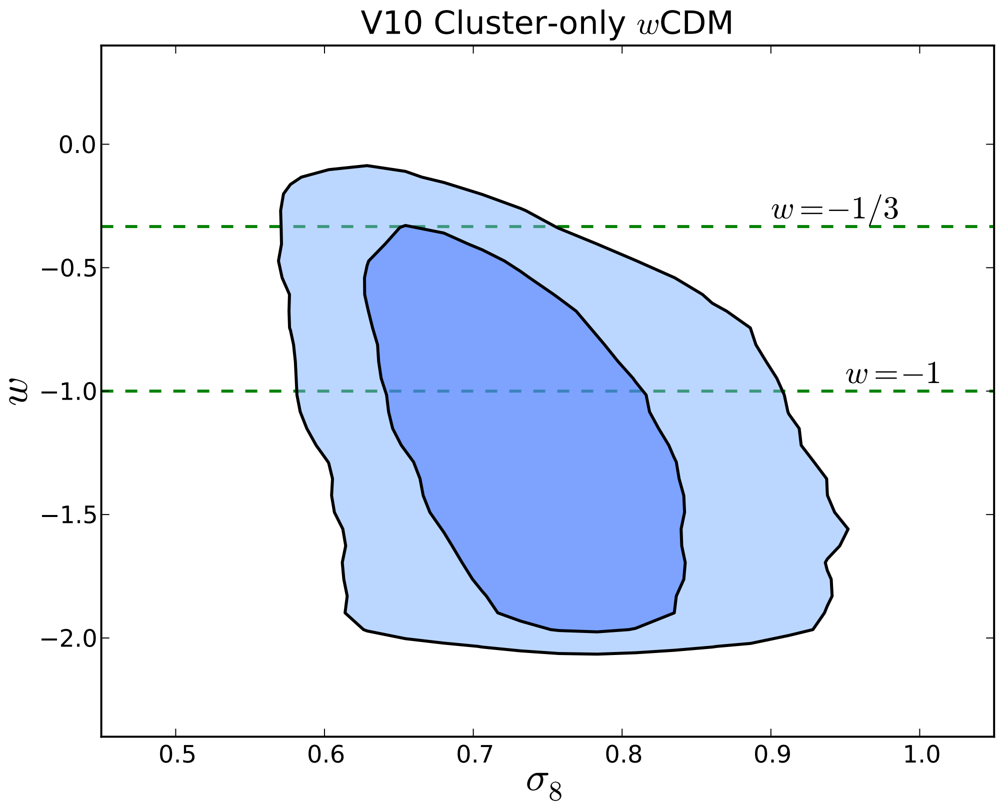

Figure 6–3: Two-dimensional 68% and 95% confidence intervals for the σ_8 and w parameters. This panel is an enlargement of the confidence intervals presented in Figure 6–2. Regions of increasingly negative w can be seen to correspond to increasing values of σ_8 with an opposite trend occurring for decreasing σ_8. An accelerating expansion corresponds to equations of state $w < -1/3$.

In Figure 6–3 we observe a weak degeneracy between σ_8 and w, whereby regions of increased σ_8 favour regions of increasingly negative w and vice versa. However, as noted above, this degeneracy does not noticeably increase the σ_8 uncertainty in the wCDM model. As summarized in the caption of Figure 6–1, for an otherwise similar cosmology, as w becomes more negative we expect σ_8, defined at z=0, to shift to larger values. Thus, when only considering the total cluster abundance, changes in w act in a manner similar to changes in σ_8; this behaviour is explored further in Figure 6–4.

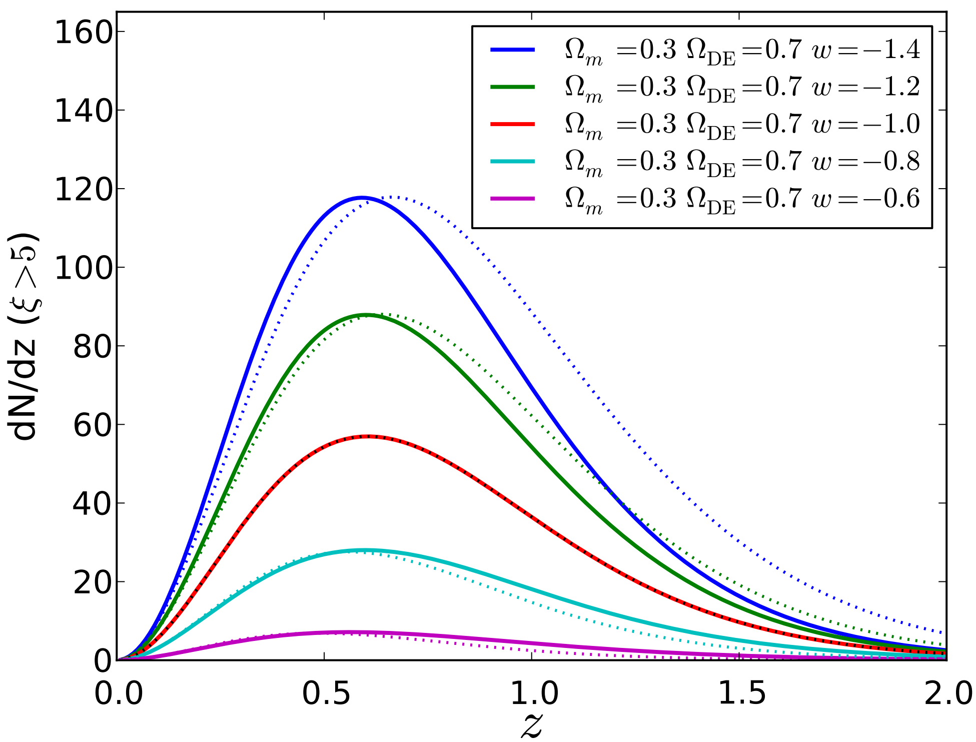

Figure 6–4: Differential cluster number counts as a function of redshift for a selection of cosmologies above an SZ-significance $\xi > 5$. Solid curves correspond to dark energy equations of state w = -0.6, -0.8, -1.0, -1.2, -1.4 from bottom to top respectively. For comparison, number counts for ΛCDM (w = -1) cosmologies with matching σ_8 values are presented as dotted curves. Values for σ_8 are σ_8 = 0.66, 0.74, 0.80, 0.84, 0.87 from bottom to top, for both the wCDM and ΛCDM models.

In Figure 6–4 the modifications to the abundance of structure as a function of redshift, due to changes in w, are demonstrated. At low redshift, the alteration to the volume element is apparent where, for a given value of Ω_{DE} and σ_8, less negative values of w result in a smaller volume element, thus decreasing the predicted cluster counts. At high redshift, the alteration to the growth function is apparent, where less negative values of w lead to a suppression of the growth rate and thus imply an excess of clusters at high redshift. For both effects an opposite behaviour is observed for increasingly negative values of w.

For small cluster catalogs, constraints are primarily from the integrated cluster abundance rather than its evolution with redshift. Figure 6–4 shows that it is, in principle, possible to isolate changes in w from changes in σ_8. To do so requires a sufficient sampling of the cluster mass function at redshifts where these differences are large. Such a sampling requires not only large catalogs (to overcome shot noise) but also a precise calibration between mass and the cluster observable.

Apart from its interactions with σ_8, the dark energy equation of state also affects two other key parameters. The first is the matter density Ω_m which also alters the rate of expansion and through it the growth of structure. The second parameter governs the redshift evolution in the scaling relation, C_{SZ}, which alters the predicted abundance of galaxy clusters as a function of redshift.

In terms of the matter density Ω_m, we see from Tables 5–1 and 6–1 that, when comparing the results for the ΛCDM model with those from the wCDM model, the best-fit value is largely unchanged while the uncertainty grows by nearly 10% when w is permitted to vary.

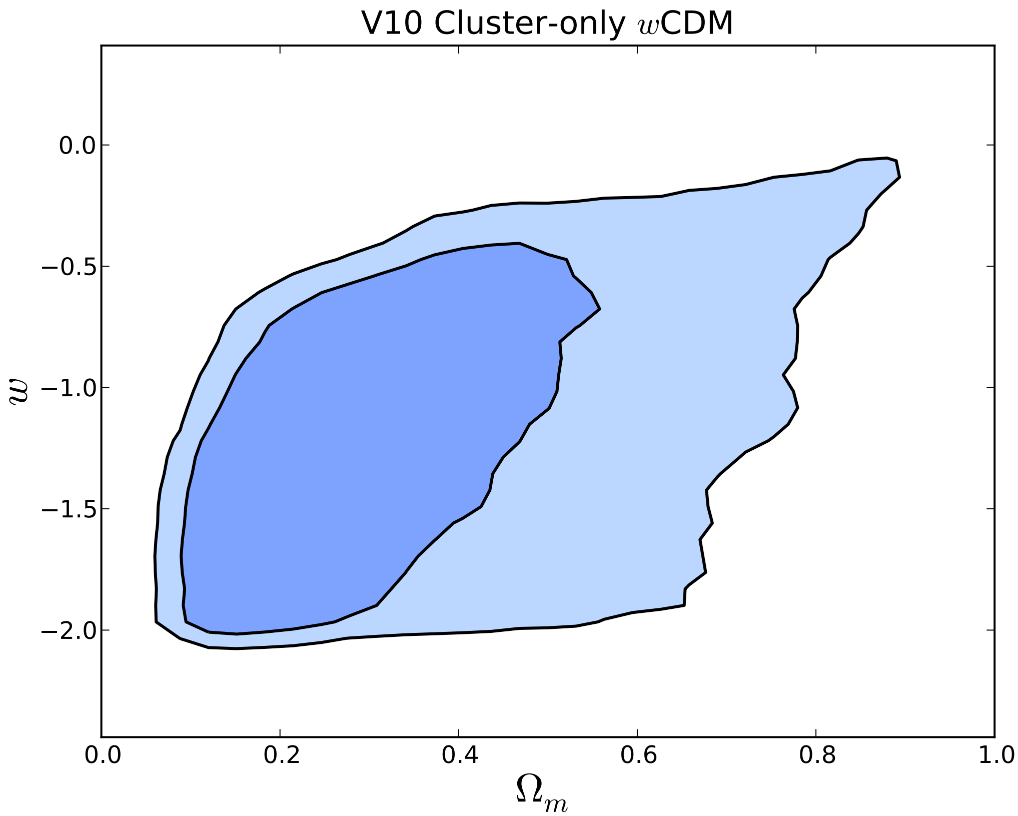

Figure 6–5: Two-dimensional 68% and 95% confidence intervals for the Ω_m and w parameters. This panel is an enlargement of the confidence intervals presented in Figure 6–2. Regions of decreased Ω_m are seen to favour more negative values of w and vice versa.

In Figure 6–5 we see that regions of increasingly negative w favour low matter densities with an opposite behaviour observed for large matter densities. This behaviour is qualitatively similar to that of the σ_8 parameter which, as shown in Figure 6–2, increases with decreased matter densities. The similarity between these two behaviours indicates that this interplay between Ω_m and w is due to their effects on the growth function, as presented in Figure 1–3. Large values of Ω_m are excluded in this figure by the lower limit of the top-hat prior placed on the Hubble constant (40 km s^{-1} Mpc$^{-1} < H_0 < 100$ km s^{-1} Mpc^{-1}) as $\Omega_m = (\Omega_c h^2 + \Omega_b h^2)/(H_0/100.0)^2$.

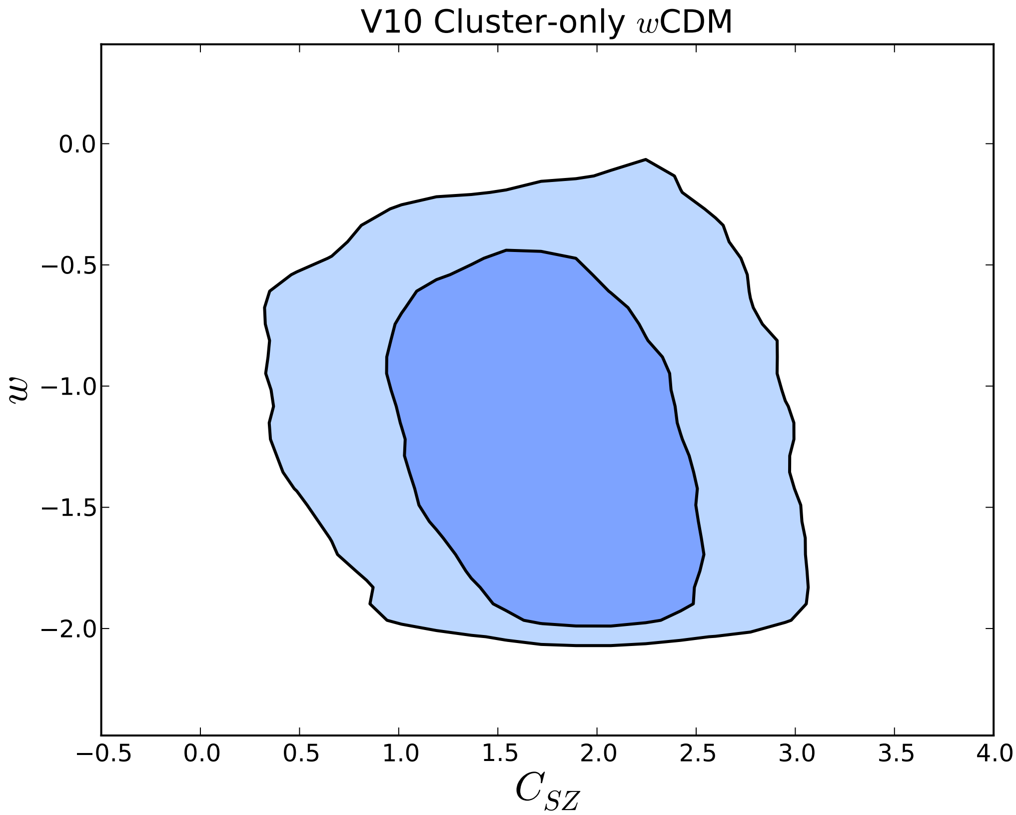

Figure 6–6: Two-dimensional 68% and 95% confidence intervals for the C_{SZ} and w parameters. This panel is an enlargement of the confidence intervals presented in Figure 6–2. More negative values of w tend towards regions of increased C_{SZ}.

The final parameter which we will examine (in terms of its interaction with the dark energy equation of state) is the parameter which defines the redshift evolution in the cluster scaling relation, C_{SZ}. For this parameter, when comparing to the ΛCDM case, the best-fit value is slightly higher, however, this deviation is well within the uncertainty, amounting to a shift of less than 0.2σ. The confidence contours for w and C_{SZ} are presented in Figure 6–6, where increasingly negative values of w are seen to slightly favour more positive values of C_{SZ} and vice versa.

6.4 Supplementary Data

In this section we will examine the constraints to the wCDM cosmological model due to the combination of external datasets and cluster data. This analysis will proceed in a manner very similar to that followed in Chapter 5 and will start with the addition of the WMAP7 dataset to the cluster likelihood. This is again accomplished within the CosmoMC framework, this time including the dark energy equation of state as a parameter in both the cluster and WMAP7 likelihoods. The results of this analysis are summarized in Table 6–2 and presented graphically in Figures 6–7 and 6–8.

From Table 6–2, we see that with the inclusion of the WMAP7 data we are able to relax some cosmological priors used by the cluster-only calculation as many parameters are well-constrained by the WMAP7 data. However, as the CMB is a probe of the high redshift universe ($z \sim 1100$), the WMAP7 data does not provide strong constraints on the dark energy equation of state, the effects of which have been shown to be most noticeable at late times. Unlike the cluster likelihood, which is sensitive to changes in the expansion rate through its effect on structure formation, the origin of the WMAP7 dark energy constraint is primarily geometric, measured through modifications to the distance to the last scattering surface. This constraint is strongly degenerate with the Hubble parameter, as evidenced by the strong degeneracy in the $H_0 - w$ confidence contours presented in Figure 6–7. This has the effect

Table 6–2: wCDM combined parameter constraints

Parameter	Cluster-only Fit	WMAP7 Fit	Cluster + WMAP7 Fit
Cosmological			
$\Omega_b h^2$	0.0231 ± 0.0072	0.0224 ± 0.0006	0.0225 ± 0.0006
$\Omega_c h^2$	0.108 ± 0.025	0.112 ± 0.006	0.109 ± 0.005
Ω_Λ	0.627 ± 0.197	0.734 ± 0.098	0.725 ± 0.088
$10^9 A_s$	2.390 ± 0.246	2.432 ± 0.123	2.389 ± 0.105
n_s	0.959 ± 0.036	0.966 ± 0.016	0.969 ± 0.014
τ	0.088[1]	0.088 ± 0.015	0.088 ± 0.015
w	-1.16 ± 0.47	-1.13 ± 0.40	-1.00 ± 0.30
Scaling Relation			
A_{SZ}	5.83 ± 1.79	6.01[†]	4.98 ± 1.55
B_{SZ}	1.43 ± 0.18	1.31[†]	1.47 ± 0.18
C_{SZ}	1.76 ± 0.58	1.60[†]	1.45 ± 0.47
D_{SZ}	0.209 ± 0.042	0.21[†]	0.208 ± 0.042
Derived			
H_0 (km/s/Mpc)	64.8 ± 15.7	74.7 ± 13.4	71.8 ± 11.0
σ_8	0.745 ± 0.083	0.846 ± 0.132	0.799 ± 0.092
Ω_m	0.373 ± 0.197	0.266 ± 0.098	0.275 ± 0.088

[1] fixed to fiducial value

[†] Fiducial V10 scaling relation: $A_{SZ} = 6.01 \pm 1.80$, $B_{SZ} = 1.31 \pm 0.26$, $C_{SZ} = 1.60 \pm 0.80$, $D_{SZ} = 0.21 \pm 0.04$

of significantly degrading the WMAP7 H_0 constraint, reported as $H_0 = 70.1 \pm 2.5$ km/s/Mpc in the ΛCDM case and $H_0 = 74.7 \pm 13.4$ km/s/Mpc here. We will return to this increased uncertainty when discussing other datasets later in this section.

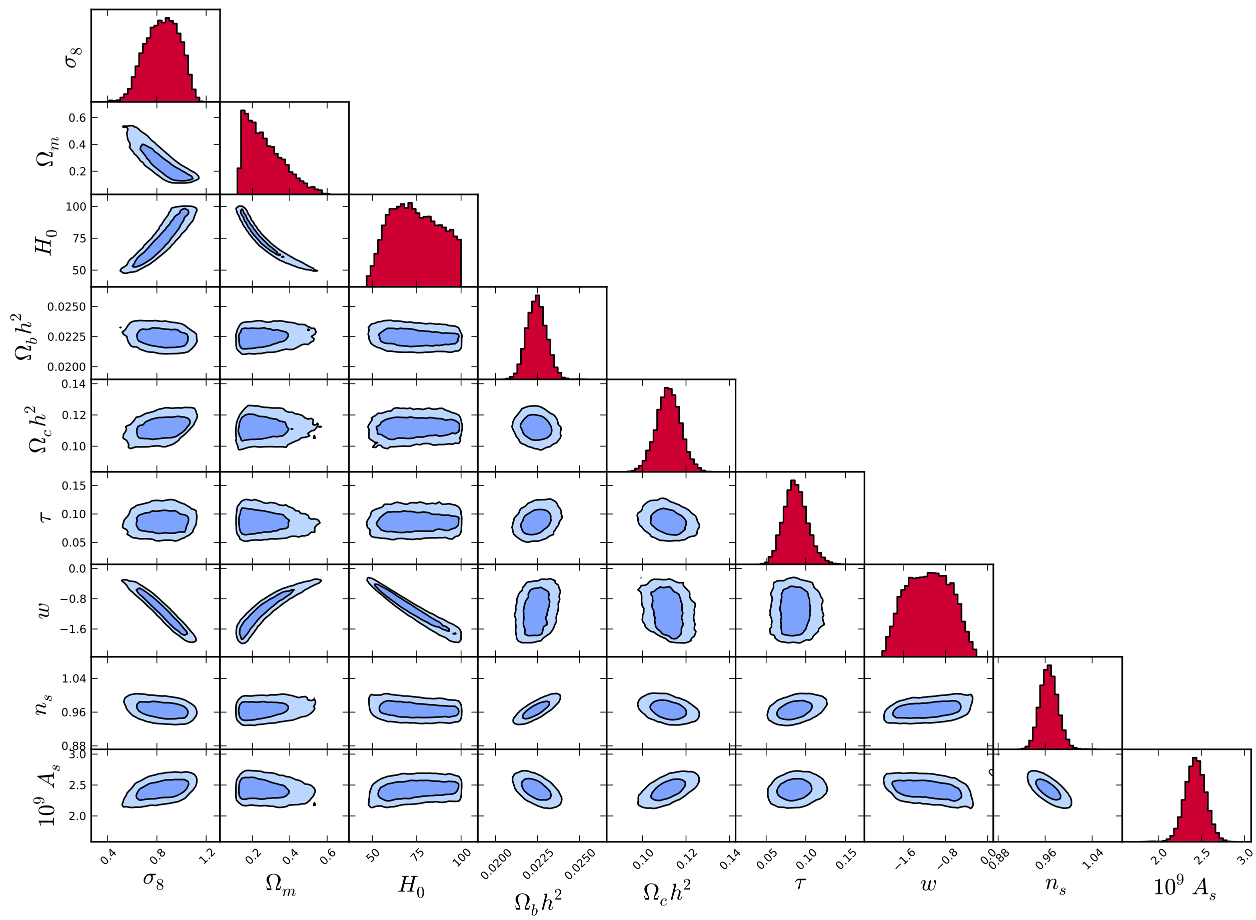

Figure 6–7: wCDM parameter grid displaying the 68% and 95% confidence contours for the WMAP7 dataset. Also shown are the marginalized, one-dimensional histograms.

In the initial cluster-only analysis we found that the V10 cluster sample constrained the dark energy equation of state to $w = -1.16 \pm 0.47$. As shown in Table

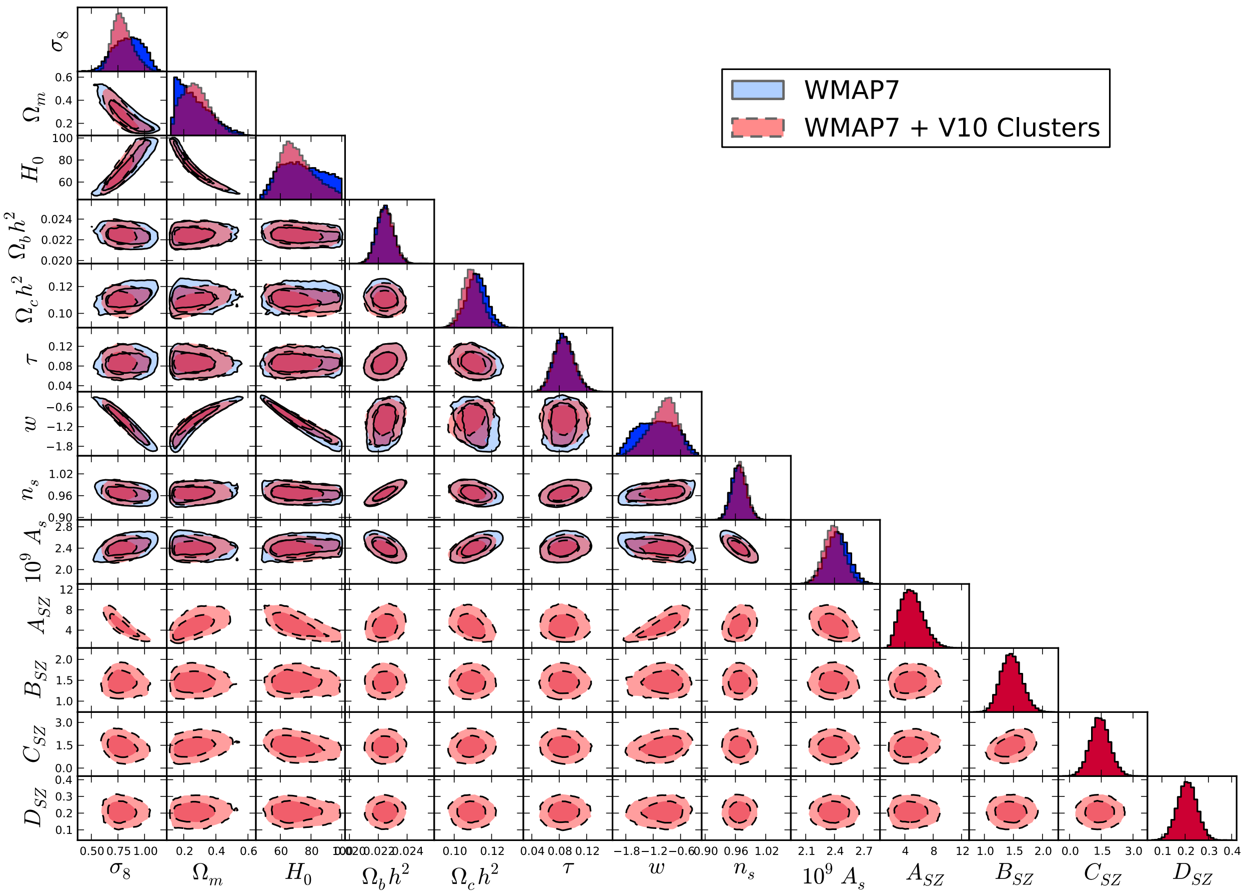

Figure 6–8: wCDM parameter grid displaying the 68% and 95% confidence confidence contours for the WMAP7 dataset as well as the combined WMAP7 and cluster dataset. Also shown are the marginalized, one-dimensional histograms. The added cluster data is shown to modestly improve constraints on some parameters.

6–2, the WMAP7 constraints to this parameter are similar, finding $w = -1.13 \pm 0.40$ which, as with the cluster-only case, is entirely consistent with a cosmological constant while again indicating a very weak preference for $w < -1$. From the combination of the two datasets a joint constraint may be formed, as shown in Table 6–2, where we find $w = -1.00 \pm 0.30$. This constraint is again consistent with a cosmological constant and displays a 25% reduction in its WMAP7-based uncertainty with the inclusion of the cluster data. This constraint can also be directly compared with that reported by the Atacama Cosmology Telescope (ACT) which, in a technique very similar to that presented in this work, found $w = -1.14 \pm 0.35$ for the combination of their SZ-selected cluster sample and the WMAP7 dataset [177]. Thus, we find that through the inclusion of late-time cluster data we are able to significantly decrease the uncertainty of the dark energy equation of state constraint offered by CMB data alone.

Further examination of Figure 6–8 also reveals a significant improvement to the constraint on the cluster-scale amplitude parameter σ_8, with the combination of WMAP7 and cluster data. Here the cluster data provides a roughly 30% reduction in the WMAP7-derived uncertainty on this parameter, improving the best-fit from $\sigma_8 = 0.846 \pm 0.132$ to $\sigma_8 = 0.799 \pm 0.092$ when the cluster data is added to the WMAP7 result. For the CMB data, the σ_8 parameter is strongly degenerate with w. As such, improved σ_8 constraints, due to the use of cluster data, translate into constraints on w, as shown in Figure 6–9. Thus, the reduction in permitted σ_8 parameter space, due to the addition of galaxy cluster data, leads to improved constraints. The addition of cluster data also improves the constraints on both the H_0 and Ω_m parameters, which display reductions of approximately 18% and 10% in their respective uncertainties (Table 6–2).

As previously mentioned, the inclusion of w to the cosmological parameter space results in a significant degradation of the Hubble parameter constraint in the

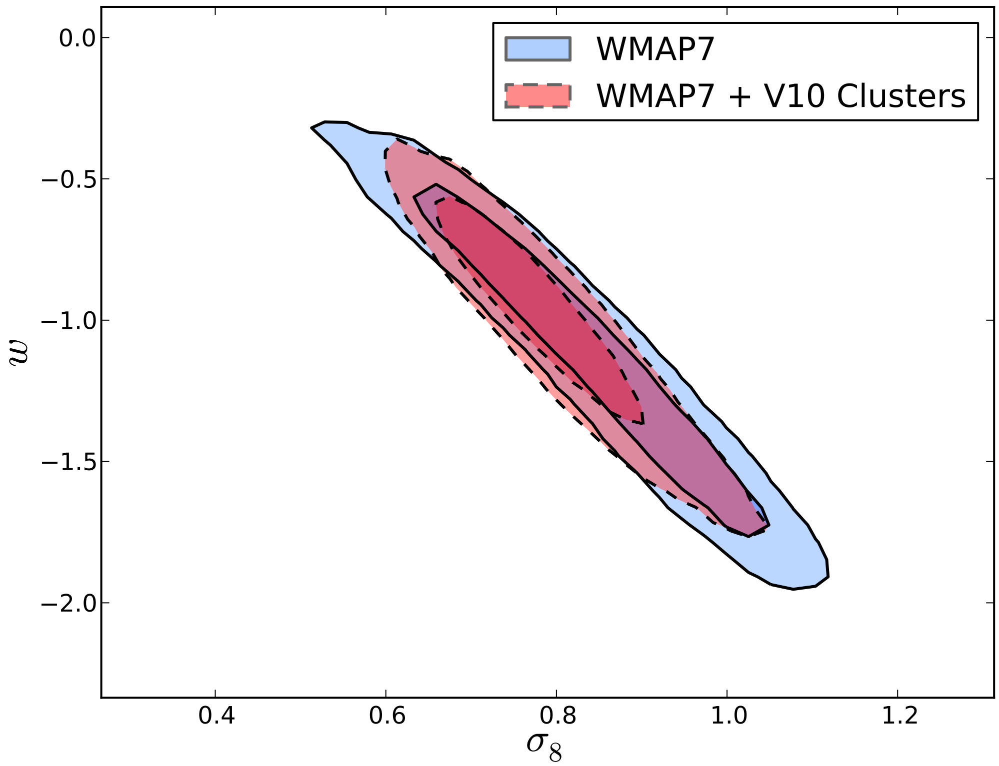

Figure 6–9: Two-dimensional 68% and 95% confidence intervals for the σ_8 and w parameters. Intervals are presented for the WMAP7 dataset both with and without galaxy cluster data. This panel is an enlargement of the confidence intervals presented in Figure 6–8. The improvement to the constraints due to the inclusion of cluster data is clear.

WMAP7 analysis. However, there exist independent measurements of the Hubble constant. As the Hubble parameter is a measure of the local expansion rate, it can be calibrated through the measurement of both the redshift (recessional velocity) and distance to cosmic structures. In practice, the distance determination proves difficult and requires objects of known luminosities, so called *standardizable candles*, such as

Table 6–3: wCDM + HST combined parameter constraints

Parameter	Cluster + HST Fit	WMAP7 + HST Fit	Cluster + WMAP7 + HST Fit
Cosmological			
$\Omega_b h^2$	0.0236 ± 0.0071	0.0225 ± 0.0006	0.0225 ± 0.0006
$\Omega_c h^2$	0.110 ± 0.031	0.112 ± 0.006	0.109 ± 0.005
Ω_Λ	0.756 ± 0.072	0.755 ± 0.027	0.756 ± 0.028
$10^9 A_s$	2.383 ± 0.237	2.439 ± 0.116	2.385 ± 0.105
n_s	0.958 ± 0.036	0.966 ± 0.014	0.968 ± 0.014
τ	0.088[1]	0.088 ± 0.015	0.088 ± 0.015
w	-1.21 ± 0.46	-1.14 ± 0.14	-1.07 ± 0.12
Scaling Relation			
A_{SZ}	5.83 ± 1.76	6.01†	4.65 ± 1.18
B_{SZ}	1.44 ± 0.19	1.31†	1.47 ± 0.18
C_{SZ}	1.52 ± 0.53	1.60†	1.38 ± 0.45
D_{SZ}	0.211 ± 0.042	0.21†	0.208 ± 0.042
Derived			
H_0 (km/s/Mpc)	74.5 ± 3.8	74.4 ± 3.8	73.7 ± 3.8
σ_8	0.778 ± 0.066	0.856 ± 0.061	0.817 ± 0.050
Ω_m	0.244 ± 0.072	0.245 ± 0.027	0.244 ± 0.028

[1] fixed to fiducial value
† Fiducial V10 scaling relation: $A_{SZ} = 6.01 \pm 1.80$, $B_{SZ} = 1.31 \pm 0.26$, $C_{SZ} = 1.60 \pm 0.80$, $D_{SZ} = 0.21 \pm 0.04$

Type 1a supernovae or Cepheid variables [178, 179, 180]. By calculating distances and redshifts for a large number of these objects it is possible to observationally determine a value for the Hubble parameter. Such surveys have been performed with the Hubble Space Telescope (HST), with results presented in Riess et al. [178] and Riess et al. [179]. This constraint takes the form of a Gaussian prior on the physical angular diameter distance to an effective redshift: $D_A^{-1}(z_{\text{eff}} = 0.04) = 6.49 \times 10^{-3} \pm 3.15 \times 10^{-4}$ Mpc^{-1} [179]. With this data, a direct, observational constraint for the Hubble parameter is included, the results of which are presented in Table 6–3 and Figure 6–10.

The primary aim in adding the observational HST constraint lies in attempting to reduce the degeneracy between H_0 and w in the WMAP7 data and to improve constraints to parameters which are degenerate with the Hubble parameter. These improved constraints are evident when comparing the confidence intervals presented in Figure 6–8 with those in 6–10.

The most obvious effect of this added data is a significant reduction in the uncertainty on the Hubble parameter H_0. For the joint WMAP7-clusters case, the addition of the HST constraint reduces the uncertainty on H_0 from $\sigma_{H_0} = 11.0$ to $\sigma_{H_0} = 3.8$ km/s/Mpc, a nearly three-fold improvement. The constraint to the matter density Ω_m is also improved by the HST data, decreasing the uncertainty by roughly a factor of three in the combined fit. For σ_8, the uncertainty is nearly halved when comparing the combined fits, improving from $\sigma_8 = 0.799 \pm 0.092$ to $\sigma_8 = 0.817 \pm 0.050$ with the addition of HST data.

Finally, we can compare the dark energy equation of state constraint reported in Tables 6–2 and 6–3. For the clusters alone, there is negligible improvement in the constraint when the HST data is added, changing from $w = -1.16 \pm 0.47$ to $w = -1.21 \pm 0.46$ with the addition of the HST data. This indicates that the growth-based cluster constraint on w is not strongly dependent upon the Hubble parameter. For the WMAP7 data, the w constraint is strongly degenerate with H_0 and thus the addition of the HST constraint has a profound effect upon the parameter uncertainty. With the addition of HST data the WMAP7 constraint shifts from $w = -1.13 \pm 0.40$ to $w = -1.14 \pm 0.14$, reducing the uncertainty on w by more than 60%. When clusters are included with the WMAP7 and HST data, the joint constraint improves

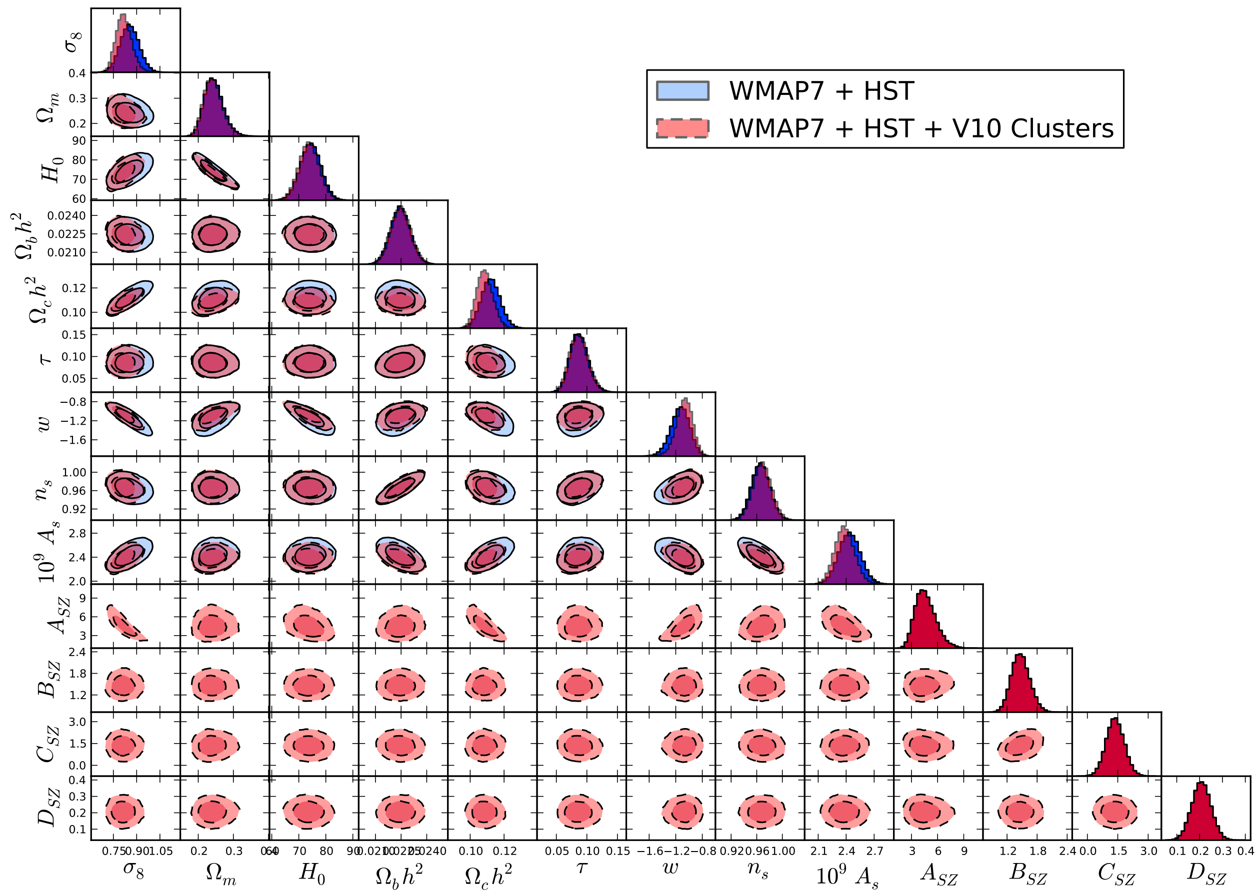

Figure 6–10: wCDM parameter grid displaying the 68% and 95% confidence contours for the combined WMAP7 and HST dataset as well as the combined WMAP7, HST and V10 cluster dataset. Also shown are the marginalized, one-dimensional histograms. The cluster data is shown to provide modest improvements to some parameters.

to $w = -1.07 \pm 0.12$, indicating a reduction in the uncertainty of nearly 15% due to the addition of cluster data. The improvement to the joint constraint from the addition of HST data is presented in Figure 6–11.

This result may also be compared with those derived from other datasets, as presented in the WMAP seven-year cosmological analysis [11]. In Komatsu et al. [11], the combination of the WMAP7 data, the HST constraint, and baryon acoustic oscillation data (BAO) [15] results in a constraint on the dark energy equation of state of $w = -1.10 \pm 0.14$. When we include WMAP7 data, the HST constraint, and supernova observations [16] we find $w = -1.03 \pm 0.08$. Thus, while the cluster data only offers a 15% improvement to the joint WMAP-HST constraint, the resulting fit is consistent and competitive with those derived from other local datasets.

A significant source of uncertainty in the cluster likelihood method rests in the scaling between the cluster observable and its mass. It is possible to reduce this uncertainty through the use of complementary cluster observables. As an approximate forecast of such methods we recalculated the combined WMAP7-HST-cluster fit for a scenario in which the Gaussian prior on the mass-significance normalization (A_{SZ}) is reduced from 30% to 10% about its central value. The result of this forecast, $w = -1.00 \pm 0.09$, indicates that improved calibration of the cluster scaling relation provides significant reductions to the uncertainty on w. Future galaxy cluster surveys are likely to improve upon this forecast constraint as they will also include greatly expanded galaxy cluster catalogs.

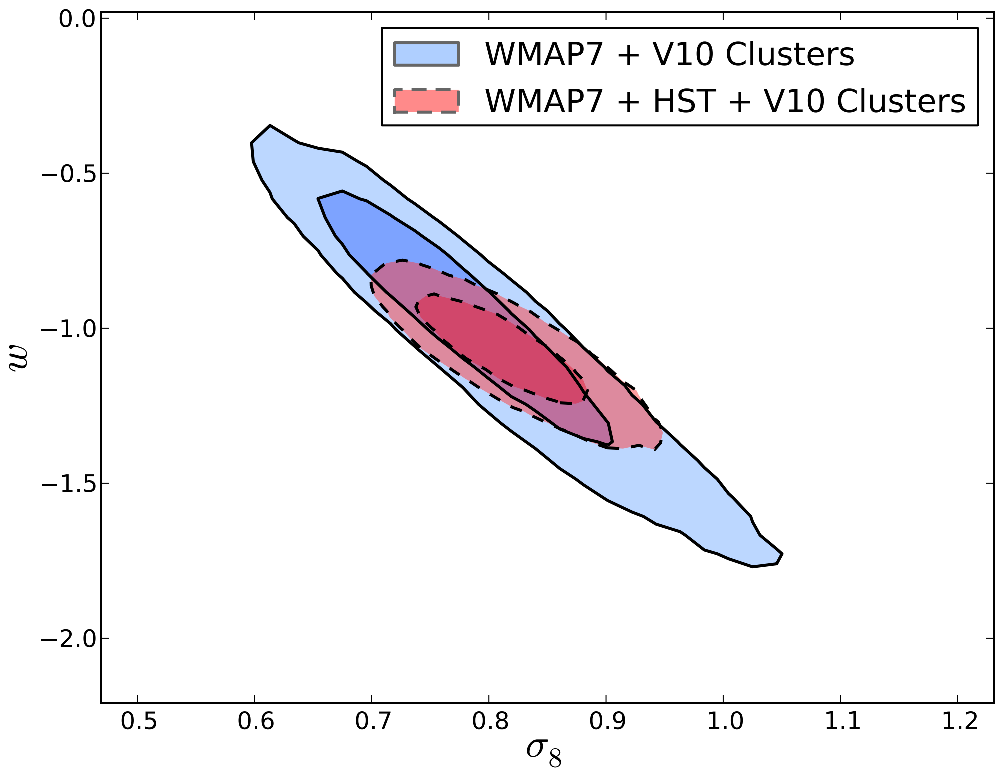

Figure 6–11: Two-dimensional 68% and 95% confidence intervals for the σ_8 and w parameters. Intervals are presented for the WMAP7 and cluster dataset both with and without the HST constraint.

CHAPTER 7
Non-Gaussian ΛCDM

7.1 Introduction

In Section 1.4, we indicated that simple inflationary models predict that quantum fluctuations in the inflationary scalar field will lead to a Gaussian spectrum of primordial density perturbations. From these predictions we are able to calculate a variety of cosmological quantities, including the CMB temperature power spectrum and, as shown in Chapter 2, the predicted abundances of collapsed objects in the universe.

To date, these forecasted quantities have been in excellent agreement with the generic predictions from these inflationary models. Among these observations is the CMB temperature angular power spectrum, measured to great precision by the WMAP experiment and presented in Figure 5–5 [18, 11]. Both the Gaussianity and near scale-invariance of the primordial perturbations are strongly supported and the observed CMB spectra are in excellent agreement with the predictions of inflationary models, with measurements of the CMB bispectrum finding $f_{NL} = 32 \pm 21$ at 68% confidence [181, 182, 65].

However, in recent years the discovery of high-redshift, massive galaxy clusters has led to speculation that the standard Gaussian, ΛCDM model may be incorrect [98, 96, 23, 24, 97]. In this chapter we will investigate this tension through the analysis of the SPT cluster sample. This analysis will be based upon the W11 galaxy cluster catalog, introduced in Section 3.6, which represents the largest statistically complete sample of the most massive clusters in the universe.

7.2 Non-Gaussian Cluster Likelihood

In Section 2.4, three separate methods for calculating the non-Gaussian mass function were presented. For each of these scenarios, the non-Gaussian mass function was modeled as a correction to a well-calibrated Gaussian mass function. Owing to the complexity in formulating the non-Gaussian mass function, each of these three methods employed a number of approximations, the details and limitations of which will be reviewed here.

The three mass functions examined in this section are the LVS, PGH and DHS methodologies, defined in Section 2.4 and presented in LoVerde and Smith [62], Paranjape et al. [95], and Dalal et al. [58] respectively. These non-Gaussian mass functions were parameterized through the non-Gaussianity parameter f_{NL}, as defined in Equation 1.70. The effect of this term is generally described in relation to either an increase or decrease in abundance of cosmic structure, depending upon the sign of f_{NL}. In order to compare these three non-Gaussian forms of the mass function, we will compute their predictions for the ratio of the non-Gaussian to Gaussian mass function for a variety of f_{NL} values. These ratios have been computed for all three formulations for various values of f_{NL} and are presented in Figures 7–1 and 7–2.

In Figure 7–1, the non-Gaussian ratios are presented as functions of both redshift and f_{NL} for the three mass functions in question. In all cases the effect of positive f_{NL} can be seen to result in the increased abundance of halos, in particular at high mass and redshift. This figure shows reasonably good agreement between the LVS

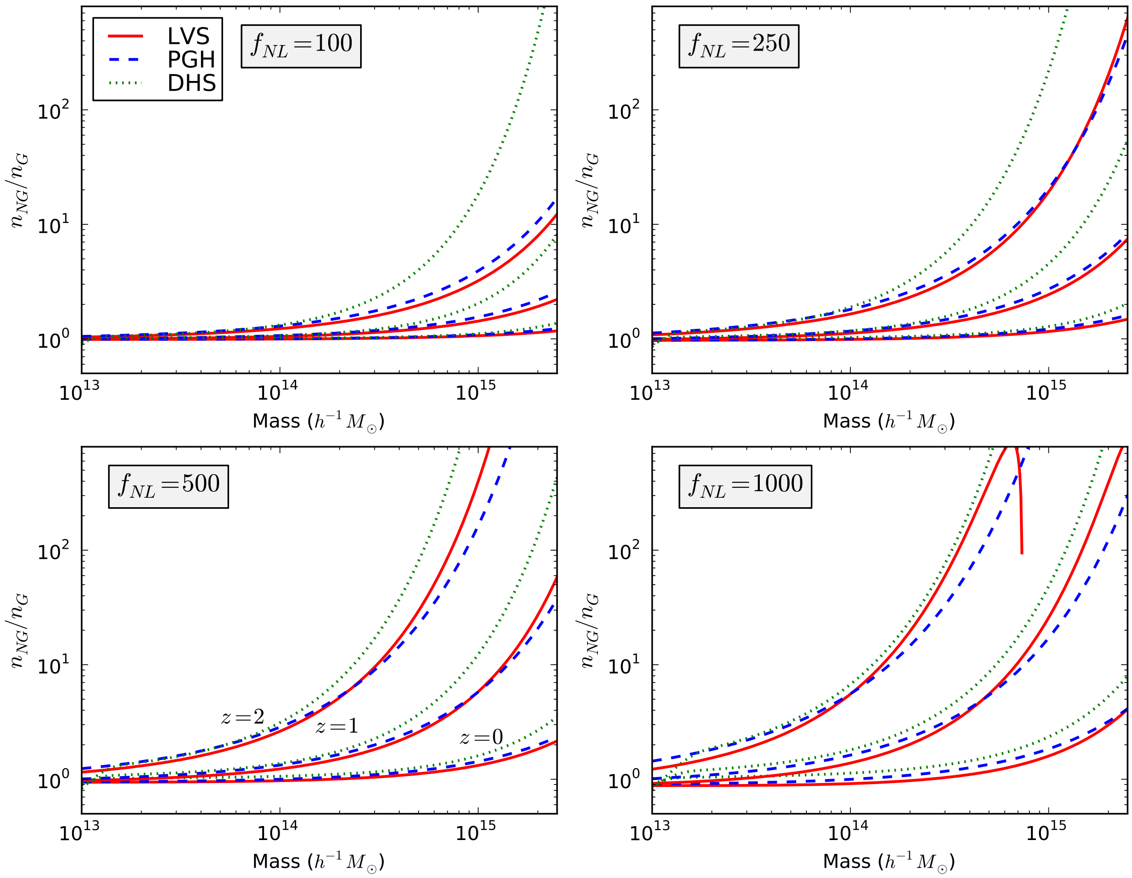

Figure 7–1: Non-Gaussian mass function ratios are presented for the LVS, PGH and DHS methodologies. Ratios have been evaluated for z=0, 1, and 2 for values of f_{NL} ranging from +100 to +1000. Reasonable agreement is observed between the LVS and PGH analytic formulations while the DHS method predicts increased abundances at most masses. Evident in the f_{NL}=1000 panel is the instability of the LVS function for combinations of large f_{NL} and mass.

and PGH mass functions across most of the mass range. For large values of mass and f_{NL}, the two functions begin to disagree, with instabilities arising in the LVS formulation. The qualitative agreement between these two functions suggests that the approximations used in both derivations are reasonable. In the limit of these approximations being exact, the two functions should be equivalent. Finally, it is noted in LoVerde and Smith [62] that they find very good agreement between the LVS non-Gaussian mass function and N-body simulations for $|f_{NL}| \leq 500$.

Also shown in Figure 7–1 is the DHS mass function ratio which appears to follow the same general form as the other two, but predicts increased abundances of halos across nearly the entire mass range. This discrepancy may be partially related to the $\lesssim 15\%$ error associated with relating M_{FOF} to M_{200} for the DHS mass function, however, as demonstrated in Section 2.4, this uncertainty is not expected to significantly alter the predictions of the DHS mass function. The agreement between the DHS and analytic non-Gaussian ratios also appears to vary as a function of f_{NL}. The DHS mass function is measured in Dalal et al. [58] to agree with the simulations with which it was calibrated to within $\sim 10\%$. They also note that their simulations, and non-Gaussian mass function, disagree significantly with the PS-based non-Gaussian mass function formulation upon which both the PGH and LVS functions are based. Thus, while both the DHS and LVS non-Gaussian mass functions appear to agree well with the N-body simulations against which they were tested, we find significant differences between the predictions of these two formulations. Once again, the origin of this uncertainty is not evident and it is unclear which method offers the more accurate prediction.

For the f_{NL}=1000 case, represented in the bottom right panel of Figure 7–1, the LVS mass function displays a significant instability, indicating that, for extremely large values of f_{NL} and mass, the truncation applied in the LVS derivation is insufficient. In this f_{NL}=1000 panel, we observe similar behaviour for all three mass functions at low to intermediate masses. At high mass, however, the LVS function appears to reach a turnaround and eventually becomes undefined. This unphysical behaviour is a result of the truncation in the Edgeworth series and is not shared by the resummed PGH function. This limitation of the LVS non-Gaussian mass function will be examined further when discussing the cluster likelihood implementation later in this Section.

The non-Gaussian mass functions were also calculated for negative values of f_{NL}, the results of which are presented in Figure 7–2. In these scenarios increasingly negative values of f_{NL} suppress structure formation, significantly decreasing the abundance of collapsed objects, again at high mass and redshift in particular. As in the positive f_{NL} case, the analytic LVS and PGH functions show reasonable agreement, particularly for f_{NL}=-500 where they appear to be nearly equivalent. This agreement is notable in light of the ad hoc prescription employed by the PGH method for negative values of f_{NL} (Equation 2.41). As with positive f_{NL} these functions disagree significantly for large negative f_{NL}, however, both functions appear to remain stable in this regime.

The DHS mass function again appears to follow the same general form as the other non-Gaussian mass functions and, in particular, shows reasonable agreement for small values of negative f_{NL}. For more negative values it predicts an increased suppression of the cluster abundance, when compared with both the LVS and PGH forms. As in the positive f_{NL} case, the origin of this behaviour is unclear and there is no evidence indicating whether the source of this discrepancy lies in either the simulation-calibrated or analytic forms. Finally, unlike at positive f_{NL}, all functions appear stable at negative values, with their respective non-Gaussian ratios all tending towards zero at large mass and f_{NL}.

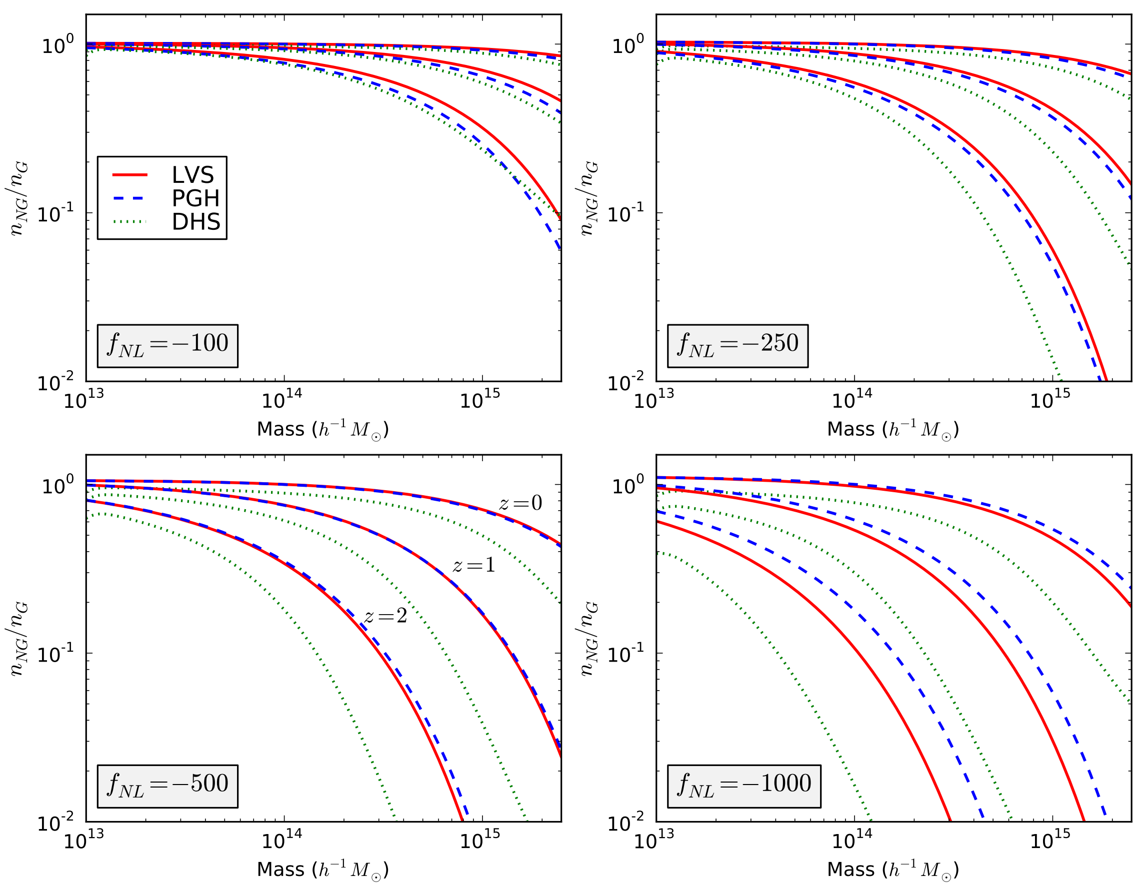

Figure 7–2: Non-Gaussian mass function ratios are presented for the LVS, PGH and DHS methodologies. Here ratios have again been calculated for three redshifts for values of f_{NL} ranging from -100 to -1000. Reasonable agreement is again observed between the LVS and PGH analytic formulations with the DHS method now predicting decreased abundances at most masses.

For the analysis presented in this work, the cluster abundances are expressed in terms of the SZ significance ξ and the cluster redshift z. As discussed in Section 4.3, ξ is related to the cluster mass through the scaling relations presented in Equations 4.5 and 4.4. For the W11 catalog, the priors which define the scaling relation parameters are presented in Table 4–1. As mentioned in V10 and W11, these priors were chosen to conservatively encompass the uncertainty associated with fitting the scaling relation parameters to simulated clusters and pressure profiles.

In particular, the 30% uncertainty associated with the scaling relation normalization A_{SZ} corresponds to a $\sim 20\%$ uncertainty in the cluster mass for the fiducial relation. As the origins of the differences between the analytic and simulation-calibrated non-Gaussian mass function predictions are not well-understood, the uncertainties associated with the non-Gaussian formulation will be described in terms of the existing scaling relation priors. This should not significantly affect the focus of our analysis, which is to constrain deviations from $f_{NL} = 0$, where the non-Gaussian mass functions are defined to reproduce the Gaussian mass function.

Having compared the differing procedures for formulating non-Gaussian mass functions we are now tasked with incorporating these functions into the cluster likelihood evaluation. In order to provide useful results from the MCMC method, it must be possible to sample the likelihood surface across a wide range of parameter values. The large-f_{NL} instabilities displayed by the LVS mass function are problematic, as we would need to explicitly place a prior which would restrict these unstable regions of parameter space. Such a prior would, in principle, depend not only upon cluster mass and redshift but also the cosmological parameters which we are attempting to constrain. Due to these limitations, the LVS non-Gaussian mass function will not be included in our cosmological analysis.

The LVS formulation, however, does act as an important and useful comparison for the PGH non-Gaussian mass function. As both functions were derived using similar analytic techniques, the general agreement between the two functions, as shown in Figures 7–1 and 7–2, lends some validation to the assumptions applied in both derivations. Important among these are the high-mass and high-f_{NL} stability in the resumming technique and the ad-hoc definition of the PGH non-Gaussian mass function at negative f_{NL}. Comparison between these two functions also indicates that there exists uncertainties in the non-Gaussian mass function formulation as, even for small f_{NL}, there appear to be noticeable discrepancies between the two formulations. The origin and magnitude of these uncertainties are not known. Thus, while not employed for the purposes of parameter estimation, the LVS mass function provides a useful point of comparison for the PGH mass function and an indication of the uncertainty associated with the non-Gaussian mass function formulation.

For the PGH and DHS non-Gaussian mass functions there do not appear to be any significant instabilities across the relevant parameter space. Thus both the PGH and DHS non-Gaussian mass functions are suitable for inclusion in the cluster likelihood analysis. By studying both formulations we are able to compare the predictions and constraints from both the analytic and simulation-derived non-Gaussian methods. While the two methods have been shown to disagree in their predictions for the non-Gaussian modification to the cluster abundance, they are both defined to reproduce the standard, Gaussian mass function for $f_{NL} = 0$ and, as such, can each provide evidence for deviations from that fiducial point.

Incorporation of these functions into the cluster analysis will prove to be reasonably straightforward, but will require one important assumption concerning the nature of the non-Gaussianity, as will be described below. First we must consider the extra free parameters required by the non-Gaussian mass functions. Fortunately, for both methods, this amounts to adding a single extra parameter, specifically the non-Gaussianity parameter f_{NL}, which can be included as an additional MCMC variable. The observed stability of the two mass functions with regards to this parameter indicates that we may explore a large region in f_{NL} parameter space which, for computational purposes, will be bounded by a simple, top-hat prior extending from $f_{NL} = -2000$ to $f_{NL} = +2000$.

With f_{NL} included as an additional MCMC parameter, we can then, as detailed in the cluster likelihood evaluation outlined in Section 4.2, replace the Gaussian Tinker mass function with its non-Gaussian counterpart, as defined in Equations 2.39 and 2.42. Through these modifications to the cluster likelihood, we are able to predict the correction to the abundance of galaxy clusters in the universe as a function of f_{NL} and, through comparison with a catalog of observed clusters, constrain the observed level of non-Gaussianity in our universe.

While the local form of primordial non-Gaussianity, as given in Equation 1.70, has been shown to alter late-time abundances of cosmic structure it is also responsible for other cosmological signatures. In particular, it is well-established that such primordial non-Gaussianity would produce a measurable bispectrum in the CMB temperature anisotropy, a quantity which is not predicted in the presence of purely Gaussian fluctuations [68, 43, 61, 182]. The presence of such a feature has been investigated by the WMAP experiment, the results of which are presented in Komatsu [65] and Komatsu et al. [182] and are shown to constrain the degree of observed non-Gaussianity to $f_{NL} = 32 \pm 21$ at 68% confidence.

In this work we are chiefly interested in obtaining evidence for non-Gaussianity as provided by galaxy cluster abundances in the late-time universe. Furthermore, there exists a large difference in physical scale between the CMB and clusters, the former constraining scales much larger ($k \sim 0.03$ Mpc^{-1}) than the latter ($k \sim 0.2$ Mpc^{-1}). Thus, while we will still incorporate the CMB constraints for the base cosmological parameters, we will isolate the effects of primordial non-Gaussianity to the cluster likelihood alone, utilizing only the CMB power spectrum, and disregarding the constraints offered by the CMB bispectrum. This approach allows us to better isolate evidence for deviations from the Gaussian cosmological model to the late-time abundance of galaxy clusters.

7.3 Analysis and Results

For this analysis we will employ the W11 catalog, introduced and described in Section 3.6. Through this purposeful selection of the most massive galaxy clusters over a large area, we aim to constrain deviations from Gaussianity in the high-mass and redshift regime where such deviations have been shown to be large (Figures 7–1 and 7–2). The order of this analysis will deviate somewhat from the pattern established in Chapters 5 and 6, where constraints were examined for the cluster

Table 7–1: Cluster and WMAP7 non-Gaussianity parameter constraints

Parameter	WMAP7+V10 $f_{NL} \equiv 0$	WMAP7+W11 PGH f_{NL}	WMAP7+W11 DHS f_{NL}
Cosmological			
$\Omega_b h^2$	0.0225 ± 0.0006	0.0225 ± 0.0006	0.0225 ± 0.0006
$\Omega_c h^2$	0.1085 ± 0.0049	0.1093 ± 0.0050	0.1094 ± 0.0055
Ω_Λ	0.741 ± 0.025	0.737 ± 0.025	0.737 ± 0.028
$10^9 A_s$	2.385 ± 0.106	2.396 ± 0.105	2.395 ± 0.109
n_s	0.969 ± 0.014	0.968 ± 0.014	0.967 ± 0.014
τ	0.088 ± 0.015	0.088 ± 0.015	0.088 ± 0.015
f_{NL}	$0.0^\dagger$	-340 ± 831	-43 ± 508
Scaling Relation (W11)			
A_{SZ}	—	3.05 ± 1.02	2.90 ± 1.12
B_{SZ}	—	1.57 ± 0.18	1.53 ± 0.21
C_{SZ}	—	0.94 ± 0.38	0.89 ± 0.39
D_{SZ}	—	0.160 ± 0.029	0.169 ± 0.030
Scaling Relation (V10)			
A_{SZ}	4.92 ± 1.00	—	—
B_{SZ}	1.48 ± 0.18	—	—
C_{SZ}	1.40 ± 0.45	—	—
D_{SZ}	0.209 ± 0.042	—	—
Derived			
H_0 (km/s/Mpc)	71.28 ± 2.30	71.02 ± 2.30	71.02 ± 2.47
σ_8	0.796 ± 0.026	0.800 ± 0.027	0.801 ± 0.031
Ω_m	0.259 ± 0.025	0.263 ± 0.025	0.263 ± 0.028

† fixed to fiducial value
Fiducial W11 scaling relation: $A_{SZ} = 3.51 \pm 1.05$, $B_{SZ} = 1.30 \pm 0.26$, $C_{SZ} = 0.85 \pm 0.42$, $D_{SZ} = 0.16 \pm 0.03$
Fiducial V10 scaling relation: $A_{SZ} = 6.01 \pm 1.80$, $B_{SZ} = 1.31 \pm 0.26$, $C_{SZ} = 1.60 \pm 0.80$, $D_{SZ} = 0.21 \pm 0.04$

likelihood both with and without supplementary datasets, in that here we will immediately include the WMAP7 likelihood. The results of the cluster and WMAP7 non-Gaussianity analysis are presented in Table 7–1 with confidence contours presented in Figure 7–3.

In terms of the standard (non-f_{NL}) cosmological parameters, Table 7–1 shows no significant changes between the Gaussian and non-Gaussian parameter fits. For the scaling relation parameters, comparison with the Gaussian case is somewhat difficult, due to the differences between the V10 and W11 scaling relation parameter

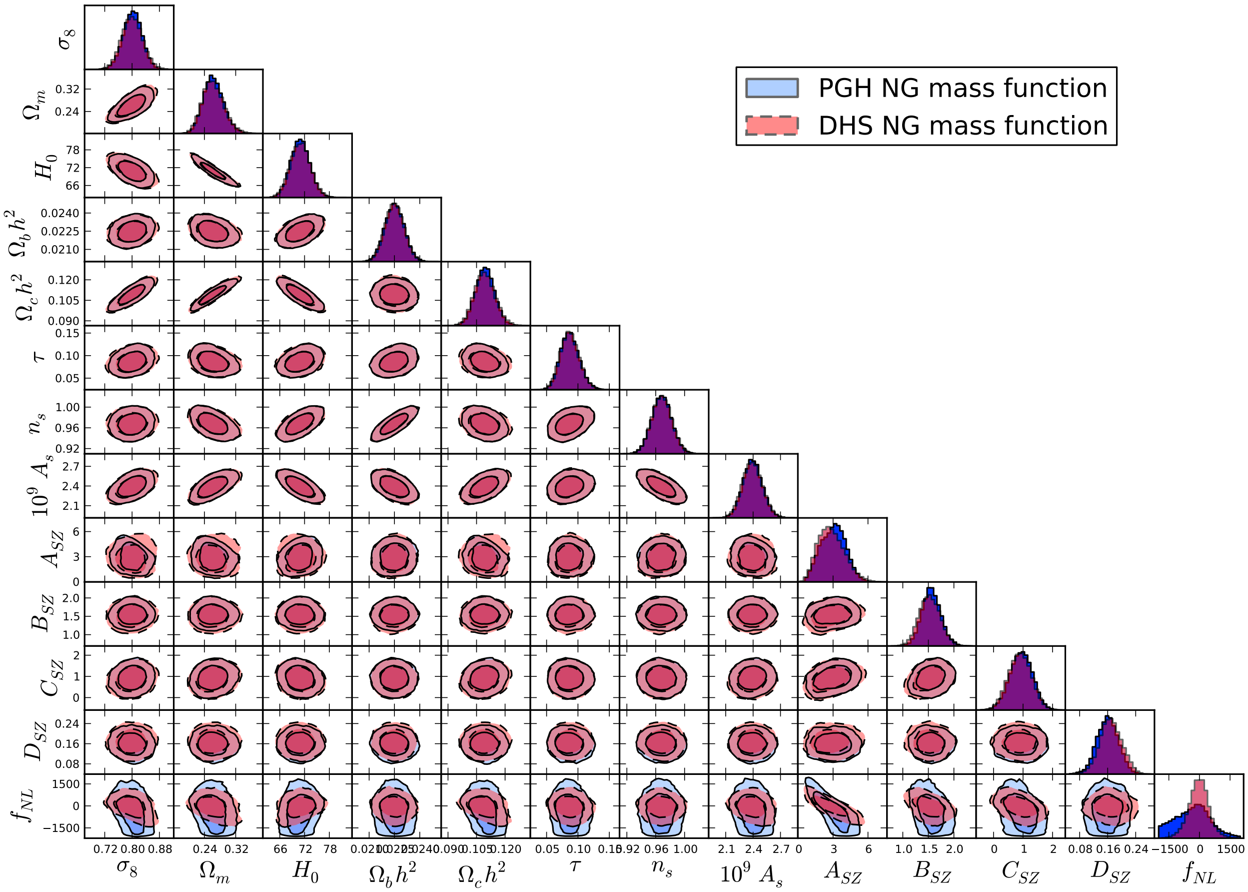

Figure 7–3: ΛCDM with f_{NL} parameter grid displaying the 68% and 95% confidence contours for the PGH and DHS non-Gaussian mass functions. Also shown are the marginalized, one-dimensional histograms.

values. However, as with the Gaussian case, the non-Gaussian best-fit amplitude for the scaling relation (A_{SZ}) is decreased with respect to the prior value while the mass-evolution (B_{SZ}) best-fit value is steeper and displays a slightly decreased uncertainty. Both of these variation are consistent with their priors, with the change in B_{SZ} representing a $\sim 1\sigma$ deviation in the non-Gaussian results. The remaining scaling relation parameters are not altered appreciable with respect to their priors, similar to the Gaussian case.

Table 7–1 also shows that, for both non-Gaussian formulations, the W11 catalog displays consistency with the standard, Gaussian, $f_{NL} = 0$, ΛCDM cosmology. For the DHS non-Gaussian analysis the 68% confidence limits on f_{NL} are $f_{NL} = -36^{+456}_{-491}$, offering no significant detection of primordial non-Gaussianity in the observed cluster abundance. In the case of the PGH analysis, we find a similar result where the best-fit value for this parameter is less than zero with a fairly large uncertainty. The 68% confidence limits for the non-Gaussianity parameter in the PGH analysis are $f_{NL} = -319^{+796}_{-930}$.

As shown in the marginalized histogram presented in Figure 7–3, the PGH likelihood appears to be asymmetric with respect to f_{NL}. The cause of this asymmetry resides in the definitions of both the cluster likelihood (Equation 4.3) and the PGH mass function (Equations 2.39 and 2.41). As per the definition of the cluster log-likelihood, a multiplication of the expected cluster abundance by a constant factor results in a larger change to the log-likelihood than a division by that same factor. By defining the negative-f_{NL} PGH mass function to be the inverse of the positive-f_{NL} form, the cluster likelihood in the PGH formalism is more sensitive to changes in positive f_{NL}, resulting in the asymmetry shown in Figure 7–3.

The results for both non-Gaussian mass function techniques (presented in Table 7–1), while broadly consistent for most parameters, do show significant disparity in their best-fit values for the f_{NL} parameter (while still consistent with the Gaussian,

$f_{NL} = 0$ prediction). In particular, the preferred value for this parameter is significantly larger in the DHS implementation versus its PGH counterpart, and has a reduced uncertainty. The DHS constraints do not appear to display the same asymmetry present in the PGH case, instead appearing approximately Gaussian, as shown in the histogram of Figure 7–3. Unlike in the PGH results, the DHS posterior for the f_{NL} parameter does not display a "tail" extending to large negative f_{NL} values. It is the presence of this tail which draws the PGH fit for this parameter to more negative values while also extending its uncertainty. An examination of the marginalized histograms presented in Figure 7–3 shows both posteriors to peak quite near $f_{NL} = 0$. These figures also show that both implementations display some degeneracy between the non-Gaussianity parameter and both σ_8 and A_{SZ}.

The relationship between f_{NL} and σ_8 is presented for both methods in Figure 7–4. As the non-Gaussianity parameter increases (increasing the predicted cluster counts), σ_8 decreases with an opposite effect occurring for decreases in f_{NL}. This effect is slightly more pronounced in the DHS formalism due to its higher f_{NL}-sensitivity, as shown in Figures 7–1 and 7–2. While the PGH non-Gaussian formulation permits larger deviations in negative f_{NL}, both constraints show remarkable agreement and are consistent with the Gaussian $f_{NL} = 0$ condition.

The second relationship to be explored is that which exists between the non-Gaussianity parameter and the normalization of the mass-significance scaling relation A_{SZ}, presented in Figure 7–5. The degeneracy between these two parameters is apparent in both the PGH and DHS methodologies. The interaction between these two parameters is quite similar to that observed in the f_{NL}-σ_8 case described above,

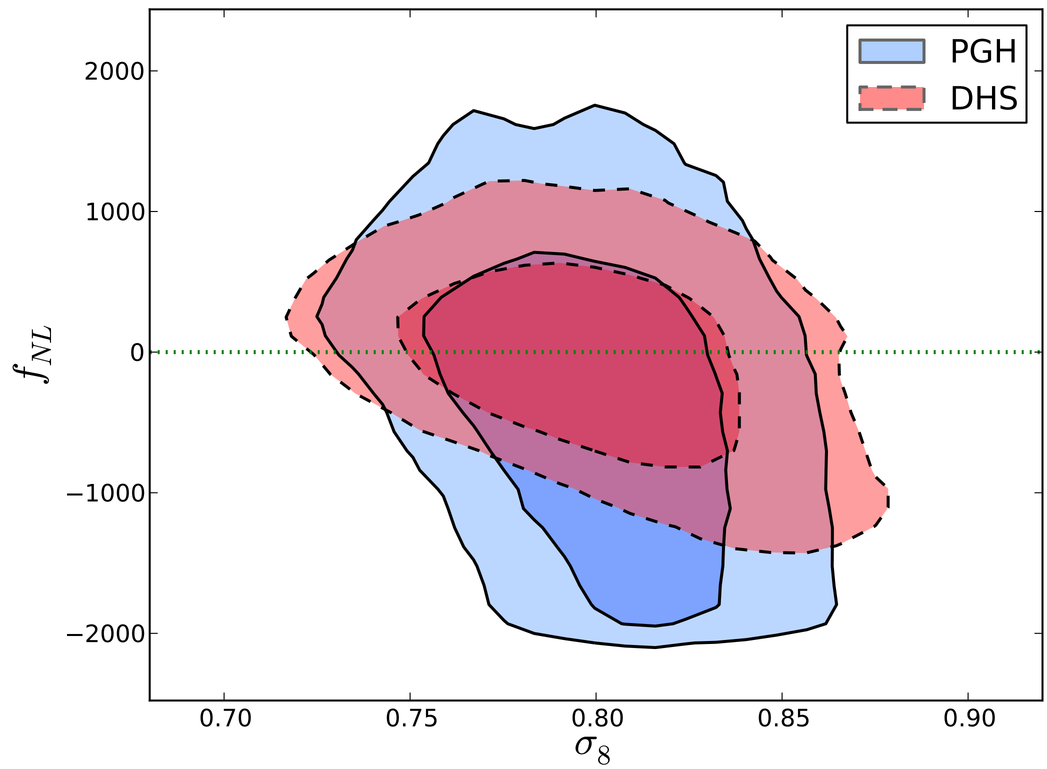

Figure 7–4: Two-dimensional 68% and 95% confidence intervals for the f_{NL} and σ_8 parameters in both the PGH and DHS non-Gaussian implementations. The Gaussian $f_{NL} = 0$ condition is shown dotted.

whereby increases in the predicted counts due to positive f_{NL} are met with decreases in A_{SZ}, which act to lower the predicted abundances. Evident in Figure 7–5 is the effect of the Gaussian prior on the scaling relation, whose mean and standard deviation are defined as $A_{SZ} = 3.51 \pm 1.05$ for the W11 cluster catalog. While the best-fit values for A_{SZ} are both consistent with the prior, Figure 7–5 show a clear preference for a decreased value of A_{SZ}. Ignoring changes to other parameters, this would indicate an observed deficit of clusters when compared with simulation, similar to the results of the Gaussian analysis.

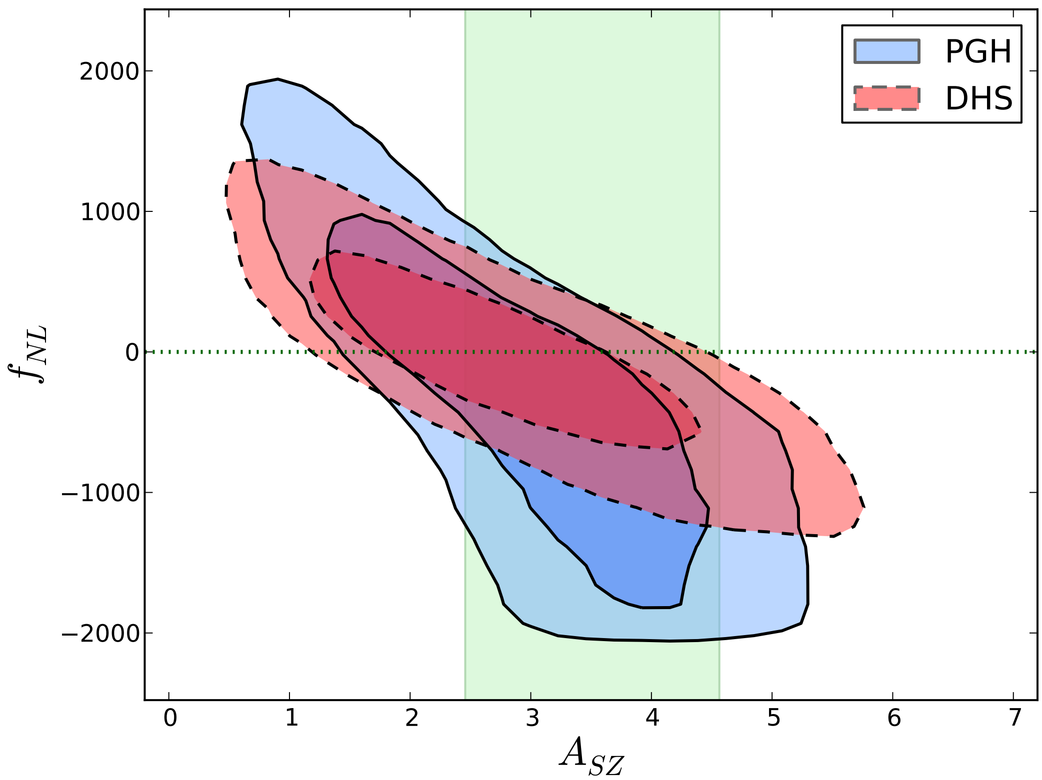

Figure 7–5: Two-dimensional 68% and 95% confidence intervals for the f_{NL} and A_{SZ} parameters in both the PGH and DHS non-Gaussian implementations. The Gaussian $f_{NL} = 0$ condition is shown dotted and the 1σ Gaussian prior on A_{SZ} is represented by the shaded vertical band.

As performed in Chapter 6, we can forecast the effect of an improved mass calibration by reducing the prior placed upon A_{SZ}. When the Gaussian prior on A_{SZ} is reduced from 30% to 10%, the uncertainty on f_{NL} for the PGH method improves from $\sigma_{f_{NL}} = 831$ to $\sigma_{f_{NL}} = 581$, while for the DHS method $\sigma_{f_{NL}}$ improves from $\sigma_{f_{NL}} = 508$ to $\sigma_{f_{NL}} = 293$ with this reduced prior. Future analyses, with increased catalogs, may improve upon these forecast constraints, potentially offering the sensitivity to constrain $f_{NL} \neq 0$.

It is also of interest to compare these f_{NL} constraints (both real and forecast) with those presented in other works which employ the abundance of massive galaxy clusters. One such analysis, presented in Cayon et al. [183], computes the probability associated with the single high mass cluster XMMU J2235.3-2557 whose weak-lensing mass was initially computed in Jee et al. [24] as $M_{200}(\rho_{crit}) = 7.3 \pm 1.3 \times 10^{14} M_{\odot}$ at a redshift of $z = 1.4$. This cluster is more distant than the highest redshift cluster in the W11 catalog (SPT-CL J2106-5844 at $z = 1.132$). The mass of this cluster is considerably less than many of the lower-redshift clusters in the W11 catalog, despite being defined at a larger radius (M_{200} versus M_{500}) [84]. The likelihood of observing such a massive and distant galaxy cluster as a cosmologically dependent quantity is explored in Cayon et al. [183].

The result of this single object analysis is $f_{NL} = 529 \pm 194$, in tension with the $f_{NL} = 0$ Gaussian model as well as the non-Gaussian constraints presented here, which find $f_{NL} < 477$ and $f_{NL} < 420$ at 68% confidence for the PGH and DHS models respectively. A separate analysis technique, presented in Hoyle et al. [23], uses a composite list of 15 massive clusters (including XMMU J2235.3-2557) as a test of non-Gaussianity. The resulting analysis finds that, for a fixed WMAP-preferred cosmology, $f_{NL} > 467$ at 95% confidence and that, when marginalized over cosmologies, $f_{NL} \gtrsim 123$ at 95% confidence. This result is again in tension with the

Gaussian case but is consistent with our analysis. There are, however, important differences from our analysis of the W11 sample.

Unlike the statistically complete cluster catalog utilized in our analysis, the non-Gaussian constraints presented in Cayon et al. [183] and Hoyle et al. [23] are calculated from a cluster set which is chosen, by design, to represent the rarest and most massive clusters in the universe. One complication to this method lies in accurately computing the effective area for such a composite catalog. This presents a non-trivial endeavour, particularly for experiments which scan multiple fields, requiring a choice of either a single field area or the entire survey. The selection function for such a cluster set is also difficult to accurately model, especially when considering multiple detection methods (such as X-ray, optical, and SZ). Finally, by artificially selecting only the rarest and most massive clusters from separate surveys, these analyses neglect a key component in the cluster likelihood, namely what is *not* seen.

For example, in the single object analysis presented in Cayon et al. [183], the presence of a single, massive cluster placed within a small survey area results in a constraint which predicts a significant degree of non-Gaussianity in the universe ($f_{NL} = 529 \pm 194$). However, as shown in Figure 7–1, large values of f_{NL} are shown to boost the amplitude of the mass function across a wide range in mass. While positive f_{NL} increases the probability of observing a single high-mass object, it also greatly increases the predicted number of objects at slightly lower mass as well. In particular, for a level of non-Gaussianity consistent with the result quoted in Cayon et al. [183], we would expect an approximate tripling in the total predicted cluster counts above our significance threshold, when compared with the Gaussian case. By tailoring the probability to account only for these massive clusters, these procedures effectively neglect the second term in the cluster likelihood (Equation 4.3). Thus, the existence of rare, high-mass clusters provides important information concerning the degree of non-Gaussianity in the universe, as does the existence and non-existence of lower mass objects. In this work we consistently include all relevant information in our analyses.

CHAPTER 8
Conclusions

In this work we motivated, derived and analyzed the constraints on modern cosmological theory offered by galaxy cluster abundances. In this process we demonstrated the means by which galaxy clusters may be utilized as probes of cosmology. The focus of this work lay in deriving and applying a likelihood formulation for the observed cluster abundance. Through measurements of the cluster abundance we explored three cosmological models, deriving useful constraints on cosmological parameters and testing deviations from the fiducial cosmological paradigm. These analyses included the canonical, six-parameter ΛCDM model and two extensions: a model wherein the dark energy component is not required to be in the form of a cosmological constant and one which permits the existence of primordial non-Gaussianity.

In Chapters 5, 6 and 7 the results of the cluster likelihood analysis were presented for the cosmological models introduced earlier. The first such model, as presented in Section 1.3, was the fiducial ΛCDM cosmology. In this chapter cosmological constraints were presented for the SZ-selected V10 galaxy cluster catalog both with and without external supplementary datasets. This cluster analysis was shown to be consistent with the ΛCDM paradigm, lending further support for the canonical cosmological model. The properties of the cluster dataset were also shown to be consistent with predictions and scaling relations derived from simulations. The cosmological constraints obtained from the cluster likelihood were also found to be consistent with those obtained from the WMAP7 dataset (Table 5–2) and were shown to depend upon the precision with which the cluster scaling relation was calibrated.

The cluster analysis was found to be especially sensitive to the matter power spectrum normalization parameter, σ_8. The cluster-only constraint for this parameter was $\sigma_8 = 0.745 \pm 0.082$, improving to $\sigma_8 = 0.796 \pm 0.026$ when the WMAP7 data was included. This parameter was also shown to exhibit strong degeneracies (Figure 5–9) with the amplitude of the cluster scaling relation, A_{SZ}. The best fit for this normalization parameter in the joint WMAP7-cluster likelihood was $A_{SZ} = 4.92 \pm 1.00$. This best-fit value is slightly less than central value predicted by simulations, but well within the uncertainty of that prediction ($A_{SZ} = 6.01 \pm 1.80$).

In Chapter 6 we expanded the cluster likelihood analysis to the wCDM cosmological model, wherein the dark energy component is permitted to exist in forms other than a cosmological constant. This model was parameterized in terms of the time-independent dark energy equation of state parameter w, modifications to which were shown to affect the abundance of cosmic structure. The results of the cluster analysis were demonstrated to be consistent with a cosmological constant form of dark energy, finding no evidence for departures from $w = -1$. In particular, the cluster analysis finds $w < -1/3$ at 90% confidence, providing strong, independent evidence for an accelerating expansion. For this model, the cluster-based cosmological constraints were again found to be consistent with those derived from the WMAP7 data (Table 6–2). The best fit dark energy equation of state, derived from the V10 cluster data, was $w = -1.16 \pm 0.47$, indicating no tension with a cosmological constant form of dark energy and weakly preferring a phantom-type form of dark energy.

When both the WMAP7 and HST data were added to the cluster likelihood the dark energy equation of state constraint improved to $w = -1.07 \pm 0.12$, remaining in good agreement with a cosmological constant. For these constraints the cluster likelihood was shown to be sensitive to w primarily through alterations to the total expected cluster abundance and, as such, it was degenerate with both σ_8 and A_{SZ}. The joint best fits for these parameters were $\sigma_8 = 0.817 \pm 0.050$ and $A_{SZ} = 4.65 \pm 1.18$, both of which are consistent with their ΛCDM counterparts, with slightly increased uncertainties. Through its degeneracy with A_{SZ}, the dark energy equation of state constraint was shown to depend upon the precision of the cluster scaling relation calibration, where a more precise calibration was demonstrated to reduce the uncertainty associated with this parameter.

In Chapter 7 excursions from a Gaussian spectrum of initial perturbations were explored. This model was parameterized through the non-Gaussianity parameter f_{NL} which acted as a measure of the local form of non-Gaussianity. The analysis in this chapter focused upon two implementations of non-Gaussian modifications to the cluster likelihood. For this analysis the W11 SZ-selected galaxy cluster catalog was employed, providing a statistically complete, wide area sample of the most massive clusters in the universe. Through this cluster analysis we found no evidence for non-Gaussian features in the primordial fluctuations, demonstrating consistency with the $f_{NL} = 0$ Gaussian condition.

Specifically, the results of the cluster non-Gaussianity analysis (Table 7–1) found $f_{NL} = -319^{+796}_{-930}$ and $f_{NL} = -36^{+456}_{-491}$ for the PGH and DHS non-Gaussian implementations respectively. These results were demonstrated to depend upon the cluster scaling relation calibration, where increased precision in this calibration was shown to decrease uncertainties on the f_{NL} parameter.

In this work the viability and constraining power of the cluster abundance likelihood was demonstrated. This method was shown to be capable of testing and constraining cosmological theory, placing useful constraints upon parameters for a variety of cosmological models. The results of our cluster analysis were demonstrated to be consistent with the fiducial ΛCDM model, supportive of a spectrum of Gaussian primordial fluctuations and a cosmological constant form of dark energy.

While the analyses presented in this work were derived from catalogs containing fewer than twenty galaxy clusters each, future galaxy cluster surveys, through increased survey area and sensitivity, are expected to detect many times this number [184, 185, 186, 187, 188]. For example, the most recent SPT cluster catalog contains more than 100 galaxy clusters, while the final SPT cluster catalog will contain many times more [139]. For SPT and other upcoming galaxy cluster surveys (e.g. eROSITA [185], XMM-Newton [189], CCAT [187], DES [188], and others) a precise calibration of the cluster mass-observable scaling relation will prove critical. Since, even for small catalogs, a 30% uncertainty in the scaling relation normalization (as used in this work) will dominate over the shot noise of the catalog, increasing the size of the cluster catalog without decreasing this uncertainty will not result in significantly improved parameter constraints.

Precise calibration of these scaling relations is an ongoing pursuit, achieved through improved estimations of cluster masses and comparisons between differing cluster mass proxies [172, 190, 191]. An example of recent efforts is presented in Benson et al. [171] which provides improved cosmological constraints for the V10 cluster catalog through the addition of complementary X-ray cluster data. By forming the joint likelihood estimator of a cluster's mass, given both SZ and X-ray proxies, the uncertainty of the scaling relation normalization is reduced, resulting in more stringent parameter constraints. A similar analysis is performed for a larger SPT cluster catalog in Reichardt et al. [139], while High et al. [173] explores the use of cluster masses derived from weak lensing data. In this manner, future galaxy cluster surveys, through increased survey area and precision calibration, aim to further decrease the uncertainty on cosmological parameters. Through these observations of the local universe, we will gain further insight into the nature of dark energy and the primordial processes responsible for the cosmic structure observed today.

REFERENCES

[1] A. Friedmann. Über die krümmung des raumes. *Zeitschrift fur Physik*, 10: 377–386, December 1922.

[2] Georges Lemaitre. A homogeneous Universe of constant mass and growing radius accounting for the radial velocity of extragalactic nebulae. *Annales Soc.Sci.Brux.Ser.I Sci.Math.Astron.Phys.*, A47:49–59, 1927.

[3] E. Hubble. A Relation between Distance and Radial Velocity among Extra-Galactic Nebulae. *Proceedings of the National Academy of Science*, 15:168–173, mar 1929.

[4] S. Dodelson. *Modern Cosmology*. Academic Press, San Diego, 2003.

[5] P. J. E. Peebles. *Principles of Physical Cosmology*. Princeton Theories in Physics. Princeton University Press, 1993.

[6] John Peacock. *Cosmological Physics*. Cambridge University Press, Cambridge, 1999.

[7] Edmund J. Copeland, M. Sami, and Shinji Tsujikawa. Dynamics of dark energy. *Int.J.Mod.Phys.*, D15:1753–1936, 2006, hep-th/0603057.

[8] S. Carroll. *An Introduction to General Relativity: Spacetime and Geometry*. Addison-Wesley, San Francisco, 2004.

[9] Sean M. Carroll. The Cosmological constant. *Living Rev.Rel.*, 4:1, 2001, astro-ph/0004075.

[10] T. Padmanabhan. Cosmological constant: The Weight of the vacuum. *Phys.Rept.*, 380:235–320, 2003, hep-th/0212290.

[11] E. Komatsu et al. Seven-Year Wilkinson Microwave Anisotropy Probe (WMAP) Observations: Cosmological Interpretation. *Astrophys.J.Suppl.*, 192: 18, 2011, 1001.4538.

[12] Rennan Barkana and Abraham Loeb. In the beginning: The First sources of light and the reionization of the Universe. *Phys.Rept.*, 349:125–238, 2001, astro-ph/0010468.

[13] O. Zahn, C.L. Reichardt, L. Shaw, A. Lidz, K.A. Aird, et al. Cosmic microwave background constraints on the duration and timing of reionization from the South Pole Telescope. 2011, 1111.6386.

[14] S. Burles, K.M. Nollett, and Michael S. Turner. What is the BBN prediction for the baryon density and how reliable is it? *Phys.Rev.*, D63:063512, 2001, astro-ph/0008495.

[15] Beth A. Reid et al. Baryon Acoustic Oscillations in the Sloan Digital Sky Survey Data Release 7 Galaxy Sample. *Mon.Not.Roy.Astron.Soc.*, 401:2148–2168, 2010, 0907.1660.

[16] R. Amanullah et al. Spectra and Light Curves of Six Type Ia Supernovae at $0.511 < z < 1.12$ and the Union2 Compilation. *Astrophys. J.*, 716:712–738, 2010, 1004.1711.

[17] N. Suzuki, D. Rubin, C. Lidman, G. Aldering, R. Amanullah, et al. The Hubble Space Telescope Cluster Supernova Survey: V. Improving the Dark Energy Constraints Above $z > 1$ and Building an Early-Type-Hosted Supernova Sample. 2011, 1105.3470.

[18] D. Larson et al. Seven-Year Wilkinson Microwave Anisotropy Probe (WMAP) Observations: Power Spectra and WMAP-Derived Parameters. *Astrophys. J. Suppl.*, 192:16, 2011, 1001.4635.

[19] R. Keisler et al. A Measurement of the Damping Tail of the Cosmic Microwave Background Power Spectrum with the South Pole Telescope. 2011, 1105.3182.

[20] D.N. Spergel et al. First year Wilkinson Microwave Anisotropy Probe (WMAP) observations: Determination of cosmological parameters. *Astrophys.J.Suppl.*, 148:175–194, 2003, astro-ph/0302209.

[21] M. Ackermann et al. Search for Dark Matter Satellites using the FERMI-LAT. 2012, 1201.2691.

[22] Richard H. Cyburt, Brian D. Fields, and Keith A. Olive. An Update on the big bang nucleosynthesis prediction for Li-7: The problem worsens. *JCAP*, 0811:012, 2008, 0808.2818.

[23] Ben Hoyle, Raul Jimenez, and Licia Verde. Implications of multiple high-redshift galaxy clusters. *Phys.Rev.*, D83:103502, 2011, 1009.3884.

[24] M.J. Jee, P. Rosati, H.C. Ford, K.S. Dawson, C. Lidman, et al. Hubble Space Telescope Weak-lensing Study of the Galaxy Cluster XMMU J2235.3-2557 at $z = 1.4$: A Surprisingly Massive Galaxy Cluster when the Universe is One-third of its Current Age. *Astrophys.J.*, 704:672–686, 2009, 0908.3897.

[25] Lawrence M. Krauss, Katherine Jones-Smith, and Dragan Huterer. Dark Energy, A Cosmological Constant, and Type Ia Supernovae. *New J.Phys.*, 9:141, 2007, astro-ph/0701692.

[26] V. Barger, E. Guarnaccia, and D. Marfatia. Classification of dark energy models in the (w(0), w(a)) plane. *Phys.Lett.*, B635:61–65, 2006, hep-ph/0512320.

[27] R.R. Caldwell, Rahul Dave, and Paul J. Steinhardt. Cosmological imprint of an energy component with general equation of state. *Phys.Rev.Lett.*, 80: 1582–1585, 1998, astro-ph/9708069.

[28] Robert R. Caldwell, Marc Kamionkowski, and Nevin N. Weinberg. Phantom energy and cosmic doomsday. *Phys.Rev.Lett.*, 91:071301, 2003, astro-ph/0302506.

[29] Eric V. Linder and Dragan Huterer. How many dark energy parameters? *Phys.Rev.*, D72:043509, 2005, astro-ph/0505330.

[30] P.J.E. Peebles and Bharat Ratra. Cosmology with a Time Variable Cosmological Constant. *Astrophys.J.*, 325:L17, 1988.

[31] P.P. Avelino, L. Losano, and J.J. Rodrigues. Quintessence and tachyon dark energy models with a constant equation of state parameter. *Phys.Lett.*, B699: 10–14, 2011, 1103.1384.

[32] Ralf Aurich and Frank Steiner. Quintessence with a constant equation of state in hyperbolic universes. *Phys.Rev.*, D67:123511, 2003, astro-ph/0212471.

[33] Li-Min Wang, R.R. Caldwell, J.P. Ostriker, and Paul J. Steinhardt. Cosmic concordance and quintessence. *Astrophys.J.*, 530:17–35, 2000, astro-ph/9901388.

[34] R.R. Caldwell. A Phantom menace? *Phys.Lett.*, B545:23–29, 2002, astro-ph/9908168.

[35] Artyom V. Astashenok, Shin'ichi Nojiri, Sergei D. Odintsov, and Artyom V. Yurov. Phantom Cosmology without Big Rip Singularity. 2012, 1201.4056.

[36] Vinod B. Johri. Phantom cosmologies. *Phys.Rev.*, D70:041303, 2004, astro-ph/0311293.

[37] Alan H. Guth. The Inflationary Universe: A Possible Solution to the Horizon and Flatness Problems. *Phys. Rev.*, D23:347–356, 1981.

[38] Alan H. Guth and So-Young Pi. The Quantum Mechanics of the Scalar Field in the New Inflationary Universe. *Phys.Rev.*, D32:1899–1920, 1985.

[39] A. Albrecht and P. J. Steinhardt. Cosmology for grand unified theories with radiatively induced symmetry breaking. *Physical Review Letters*, 48:1220–1223, April 1982.

[40] A. D. Linde. A new inflationary universe scenario: A possible solution of the horizon, flatness, homogeneity, isotropy and primordial monopole problems. *Physics Letters B*, 108:389–393, February 1982.

[41] Karim A. Malik and David Wands. Cosmological perturbations. *Phys.Rept.*, 475:1–51, 2009, 0809.4944.

[42] David H. Lyth and Antonio Riotto. Particle physics models of inflation and the cosmological density perturbation. *Phys.Rept.*, 314:1–146, 1999, hep-ph/9807278.

[43] N. Bartolo, E. Komatsu, Sabino Matarrese, and A. Riotto. Non-Gaussianity from inflation: Theory and observations. *Phys.Rept.*, 402:103–266, 2004, astro-ph/0406398.

[44] Robert H. Brandenberger. Introduction to Early Universe Cosmology. *PoS*, ICFI2010:001, 2010, 1103.2271.

[45] Rouzbeh Allahverdi, Robert Brandenberger, Francis-Yan Cyr-Racine, and Anupam Mazumdar. Reheating in Inflationary Cosmology: Theory and Applications. *Ann.Rev.Nucl.Part.Sci.*, 60:27–51, 2010, 1001.2600.

[46] D.N. Spergel et al. Wilkinson Microwave Anisotropy Probe (WMAP) three year results: implications for cosmology. *Astrophys.J.Suppl.*, 170:377, 2007, astro-ph/0603449.

[47] E. Komatsu et al. Five-Year Wilkinson Microwave Anisotropy Probe (WMAP) Observations: Cosmological Interpretation. *Astrophys.J.Suppl.*, 180:330–376, 2009, 0803.0547.

[48] Christos G. Tsagas. Cosmological perturbations. *Lect.Notes Phys.*, 592:223–261, 2002, astro-ph/0201405.

[49] P. Meszaros. The behaviour of point masses in an expanding cosmological substratum. *Astron.Astrophys.*, 37:225–228, 1974.

[50] Daniel J. Eisenstein and Wayne Hu. Power Spectra for Cold Dark Matter and its Variants. *Astrophys. J.*, 511:5, 1997, astro-ph/9710252.

[51] Sean M. Carroll, William H. Press, and Edwin L. Turner. The Cosmological constant. *Ann. Rev. Astron. Astrophys.*, 30:499–542, 1992.

[52] D. J. Heath. The growth of density perturbations in zero pressure Friedmann-Lemaitre universes. *Mon. Not. Roy. Astron. Soc.*, 179:351–358, May 1977.

[53] Daniel J. Eisenstein and Wayne Hu. Baryonic Features in the Matter Transfer Function. *Astrophys. J.*, 496:605, 1998, astro-ph/9709112.

[54] Antony Lewis, Anthony Challinor, and Anthony Lasenby. Efficient computation of CMB anisotropies in closed FRW models. *Astrophys. J.*, 538:473–476, 2000, astro-ph/9911177.

[55] Christian T. Byrnes, Ki-Young Choi, and Lisa M. H. Hall. Conditions for large non-Gaussianity in two-field slow- roll inflation. *JCAP*, 0810:008, 2008, 0807.1101.

[56] Ki-Young Choi and Bumseok Kyae. Natural Hybrid Inflation Model with Large Non- Gaussianity. 2011, 1109.4245.

[57] Carlos Cunha, Dragan Huterer, and Olivier Dore. Primordial non-Gaussianity from the covariance of galaxy cluster counts. *Phys. Rev.*, D82:023004, 2010, 1003.2416.

[58] Neal Dalal, Olivier Dore, Dragan Huterer, and Alexander Shirokov. The imprints of primordial non-gaussianities on large- scale structure: scale dependent bias and abundance of virialized objects. *Phys. Rev.*, D77:123514, 2008, 0710.4560.

[59] Vincent Desjacques and Uros Seljak. Signature of primordial non-Gaussianity of ϕ^3-type in the mass function and bias of dark matter haloes. *Phys. Rev.*, D81:023006, 2010, 0907.2257.

[60] M. Grossi et al. Large-scale non-Gaussian mass function and halo bias: tests on N-body simulations. *Mon. Not. Roy. Astron. Soc.*, 398:321–332, 2009, 0902.2013.

[61] Marilena LoVerde, Amber Miller, Sarah Shandera, and Licia Verde. Effects of Scale-Dependent Non-Gaussianity on Cosmological Structures. *JCAP*, 0804:014, 2008, 0711.4126.

[62] Marilena LoVerde and Kendrick M. Smith. The Non-Gaussian Halo Mass Function with fNL, gNL and tauNL. *JCAP*, 1108:003, 2011, 1102.1439.

[63] Jun-Qing Xia, Carlo Baccigalupi, Sabino Matarrese, Licia Verde, and Matteo Viel. Constraints on Primordial Non-Gaussianity from Large Scale Structure Probes. *JCAP*, 1108:033, 2011, 1104.5015.

[64] Jun-Qing Xia et al. Primordial Non-Gaussianity and the NRAO VLA Sky Survey. *Astrophys. J.*, 717:L17, 2010, 1003.3451.

[65] Eiichiro Komatsu. Hunting for Primordial Non-Gaussianity in the Cosmic Microwave Background. *Class.Quant.Grav.*, 27:124010, 2010, 1003.6097.

[66] Juan Martin Maldacena. Non-Gaussian features of primordial fluctuations in single field inflationary models. *JHEP*, 0305:013, 2003, astro-ph/0210603.

[67] Jinn-Ouk Gong, Jai-chan Hwang, and Hyerim Noh. Classical non-Gaussianity from non-linear evolution of curvature perturbations. 2011, 1108.2267.

[68] Viviana Acquaviva, Nicola Bartolo, Sabino Matarrese, and Antonio Riotto. Second order cosmological perturbations from inflation. *Nucl.Phys.*, B667:119–148, 2003, astro-ph/0209156.

[69] William H. Press and Paul Schechter. Formation of galaxies and clusters of galaxies by selfsimilar gravitational condensation. *Astrophys. J.*, 187:425–438, 1974.

[70] James M. Bardeen, J. R. Bond, Nick Kaiser, and A. S. Szalay. The Statistics of Peaks of Gaussian Random Fields. *Astrophys. J.*, 304:15–61, 1986.

[71] J. R. Bond, S. Cole, G. Efstathiou, and Nick Kaiser. Excursion set mass functions for hierarchical Gaussian fluctuations. *Astrophys. J.*, 379:440, 1991.

[72] Ravi K. Sheth and Giuseppe Tormen. Large scale bias and the peak background split. *Mon. Not. Roy. Astron. Soc.*, 308:119, 1999, astro-ph/9901122.

[73] Ravi K. Sheth, H. J. Mo, and Giuseppe Tormen. Ellipsoidal collapse and an improved model for the number and spatial distribution of dark matter haloes. *Mon. Not. Roy. Astron. Soc.*, 323:1, 2001, astro-ph/9907024.

[74] Volker Springel et al. Simulating the joint evolution of quasars, galaxies and their large-scale distribution. *Nature*, 435:629–636, 2005, astro-ph/0504097.

[75] Stefan Gottloeber, G. Yepes, C. Wagner, and R. Sevilla. The MareNostrum universe. 2006, astro-ph/0608289.

[76] Jeremy L. Tinker et al. Toward a halo mass function for precision cosmology: the limits of universality. *Astrophys. J.*, 688:709–728, 2008, 0803.2706.

[77] Marc Davis, George Efstathiou, Carlos S. Frenk, and Simon D. M. White. The evolution of large-scale structure in a universe dominated by cold dark matter. *Astrophys. J.*, 292:371–394, 1985.

[78] Surhud More, Andrey Kravtsov, Neal Dalal, and Stefan Gottlober. The overdensity and masses of the friends-of-friends halos and universality of the halo

mass function. *Astrophys. J. Supp.*, 195:4, 2011, 1103.0005.

[79] Cedric G. Lacey and Shaun Cole. Merger rates in hierarchical models of galaxy formation. 2. Comparison with N body simulations. *Mon. Not. Roy. Astron. Soc.*, 271:676, 1994, astro-ph/9402069.

[80] A. Jenkins et al. Mass function of dark matter halos. *Mon. Not. Roy. Astron. Soc.*, 321:372, 2001, astro-ph/0005260.

[81] Onsi Fakhouri and Chung-Pei Ma. The Nearly Universal Merger Rate of Dark Matter Haloes in Lambda-CDM Cosmology. 2007, 0710.4567.

[82] Darren Reed, Richard Bower, Carlos Frenk, Adrian Jenkins, and Tom Theuns. The halo mass function from the dark ages through the present day. *Mon. Not. Roy. Astron. Soc.*, 374:2–15, 2007, astro-ph/0607150.

[83] K. Vanderlinde et al. Galaxy Clusters Selected with the Sunyaev-Zel'dovich Effect from 2008 South Pole Telescope Observations. *Astrophys. J.*, 722:1180–1196, 2010, 1003.0003.

[84] R. Williamson, B.A. Benson, F.W. High, K. Vanderlinde, P.A.R. Ade, et al. An SZ-selected sample of the most massive galaxy clusters in the 2500-square-degree South Pole Telescope survey. *Astrophys.J.*, 738:139, 2011, 1101.1290.

[85] Kari Enqvist, Shaun Hotchkiss, and Olli Taanila. Estimating f_{NL} and g_{NL} from Massive High-Redshift Galaxy Clusters. *JCAP*, 1104:017, 2011, 1012.2732.

[86] Sabino Matarrese, Licia Verde, and Raul Jimenez. The abundance of high-redshift objects as a probe of non- Gaussian initial conditions. *Astrophys. J.*, 541:10, 2000, astro-ph/0001366.

[87] Sirichai Chongchitnan and Joseph Silk. A Study of High-Order Non-Gaussianity with Applications to Massive Clusters and Large Voids. *Astrophys.J.*, 724:285–295, 2010, 1007.1230.

[88] Jurg Diemand and Ben Moore. The structure and evolution of cold dark matter halos. 2009, 0906.4340.

[89] Brant Robertson, Andrey Kravtsov, Jeremy Tinker, and Andrew Zentner. Collapse Barriers and Halo Abundance: Testing the Excursion Set Ansatz. *Astrophys.J.*, 696:636–652, 2009, 0812.3148.

[90] Martin J. White. The Mass of a halo. *Astron.Astrophys.*, 367:27, 2001, astro-ph/0011495.

[91] Uros Seljak. Analytic model for galaxy and dark matter clustering. *Mon.Not.Roy.Astron.Soc.*, 318:203, 2000, astro-ph/0001493.

[92] Martin J. White, 1. The mass function. *Astrophys. J. Suppl.*, 143:241, 2002, astro-ph/0207185.

[93] Wayne Hu and Andrey V. Kravtsov. Sample variance considerations for cluster surveys. *Astrophys.J.*, 584:702–715, 2003, astro-ph/0203169.

[94] G.L. Bryan and M.L. Norman. Statistical properties of x-ray clusters: Analytic and numerical comparisons. *Astrophys.J.*, 495:80, 1998, astro-ph/9710107.

[95] Aseem Paranjape, Christopher Gordon, and Shaun Hotchkiss. The Extreme Tail of the Non-Gaussian Mass Function. *Phys. Rev.*, D84:023517, 2011, 1104.1145.

[96] Shaun Hotchkiss. Quantifying the rareness of extreme galaxy clusters. *JCAP*, 1107:004, 2011, 1105.3630.

[97] Michael J. Mortonson, Wayne Hu, and Dragan Huterer. Simultaneous Falsification of ΛCDM and Quintessence with Massive, Distant Clusters. *Phys.Rev.*, D83:023015, 2011, 1011.0004.

[98] Ian Harrison and Peter Coles. Testing Cosmology with Extreme Galaxy Clusters. 2011, 1111.1184.

[99] Alan R. Duffy, Joop Schaye, Scott T. Kay, and Claudio Dalla Vecchia. Dark matter halo concentrations in the Wilkinson Microwave Anisotropy Probe year 5 cosmology. *Mon.Not.Roy.Astron.Soc.*, 390:L64, 2008, 0804.2486.

[100] Julio F. Navarro, Carlos S. Frenk, and Simon D.M. White. A Universal density profile from hierarchical clustering. *Astrophys.J.*, 490:493–508, 1997, astro-ph/9611107.

[101] Anthony H. Gonzalez, Dennis Zaritsky, and Ann I. Zabludoff. A Census of Baryons in Galaxy Clusters and Groups. *Astrophys. J.*, 666:147–155, 2007, 0705.1726.

[102] Yen-Ting Lin, Joseph J. Mohr, and S. A. Stanford. Near-IR Properties of Galaxy Clusters: Luminosity as a Binding Mass Predictor and the State of Cluster Baryons. *Astrophys. J.*, 591:749–763, 2003, astro-ph/0304033.

[103] H. Roussel, R. Sadat, and A. Blanchard. The baryon content of groups and clusters of galaxies. 2000, astro-ph/0007168.

[104] Yen-Ting Lin, S. Adam Stanford, Peter R.M. Eisenhardt, Alexey Vikhlinin, Ben J. Maughan, et al. Baryon Content of Massive Galaxy Clusters at $z = 0 - 0.6$. 2011, 1112.1705.

[105] Stefano Borgani and Andrey Kravtsov. Cosmological simulations of galaxy clusters. *ArXiv e-prints*, 2009, 0906.4370.

[106] Piero Rosati, Stefano Borgani, and Colin Norman. The Evolution of X-ray Clusters of Galaxies. *Ann. Rev. Astron. Astrophys.*, 40:539–577, 2002, astro-ph/0209035.

[107] H. Boehringer et al. The ROSAT-ESO Flux Limited X-Ray (REFLEX) Galaxy Cluster Survey I: The Construction of the Cluster Sample. *Astronomy and Astrophysics*, 369:826–850, April 2000, astro-ph/0012266.

[108] A. Vikhlinin et al. Chandra Cluster Cosmology Project III: Cosmological Parameter Constraints. *Astrophys. J.*, 692:1060–1074, 2009, 0812.2720.

[109] Adam Mantz, Steven W. Allen, David Rapetti, and Harald Ebeling. The Observed Growth of Massive Galaxy Clusters I: Statistical Methods and Cosmological Constraints. *Mon. Not. Roy. Astron. Soc.*, 406:1759–1772, 2010, 0909.3098.

[110] Reinabelle Reyes, Rachel Mandelbaum, Christopher M. Hirata, Neta Bahcall, and Uros Seljak. Improved optical mass tracer for galaxy clusters calibrated using weak lensing measurements. *Mon. Not. Roy. Astron. Soc.*, 390:1157–1169, 2008, 0802.2365.

[111] G. O. Abell. The Distribution of Rich Clusters of Galaxies. *ApJS*, 3:211, May 1958.

[112] F. Zwicky, E. Herzog, P. Wild, M. Karpowicz, and C. T. Kowal. *Catalogue of galaxies and of clusters of galaxies, Vol. I.* 1961.

[113] Michael D. Gladders et al. Cosmological Constraints from the Red-Sequence Cluster Survey. *Astrophys. J.*, 655:128–134, 2007, astro-ph/0603588.

[114] H.K.C. Yee et al. The Red-Sequence Cluster Surveys. *ASP Conf.Ser.*, 2007, astro-ph/0701839.

[115] Benjamin Koester et al. A MaxBCG Catalog of 13,823 Galaxy Clusters from the Sloan Digital Sky Survey. *Astrophys.J.*, 660:239–255, 2007, astro-ph/0701265.

[116] Donald G. York et al. The Sloan Digital Sky Survey: Technical Summary. *Astron.J.*, 120:1579–1587, 2000, astro-ph/0006396.

[117] Mark Birkinshaw. The Sunyaev-Zel'dovich Effect. *Phys. Rept.*, 310:97–195, 1999, astro-ph/9808050.

[118] A. Vikhlinin et al. Chandra Cluster Cosmology Project II: Samples and X-ray Data Reduction. *Astrophys. J.*, 692:1033–1059, 2009, 0805.2207.

[119] Nicolas Clerc, Tatyana Sadibekova, Marguerite Pierre, Florian Pacaud, Jean-Paul Le Fevre, et al. The cosmological analysis of X-ray cluster surveys: II-Application of the CR-HR method to the XMM archive. 2011, 1109.4441.

[120] Nicola Mehrtens, A. Kathy Romer, E.J. Lloyd-Davies, Matt Hilton, Christopher J. Miller, et al. The XMM Cluster Survey: Optical analysis methodology and the first data release. 2011, 1106.3056.

[121] J.R. Peterson, J.G. Jernigan, R.R. Gupta, J. Bankert, and S.M. Kahn. Evidence for Non-Linear Growth of Structure from an X-ray Selected Cluster Survey using a Novel Joint Analysis of the Chandra and XMM-Newton Archives. *Astrophys.J.*, 707:878–889, 2009, 0911.1327.

[122] H. Boehringer, P. Schuecker, L. Guzzo, C.A. Collins, W. Voges, et al. The ROSAT-ESO Flux Limited X-ray (REFLEX) Galaxy Cluster Survey. 5. The Cluster catalogue. *Astron.Astrophys.*, 425:367–383, 2004, astro-ph/0405546.

[123] R. A. Sunyaev and Ya. B. Zeldovich. Small-Scale Fluctuations of Relic Radiation. *Astrophysics and Space Science*, 7:3–19, April 1970.

[124] R. A. Sunyaev and Ya. B. Zeldovich. The Observations of relic radiation as a test of the nature of X-Ray radiation from the clusters of galaxies. *Comments Astrophys. Space Phys.*, 4:173–178, 1972.

[125] John E. Carlstrom, Gilbert P. Holder, and Erik D. Reese. Cosmology with the Sunyaev-Zel'dovich Effect. *Ann. Rev. Astron. Astrophys.*, 40:643–680, 2002, astro-ph/0208192.

[126] Y. Rephaeli. Cosmic microwave background comptonization by hot intracluster gas. *Astrophys. J.*, 445:33–36, May 1995.

[127] S. Y. Sazonov and R. A. Sunyaev. CMB Radiation in the Direction of a Moving Cluster of Galaxies with Hot Gas: Relativistic Corrections. *Astrophys. J.*, 508: 1–5, 1998, astro-ph/9804125.

[128] Albert Stebbins. Extensions to the Kompaneets Equation and Sunyaev-Zel'dovich Distortion. 1997, astro-ph/9709065.

[129] A.S. Kompaneets. The establishment of thermal equilibrium between quanta and electrons. *Zh. Eksp. Teor. fiz.*, 31:876, 1956. [Translation in Sov. Phys. JETP, 4, 730 (1957)].

[130] M. Zemcov, J. Aguirre, J. Bock, M. Bradford, N. Czakon, et al. High Spectral Resolution Measurement of the Sunyaev-Zel'dovich Effect Null with Z-Spec.

Astrophys.J., 749:114, 2012, 1202.0029.

[131] J. E. Carlstrom et al. The 10 Meter South Pole Telescope. 2009, 0907.4445.

[132] S. Padin, Z. Staniszewski, R. Keisler, M. Joy, A. A. Stark, P. A. R. Ade, K. A. Aird, B. A. Benson, L. E. Bleem, J. E. Carlstrom, C. L. Chang, T. M. Crawford, A. T. Crites, M. A. Dobbs, N. W. Halverson, S. Heimsath, R. E. Hills, W. L. Holzapfel, C. Lawrie, A. T. Lee, E. M. Leitch, J. Leong, W. Lu, M. Lueker, J. J. McMahon, S. S. Meyer, J. J. Mohr, T. E. Montroy, T. Plagge, C. Pryke, J. E. Ruhl, K. K. Schaffer, E. Shirokoff, H. G. Spieler, and J. D. Vieira. South pole telescope optics. *Appl.Opt.*, 47:4418–4428, August 2008.

[133] Z. Staniszewski et al. Galaxy clusters discovered with a Sunyaev-Zel'dovich effect survey. *Astrophys. J.*, 701:32–41, 2009, 0810.1578.

[134] Martin G. Haehnelt and Max Tegmark. Using the kinematic Sunyaev-Zeldovich effect to determine the peculiar velocities of clusters of galaxies. *Mon. Not. Roy. Astron. Soc.*, 279:545–556, 1996, astro-ph/9507077.

[135] D. Herranz, J. L. Sanz, R. B. Barreiro, and E. Martinez-Gonzalez. Scale-Adaptive filters for the detection/separation of compact sources. *Astrophys. J.*, 580:610–625, 2002, astro-ph/0204149.

[136] D. Herranz et al. Filtering techniques for the detection of Sunyaev- Zel'dovich clusters in multifrequency CMB maps. *Mon. Not. Roy. Astron. Soc.*, 336:1057, 2002, astro-ph/0203486.

[137] Jean-Baptiste Melin, James G. Bartlett, and Jacques Delabrouille. Catalog Extraction in SZ Cluster Surveys: a matched filter approach. 2006, astro-ph/0602424.

[138] F. W. High et al. Optical Redshift and Richness Estimates for Galaxy Clusters Selected with the Sunyaev-Zel'dovich Effect from 2008 South Pole Telescope Observations. *Astrophys. J.*, 723:1736–1747, 2010, 1003.0005.

[139] C.L. Reichardt, B. Stalder, L.E. Bleem, T.E. Montroy, K.A. Aird, et al. Galaxy clusters discovered via the Sunyaev-Zel'dovich effect in the first 720 square degrees of the South Pole Telescope survey. 2012, 1203.5775.

[140] Felipe Menanteau et al. Southern Cosmology Survey II: Massive Optically-Selected Clusters from 70 square degrees of the SZE Common Survey Area. *Astrophys. J. Suppl.*, 191:340–351, 2010, 1002.2226.

[141] Andrey V. Kravtsov, Alexey Vikhlinin, and Daisuke Nagai. A New Robust Low-Scatter X-ray Mass Indicator for Clusters of Galaxies. *Astrophys. J.*, 650: 128–136, 2006, astro-ph/0603205.

[142] Adam Mantz, Steven W. Allen, Harald Ebeling, David Rapetti, and Alex Drlica-Wagner. The Observed Growth of Massive Galaxy Clusters II: X-ray Scaling Relations. *Mon. Not. Roy. Astron. Soc.*, 406:1773–1795, 2010, 0909.3099.

[143] W. Cash. Parameter estimation in astronomy through application of the likelihood ratio. *Astrophys. J.*, 228:939–947, 1979.

[144] J.A. Nousek and D.R. Shue. Chi-squared and C statistic minimization for low count per bin data. *Astrophys. J.*, 342:1207–1211, July 1989.

[145] Gilbert P. Holder and John E. Carlstrom. The Sunyaev-Zeldovich effect as microwave foreground and probe of cosmology. 1999, astro-ph/9904220.

[146] Domingos Barbosa, James G. Bartlett, Alain Blanchard, and Jamila Oukbir. The Sunyaev-Zel'dovich effect and the value of Omega(o). *Astron.Astrophys.*, 314:13–17, 1996, astro-ph/9511084.

[147] Paul Bode, Jeremiah P. Ostriker, Jochen Weller, and Laurie Shaw. Accurate Realizations of the Ionized Gas in Galaxy Clusters: Calibrating Feedback. *Astrophys.J.*, 663:139–149, 2007, astro-ph/0612663.

[148] L.D. Shaw, O. Zahn, G.P. Holder, and O. Dore. Sharpening the Precision of the Sunyaev-Zel'dovich Power Spectrum. *Astrophys.J.*, 702:368–376, 2009, 0903.5322.

[149] Paul Bode, Jeremiah P. Ostriker, and Alexey Vikhlinin. Exploring the Energetics of Intracluster Gas with a Simple and Accurate Model. *Astrophys.J.*, 700:989–999, 2009, 0905.3748.

[150] C. C. Ngeow, J. Mohr, A. Zenteno, D. Data Management, BCS, and SPT Collaborations. The blanco cosmology survey: Data reduction, calibration and photometric redshift estimation to four distant galaxy clusters discovered by the south pole telescope. In *American Astronomical Society Meeting Abstracts #213*, volume 41 of *Bulletin of the American Astronomical Society*, page 448.04, January 2009.

[151] R.J. Foley, K. Andersson, G. Bazin, T. de Haan, J. Ruel, et al. Discovery and Cosmological Implications of SPT-CL J2106-5844, the Most Massive Known Cluster at $z > 1$. *Astrophys.J.*, 731:86, 2011, 1101.1286.

[152] Nelson Christensen and Renate Meyer. Bayesian Methods for Cosmological Parameter Estimation from Cosmic Microwave Background Measurements. 2000,

astro-ph/0006401.

[153] Nelson Christensen, Renate Meyer, Lloyd Knox, and Ben Luey. II. Bayesian methods for cosmological parameter estimation from cosmic microwave background measurements. *Class.Quant.Grav.*, 18:2677, 2001, astro-ph/0103134.

[154] Antony Lewis and Sarah Bridle. Cosmological parameters from CMB and other data: a Monte- Carlo approach. *Phys. Rev.*, D66:103511, 2002, astro-ph/0205436.

[155] Licia Verde et al. First Year Wilkinson Microwave Anisotropy Probe (WMAP) Observations: Parameter Estimation Methodology. *Astrophys. J. Suppl.*, 148: 195, 2003, astro-ph/0302218.

[156] Joanna Dunkley, Martin Bucher, Pedro G. Ferreira, Kavilan Moodley, and Constantinos Skordis. Fast and reliable MCMC for cosmological parameter estimation. *Mon. Not. Roy. Astron. Soc.*, 356:925–936, 2005, astro-ph/0405462.

[157] W.R. Gilks, S. Richardson, and D.J. Spiegelhalter. *Markov Chain Monte Carlo in Practice*. Chapman & Hall/CRC, New York, 1996.

[158] Nicholas Metropolis, Arianna W. Rosenbluth, Marshall N. Rosenbluth, Augusta H. Teller, and Edward Teller. Equation of state calculations by fast computing machines. *Journal of Chemical Physics*, 21:1087–1092, 1953.

[159] W.K. Hastings. Monte carlo samping methods using markov chains and their applications. *Biometrika*, pages 97–109, 1970.

[160] A. Gelman and D.B. Rubin. Inference from iterative simulation using multiple sequences. *Statistical Science*, 7:457–511, 1992.

[161] Lm An, Stephen Brooks, and Andrew Gelman. Stephen brooks and andrew gelman. *Journal of Computational and Graphical Statistics*, 7:434–455, 1998.

[162] C.L. Reichardt, L. Shaw, O. Zahn, K.A. Aird, B.A. Benson, et al. A measurement of secondary cosmic microwave background anisotropies with two years of South Pole Telescope observations. 2011, 1111.0932.

[163] E. Shirokoff, C.L. Reichardt, L. Shaw, M. Millea, P.A.R. Ade, et al. Improved constraints on cosmic microwave background secondary anisotropies from the complete 2008 South Pole Telescope data. *Astrophys.J.*, 736:61, 2011, 1012.4788.

[164] M. Lueker, C.L. Reichardt, K.K. Schaffer, O. Zahn, P.A.R. Ade, et al. Measurements of Secondary Cosmic Microwave Background Anisotropies with the South Pole Telescope. *Astrophys.J.*, 719:1045–1066, 2010, 0912.4317.

[165] Hy Trac, Paul Bode, and Jeremiah P. Ostriker. Templates for the Sunyaev-Zel'dovich Angular Power Spectrum. *Astrophys.J.*, 727:94, 2011, 1006.2828.

[166] Renee Hlozek, Joanna Dunkley, Graeme Addison, John William Appel, J.Richard Bond, et al. The Atacama Cosmology Telescope: a measurement of the primordial power spectrum. 2011, 1105.4887.

[167] R. E. Smith et al. Stable clustering, the halo model and nonlinear cosmological power spectra. *Mon. Not. Roy. Astron. Soc.*, 341:1311, 2003, astro-ph/0207664.

[168] Marcos Lima and Wayne Hu. Self-Calibration of Cluster Dark Energy Studies: Counts in Cells. *Phys. Rev.*, D70:043504, 2004, astro-ph/0401559.

[169] Marcos Lima and Wayne Hu. Self-Calibration of Cluster Dark Energy Studies: Observable-Mass Distribution. *Phys. Rev.*, D72:043006, 2005, astro-ph/0503363.

[170] Subhabrata Majumdar and Joseph J. Mohr. Self calibration in cluster studies of dark energy: Combining the cluster redshift distribution, the power spectrum and mass measurements. *Astrophys.J.*, 613:41–50, 2004, astro-ph/0305341.

[171] B.A. Benson, T. de Haan, J.P. Dudley, C.L. Reichardt, K.A. Aird, et al. Cosmological Constraints from Sunyaev-Zel'dovich-Selected Clusters with X-ray Observations in the First 178 Square Degrees of the South Pole Telescope Survey. 2011, 1112.5435.

[172] K. Andersson, B.A. Benson, P.A.R. Ade, K.A. Aird, B. Armstrong, et al. X-ray Properties of the First SZE-selected Galaxy Cluster Sample from the South Pole Telescope. *Astrophys.J.*, 738:48, 2011, 1006.3068.

[173] F.W. High, H. Hoekstra, N. Leethochawalit, T. de Haan, L. Abramson, et al. Weak-Lensing Mass Measurements of Five Galaxy Clusters in the South Pole Telescope Survey Using Magellan/Megacam. 2012, 1205.3103.

[174] N. Jarosik, C.L. Bennett, J. Dunkley, B. Gold, M.R. Greason, et al. Seven-Year Wilkinson Microwave Anisotropy Probe (WMAP) Observations: Sky Maps, Systematic Errors, and Basic Results. *Astrophys.J.Suppl.*, 192:14, 2011, 1001.4744.

[175] J. Dunkley et al. Five-Year Wilkinson Microwave Anisotropy Probe (WMAP) Observations: Likelihoods and Parameters from the WMAP data. *Astrophys.J.Suppl.*, 180:306–329, 2009, 0803.0586.

[176] L. Page et al. Three year Wilkinson Microwave Anisotropy Probe (WMAP) observations: polarization analysis. *Astrophys.J.Suppl.*, 170:335, 2007, astro-ph/0603450.

[177] Neelima Sehgal, Hy Trac, Viviana Acquaviva, Peter A.R. Ade, Paula Aguirre, et al. The Atacama Cosmology Telescope: Cosmology from Galaxy Clusters Detected via the Sunyaev-Zel'dovich Effect. *Astrophys.J.*, 732:44, 2011, 1010.1025.

[178] Adam G. Riess, Lucas Macri, Stefano Casertano, Hubert Lampeitl, Henry C. Ferguson, et al. A 3% Solution: Determination of the Hubble Constant with the Hubble Space Telescope and Wide Field Camera 3. *Astrophys.J.*, 730:119, 2011, 1103.2976.

[179] Adam G. Riess et al. A Redetermination of the Hubble Constant with the Hubble Space Telescope from a Differential Distance Ladder. *Astrophys. J.*, 699:539–563, 2009, 0905.0695.

[180] G. Fritz Benedict, Barbara E. McArthur, Michael W. Feast, Thomas G. Barnes, Thomas E. Harrison, et al. Hubble Space Telescope Fine Guidance Sensor Parallaxes of Galactic Cepheid Variable Stars: Period-Luminosity Relations. *Astron.J.*, 133:1810–1827, 2007, astro-ph/0612465.

[181] H. V. Peiris et al. First year Wilkinson Microwave Anisotropy Probe (WMAP) observations: Implications for inflation. *Astrophys. J. Suppl.*, 148:213, 2003, astro-ph/0302225.

[182] E. Komatsu et al. First year Wilkinson Microwave Anisotropy Probe (WMAP) observations: tests of gaussianity. *Astrophys.J.Suppl.*, 148:119–134, 2003,

astro-ph/0302223.

[183] Laura Cayon, Christopher Gordon, and Joseph Silk. Probability of the most massive cluster under non-Gaussian initial conditions. 2010, 1006.1950.

[184] B. Sartoris, S. Borgani, P. Rosati, and J. Weller. Probing dark energy with the next generation X-ray surveys of galaxy clusters. 2011, 1112.0327.

[185] Annalisa Pillepich, Cristiano Porciani, and Thomas H. Reiprich. The X-ray cluster survey with eROSITA: forecasts for cosmology, cluster physics, and primordial non-Gaussianity. 2011, 1111.6587.

[186] M. Pierre, F. Pacaud, J.B. Juin, J.B. Melin, N. Clerc, et al. Precision cosmology with a wide area XMM cluster survey. *Mon.Not.Roy.Astron.Soc.*, 414:1732, 2011, 1009.3182.

[187] S. J. E. Radford, R. Giovanelli, T. A. Sebring, and J. Zmuidzinas. CCAT. In D. C. Lis, J. E. Vaillancourt, P. F. Goldsmith, T. A. Bell, N. Z. Scoville, and J. Zmuidzinas, editors, *Submillimeter Astrophysics and Technology: a Symposium Honoring Thomas G. Phillips*, volume 417 of *Astronomical Society of the Pacific Conference Series*, page 113, December 2009.

[188] T. Abbott et al. The dark energy survey. 2005, astro-ph/0510346. White Paper submitted to Dark Energy Task Force.

[189] R. Fassbender, H. Boehringer, A. Nastasi, R. Suhada, M. Muehlegger, et al. The X-ray luminous galaxy cluster population at $0.9 < z <\sim 1.6$ as revealed by the XMM-Newton Distant Cluster Project. *New J.Phys.*, 13:125014, 2011, 1111.0009.

[190] A. Reichert, H. Bohringer, R. Fassbender, and M. Muhlegger. Observational constraints on the redshift evolution of X-ray scaling relations of galaxy clusters out to $z \sim 1.5$. 2011, 1109.3708.

[191] P.A.R. Ade et al. Planck Early Results XI: Calibration of the local galaxy cluster Sunyaev-Zeldovich scaling relations. *Astron.Astrophys.*, 536:A11, 2011, 1101.2026.